An Experimental Study of Turbulent Vortex Rings Using Particle Image Velocimetry

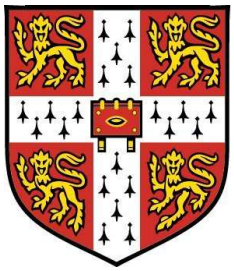

Lian Gan

Department of Engineering

University of Cambridge

A thesis submitted for the degree of

Doctor of Philosophy

August 2010

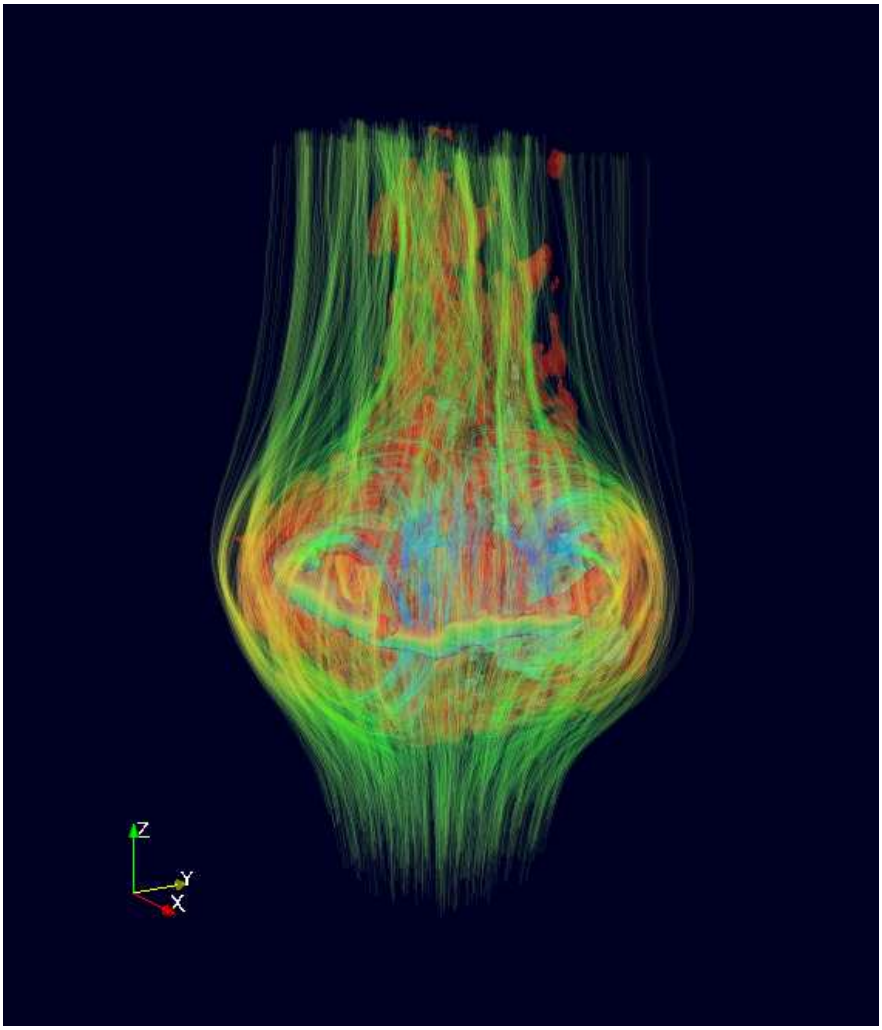

Measure what is measurable, and make measurable what is not so.

- Galileo Galilei c. 1610

Declaration

I hereby declare that:

this dissertation is the result of my own work and includes nothing which is the outcome of work done in collaboration except where specifically indicated in the text;

this dissertation is not substantially the same as any that I have submitted, or, is being concurrently submitted for a degree or diploma or other qualification at the University of Cambridge or any other university or similar institution except as declared in the preface and specified in the text. I further state that no substantial part of my dissertation has already been submitted, or is being concurrently submitted for any such degree, diploma or other qualification at the University of Cambridge or any other university of similar institution except as declared in the preface and specified in the text;

this dissertation does not exceed the word limit for the respective Degree Committee.

Signature:

Date:

I would like to dedicate this thesis to my loving parents
Mr. Zhaohe Gan and Ms. Hua Zheng
and my wife
Ms. Huajing Zhao

Acknowledgements

I would like to express my sincere gratitude to all those people who contribute to the completion of this thesis by encouraging me to start, sustain and finish it. For this reason and many others, I would like to firstly show my appreciation to my supervisor Dr. T. B. Nickels, who has played a pivotal role in my intellectual journey of the Ph.D. He has always been resourceful and has dedicated much of his time and energy in guiding me to complete this research and to write up the thesis. In addition, I also wish to thank both my internal examiner Dr. J. Dawson and external examiner Dr. G. N. Coleman for their critical comments and suggestions of the thesis.

I particularly owe my great gratitude for my beloved parents who always stand with me, sharing happiness and sadness with me throughout the years. Without their support, my undertaking of this research could not have been successfully achieved. My deepest love also goes to my wife for her intellectual and emotional support. It is with her long accompanying that made my Cambridge life more colourful and enjoyable. Special gratitude also goes to my father and mother-in-law for their advices and encouragement.

I would also like to express my appreciation to my seniors, friends and colleagues, for the sharing of their ideas and valuable discussions and suggestions, especially to Dr. P. Ray and Dr. X. Wei.

This study could not have been completed without the help from the technicians in the Heat Lab, Department of Engineering for manufacturing the components of the experimental rigs. Thank is specially addressed to Mr. M. Underwood and Mr. R. Leroy.

Last but not least, I would like to thank all my dear old friends outside of the university. They have ungrudgingly shown their spiritual supports and encouragements throughout my Ph.D. studies.

Abstract

In this dissertation, the early development of turbulent vortex rings at two Reynolds numbers is studied using two-dimensional and Stereoscopic Particle Image Velocimetry. In the late 1980s' a similarity theory of turbulent vortex rings was proposed and tested primarily using a two-channel tracking Laser Doppler Velocimeter. However, due to the limitations of the experimental technique the tests were inconclusive and important assumptions could not be checked. Since single-point measurements were used, turbulent vortex ring structures could only be inferred using a complex signal-analysis technique. In the present study, two-dimensional and stereoscopic Particle Image Velocimetry techniques provide spatial and temporal resolved measurements of the full field of the cross-section of turbulent vortex rings, from which a more rigorous investigation of the similarity theory is possible. Since the region over which the similarity theory appears to hold starts at about 2.5 orifice diameters downstream, this study focusses on the early development region from this point to ten diameters downstream. Finally, the ensemble-averaged turbulent ring velocity contours, vorticity contours, pressure field contours, as well as Reynolds stresses and turbulence production contours, are presented. The effects of the turbulent vortex ring position dispersion and tilting angle variation on the measurement results are also studied and quantified. An effort is also made to reconstruct a three-dimensional turbulent vortex ring velocity field by adopting Taylor's hypothesis. Some important features are successfully captured. An azimuthal-averaging method is also developed in an attempt to estimate the turbulence quantities in cylindrical coordinates. However, because of various limitations, the three-dimensional reconstruction method is not perfect, and room for future improvement is discussed.

Contents

List of Figures

List of Tables

Chapter 1

Introduction

Vortex rings, three-dimensional toroidal structures resulting from boundary layer roll-up, have been observed in various shapes and sizes. Perhaps the most familiar example of a vortex ring is the smoke ring produced when cigarette smoke is suddenly ejected through the lips of a smoker, or when there is a sudden ejection of gas from an exhaust nozzle of a vehicle. A typical structure of a vortex ring is shown in figure 1.1, where layers of dyed fluid are noticeable. In nature, vortex rings can be observed in various length scales, from a few kilometres to a few millimetres.

Examples of large-scale vortex rings are the 'mushroom cloud' formed during a nuclear explosion or mushroom-shaped plume formed during a volcanic eruption. The physics of the mushroom cloud formation after detonation of a nuclear bomb involves hot gases rotating and rising into a toroidal shape inside the head of the cloud, while cooler air is drawn into the cloud and upwards to form the 'vortex-ring bubble'. Fascinatingly, very similar phenomenon can be observed in laboratories, e.g. when a water droplet impacts a water surface from a distance above (see figure 1.2). The physics of a volcanic eruption is very similar to the formation of cigarette smoke rings, the pyroclastic material exits from the volcano mouth and roll up into a mushroom shape.

A microburst (downburst) is another large-scale example in nature, which is opposite to a tornado and is a potential hazard for aircraft. A ring forms when the wind curls as the cold air of the downburst moves away from the point of impact with the ground. A similar picture of downburst can be seen at the start of the launching of a rocket or spacecraft.

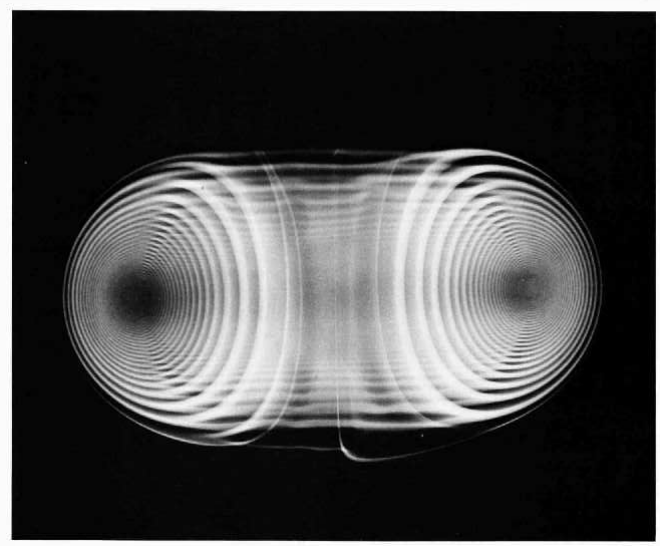

Figure 1.1: Ejection of smoke from the end of a tube into air. Reynolds number is approximately 10000. Image taken from van Dyke (1982).

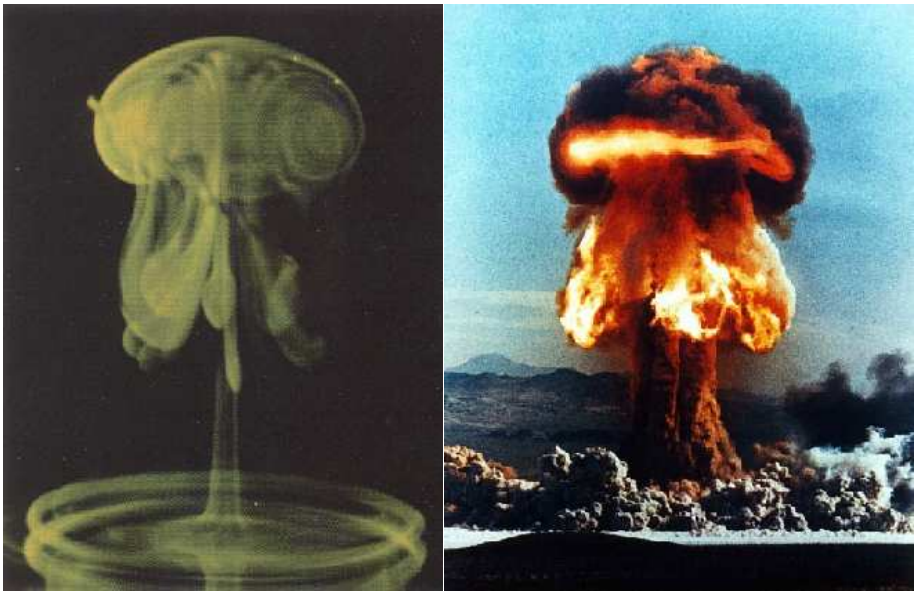

Figure 1.2: Comparison of the vortex structure created by a $2.6mm$ water drop $50ms$ after impacting a pool of water after a fall of $35mm$ (left, inverted) and an above-ground nuclear test, Nevada, 1957, U.S. Department of Energy (right). Left image taken from Peck & Sigurdson (1994).

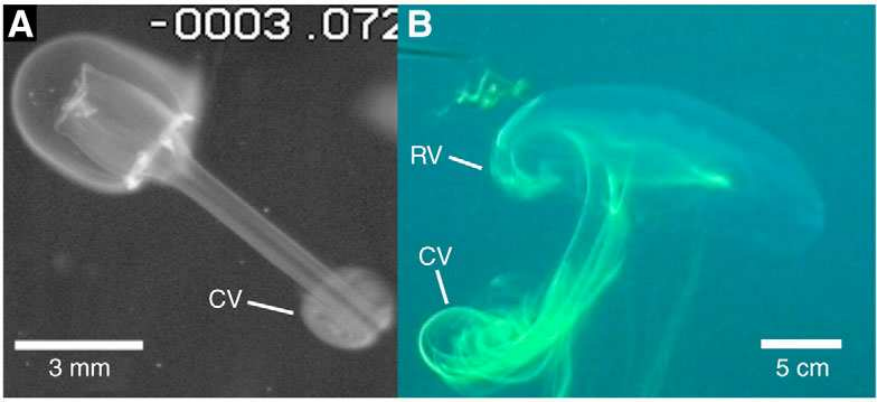

Figure 1.3: Visualisations of medusa flow currents. (A) Jet propulsion in juvenile *Aequorea victoria*. A vortex ring (CV) is formed in the water during the bell contraction phase, whereas no vortex is formed in the water during the bell relaxation phase. (B) Jet-paddling in *Aurelia aurita*. Vortex rings of opposing rotational orientation are formed in the water during bell contraction (CV) and relaxation (RV), respectively. The stopping vortex can be observed forming near the bell margin (RV). Image taken from Dabiri *et al.* (2007).

Smaller-scale vortex rings can be observed when some aquatic species shed vortices from their bodies or produce vortex rings as a means of propulsion for swimming; see figure 1.3. The shed vortices can advance downstream by their self-induced velocity and form a vortex ring. Such biological propulsion mechanisms have attracted substantial research, in order to discover an optimal way of swimming. Vortex rings are also seen in human physiological flows, as when the blood flow enters the cardiac left ventricle during diastole, a vortex ring can form (see figure 1.4). The physics is also similar to the nozzle vortex ring discussed above, but it is a periodic process. Researchers have attempted to link some of the properties of such periodic formations of rings to the evidence of certain cardiac diseases, which remain leading causes of death worldwide.

Because of its relatively robust capability for momentum delivery, the physics of vortex rings is widely applied to engineering problems. For instance, there has been evidence of applying vortex rings for underwater drilling; vortex rings are also potentially useful for fighting oil-well fires. They are also applied for military purposes, in developing weapons like vortex cannons or vortex guns. Such weapons have shown that they are capable of knocking down a $75kg$ human dummy from 10

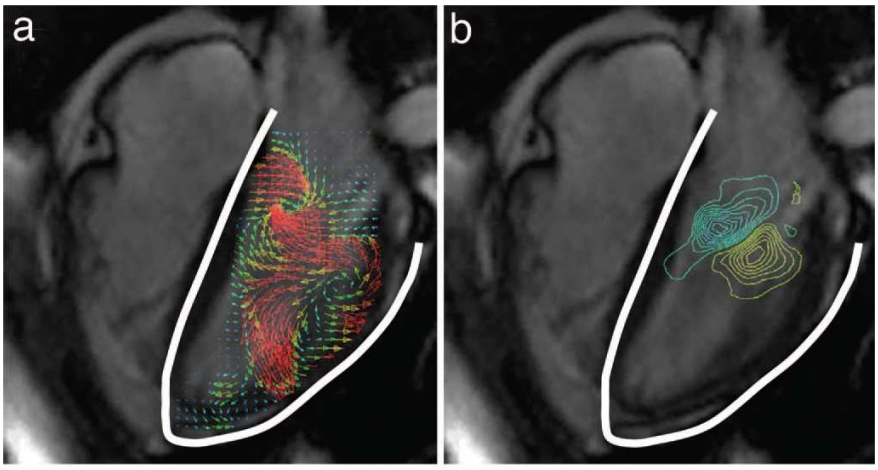

Figure 1.4: Vortex ring formation *in vivo* and *in vitro*. (a and b) Map of *in vivo* blood flow velocity vectors and vorticity (rotation and shear) contours in the left ventricle (LV) of a human heart during diastole. Images were obtained by magnetic resonance imaging (MRI) of a healthy adult. The LV boundary is indicated by a white line. Vortical patterns are indicated by the orientation of velocity vectors and by vorticity contours. Blue and yellow contours indicate clockwise and counter-clockwise fluid rotation, respectively. Image taken from Gharib *et al.* (2006).

meters away. Large vortex cannons are even able to knock down thin walls. Other examples involve vortex rings' excellent translation ability due to their self-induced velocity. Applications have been found in using acoustic guns to measure distances.

The role of vortex rings in mixing has also been recognized in a variety of applications because of their entrainment capability. They are found to be responsible in shear layer mixing, and they are also used to help mix chemicals in combustion chambers to increase the efficiency of combustion and other chemical reactions.

Most of the phenomena and applications are related to turbulent vortex rings, or highly excited vortex rings. The physics of vortex rings thus certainly deserves an intensive study in order to understand phenomena in nature.

Chapter 2

Literature Review

The study of laminar vortex rings, as an interesting topic in fluid mechanics, has attracted at least 50 years of research. Some physics associated with laminar vortex rings have been summarised in Shariff & Leonard (1992) and Lim & Nickels (1995). There is not so much literature on turbulent vortex rings, however. In this chapter, some relevant information about turbulent vortex rings is presented and revised and the significance of this research activity is also given.

2.1 Slug model

A vortex ring in laboratory studies is usually generated by an impulsive ejection of fluid through a nozzle or an orifice into a quiescent environment. The inner boundary layer of the nozzle or the orifice is ejected and rolls up to form a toroidal structure, which is known as a vortex ring. An example of a nozzle-generated vortex ring is shown in figure 1.1. Two mathematical models were invented in order to quantify the formation process. The first model, which is perhaps the most commonly used, is the slug model. The slug model has been widely adopted by researchers to predict the circulation of vortex rings. A piston movement through a nozzle is the easiest example to illustrate the concept of the model; see figure 2.1. The velocity $U_p(t)$ and the stroke length L of the piston motion determine the circulation of the ring and may be used to define a Reynolds number which partly characterises the nature of the ring.

In this model, the velocity profile external to the boundary layer across the nozzle exit plane is assumed to be axisymmetric and top-hat shaped, which is represented

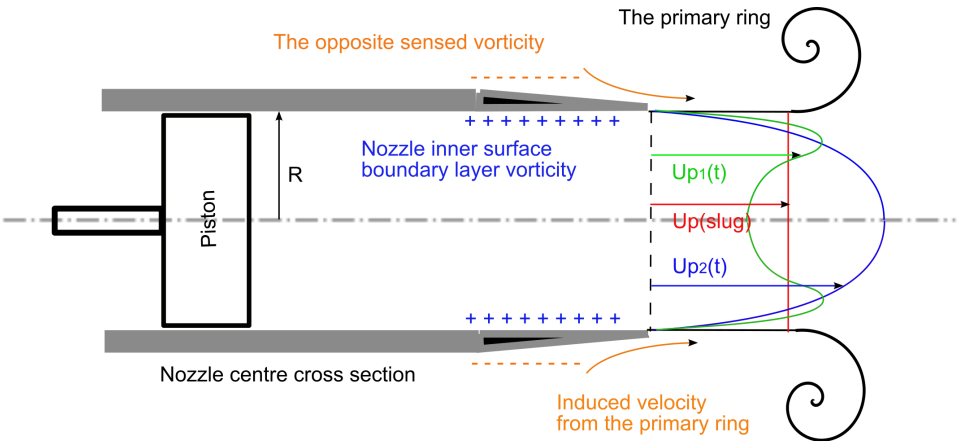

Figure 2.1: Illustration of influences of various factors on the slug model. U_p denotes the slug model velocity profile at the tube exit; $U_{p1}(t)$ denotes the profile at the beginning of the piston motion; $U_{p2}(t)$ denotes the profile at a later time. $U_{p1}(t)$ and $U_{p2}(t)$ can be functions of time. Thus the piston stroke length $L = \int_0^T U_p(t)\mathrm{d}t$, where T is the slug time.

by $U_p(slug)$ in figure 2.1. The peak velocity is assumed to be equal to the piston velocity. (Due to the existence of a thin boundary layer and continuity, the peak velocity at larger time is always higher than the piston velocity; see $U_{p2}(t)$ in figure 2.1, which will be discussed further below.) In cylindrical coordinates, the rate of the circulation Γ_{slug} created and ejected by the piston, which is also called the vorticity flux, can be written as:

$$\begin{aligned} \frac{\mathrm{d}\,\Gamma_{slug}}{\mathrm{d}\,t} &= \int_0^R \omega_\theta u_y \,\mathrm{d}r \\ &\approx \int_0^R -\frac{\partial u_y}{\partial r} u_y \,\mathrm{d}r \\ &\approx \frac{1}{2} U_p^2(t), \end{aligned} \tag{2.1}$$

where R denotes the nozzle radius (see figure 2.1); $U_p(t)$ denotes the piston velocity history; r, θ and y denote the radial, azimuthal and axial direction of the cylindrical coordinates, while ω_θ is the azimuthal vorticity. The first approximation in 2.1 involves the assumption that in axisymmetric situations, the azimuthal vorticity

$$\omega_\theta = \frac{\partial u_r}{\partial y} - \frac{\partial u_y}{\partial r} \approx -\frac{\partial u_y}{\partial r}, \tag{2.2}$$

since the boundary-layer equation assumes $\partial u_r/\partial y$ is negligible compared with $\partial u_y/\partial r$. The second approximation in equation 2.1 involves the assumption that the peak velocity (on the axis of symmetry) is equal to the piston velocity. Thus if the piston velocity programme is an impulsive start to a constant (i.e. $U_p(t) = U_p$, for $t > 0$), the total slug circulation produced can be written as

$$\begin{aligned} \Gamma_{slug} &= \int_0^T \frac{1}{2} U_p^2 \, \mathrm{d}t \\ &= \frac{1}{2} U_p \int_0^T U_p \, \mathrm{d}t \\ &= \frac{1}{2} U_p L, \end{aligned} \tag{2.3}$$

where T is the slug time and L is the piston stroke length. The Reynolds number hence can be defined by the slug circulation

$$Re_{slug} = \frac{\Gamma_{slug}}{\nu} = \frac{U_p L}{2\nu}.^{1} \tag{2.4}$$

If the momentum of the piston motion is assumed to be entirely delivered to the discharged fluid, the speed of the discharged volume equals the piston speed, and the idealised slug impulse I_{slug} can be written as

$$\begin{aligned} I_{slug} &= \rho \times vol_{dis} \times U_{dis} \\ &= \left(\frac{1}{4} \pi D^2 L \rho \right) U_p, \end{aligned} \tag{2.5}$$

where D is the nozzle diameter. Note that this is not the true impulse because it takes no account of the over pressure at the nozzle exit. This point will be discussed in section 5.1.9.

Didden (1979) made some measurements of the velocity fields in the vicinity of the nozzle exit using Laser Doppler Velocimeter (LDV) and found that, the actual circulation produced by the piston motion can be written as

$$\frac{\Gamma}{\Gamma_{slug}} = 1.14 + 0.32 \left(\frac{L}{D} \right)^{-1}, \tag{2.6}$$

[1] In this dissertation, unless otherwise indicated, Re is equivalent to Re_{slug}

by data fitting. This equation is most accurate for $Re < 7000$ and $L/D > 0.6$. Therefore, at these conditions, the slug circulation underestimates the real circulation, and the degree of the underestimation depends on the L/D value. The work in Maxworthy (1977), however, found that for higher Re, in the range between 30000 to 50000, the slug circulation overestimates the real circulation. The comparison of the slug circulation and the circulation calculated from various experiments is shown in figure 2.2. The discrepancies between the real and slug circulations are attributed to three major causes given in Didden (1979) experimentally and in Nitsche & Krasny (1994) numerically.

- First, for small times the velocity near the nozzle exit exceeds the instantaneous piston velocity due to piston acceleration, the effect of which is to increase the velocity gradients and hence to increase the vorticity flux.
- Second, at larger times, because the boundary layer becomes thicker, the center flow velocity will also be appreciably larger than the piston velocity U_p.
- Third, the flux of the opposite-sensed vorticity from the nozzle external wall is entrained into the main ring due to the pressure fields.

The first two factors increase the real value and the third one decreases it. A schematic illustration of these three factors is shown in figure 2.1.

Later researchers have found other possible influences on the real ring's circulation. Allen & Chong (2000) used dye visualisation and particle tracking to provide a scaling law and quantified the growth rate of a piston vortex ring, which is generated from the separated boundary layer material when the piston advances (Hughes & Gerrard, 1971). The mature piston vortex may eventually detach from the piston surface and interact with the primary vortex ring under certain conditions, e.g. when the piston surface stops flush with the nozzle/orifice exit plane. Cater *et al.* (2004) used Particle Image Velocimetry (PIV) to investigate the effect quantitatively and showed that the imperfect merging of the piston vortex and the primary ring can not only increase the circulation of the primary ring but also promote the transition of the ring to turbulent. Nevertheless, the effect of the piston vortex can be eliminated under other circumstances, for instance, when the piston stops several nozzle/orifice diameters behind the exit.

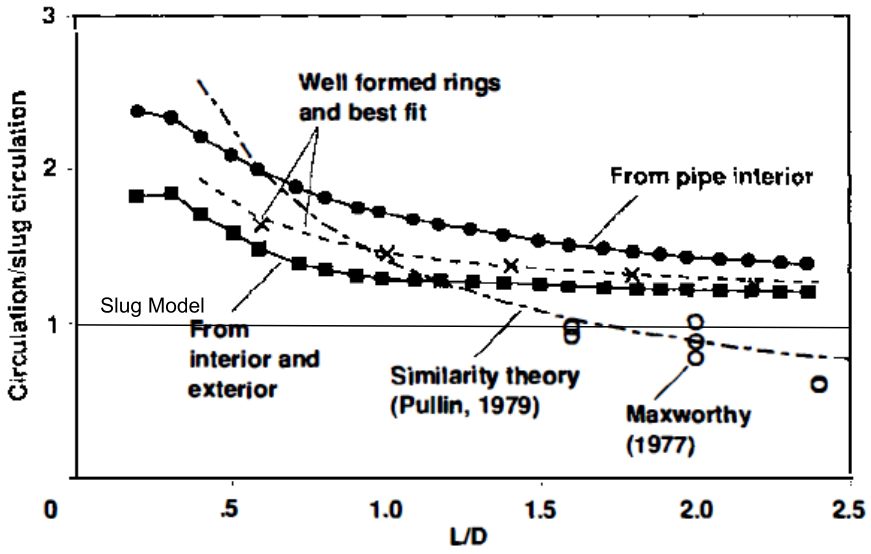

Figure 2.2: Circulation of vortex rings formed at a pipe exit referred to the circulation predicted by the slug model. Unless indicated, the data are from Didden (1979). The multiple data points of Maxworthy (1977) at the three L/D values are for different Reynolds numbers, increasing downward. Figure taken from Shariff & Leonard (1992).

Unlike most flow phenomena, Reynolds number is not the only important parameter for predicting the level of turbulence. In the vortex ring formation process, two other factors also play critical roles, namely dimensionless number L/D and the history of the piston velocity as a function of time (piston velocity programme). The history of the piston movement is usually set to be a constant in most of the experiments. Examples of other piston movement types can be found in Glezer (1988). Glezer (1988) also did flow visualisation experiments on vortex rings at various Reynolds numbers and L/D ratios, and combined the results from earlier researchers, to quantify the conditions (the mapping of Re and L/D) which can produce turbulent vortex rings immediately upon initiation. Glezer (1988) divided the turbulent vortex rings into two main types: turbulence from laminar instability and turbulence upon initiation, on a transition map; see figure 2.3. The mechanism that generates turbulence in the second type of the rings is attributed to the Kelvin-Helmholtz instability on the cylindrical slug of fluid behind the main spiral. Another possible explanation is the Rayleigh centrifugal instability caused by the ingestion of secondary vorticity into the main vorticity roll-up sheet (Maxworthy, 1972).

The second model for describing the vortex ring formation process is the self-similar roll-up, which is based on the analysis of the roll-up of an inviscid, two-dimensional vortex sheet. This is so far the only model that attempts to account for vortex sheet evolution during the formation and gives some insight into the vortex core structure. This model was applied to the ring formation at a tube exit by Saffman (1978) for the case of an impulsive-started flow and later was extended by Pullin (1979) to ring formation at orifice exits and for more general piston speed programmes. Because this study does not aim to investigate the ring formation process or the core structure, this model is not discussed in detail.

2.2 Models for turbulent vortex rings

Detailed quantitative data at various downstream locations from the nozzle exit for various stages of ring development have been given by many researchers, but mostly for laminar or relatively low Reynolds number cases; some examples can be found in section 2.3 for both experimental and numerical studies. When the Reynolds

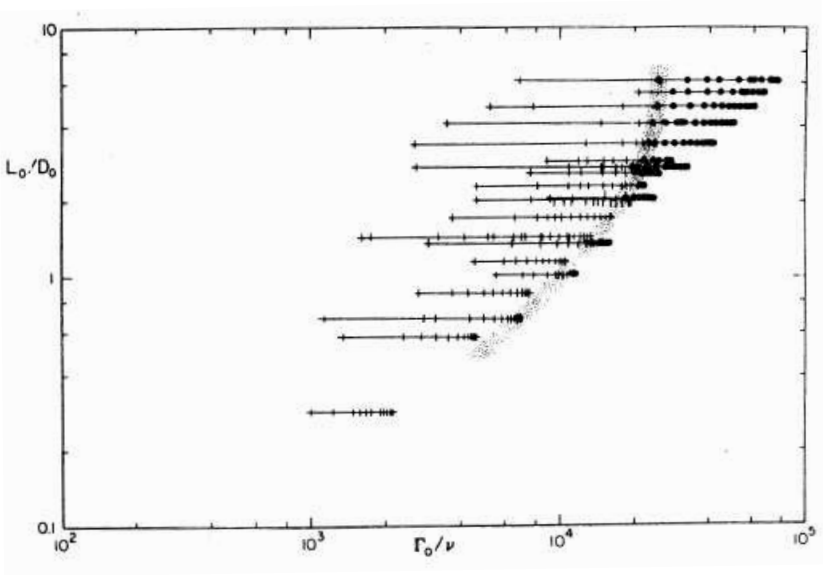

Figure 2.3: The transition map marked rings at various Re and L/D ratios. • denotes turbulent rings and + denotes laminar rings. Γ_o is the slug circulation Γ_{slug}. Figure taken from Glezer (1988).

number is sufficiently high, or the stroke length is sufficiently long, the vortex ring produced may be turbulent; see section 2.1 and figure 2.3. There have been relatively few studies of turbulent vortex rings, among which are Maxworthy (1974), Johnson (1970), Johnson (1971), Sallet & Widmayer (1974). The most comprehensive study of turbulent vortex ring structure, however, is given in Glezer & Coles (1990), in which a long-term similarity solution was proposed based on the assumption of the invariance of the impulse, and experiments were made to examine the ring structure and turbulence statistics. Maxworthy (1974) and Johnson (1970) also independently developed models accounting for turbulent vortex rings' long-term properties, but their models are empirical or semi-empirical ones. These three models are briefly discussed here.

2.2.1 The similarity theory

The similarity theory proposed by Glezer & Coles (1990) is based on dimensional analysis and the invariance of the impulse. It is reviewed here in more detail because it is the only non-empirical model among the three and serves as the the-

oretical background of the present research activity. Two-channel LDV was used to acquire two components of velocity at various streamwise and spanwise stations. This, however only provided instantaneous velocity information at a single point in the flow field at one probe station, although the two channels give two velocity components. This limitation is important because, first, spatial structure must be inferred from temporal information and second, the information is almost 'blind' to the surrounding environment (the relative position in the ring structure where the velocity information is obtained). To overcome the first limitation, Taylor's hypothesis (Taylor, 1938) and their similarity theory were applied; to overcome the second, considerable statistical treatments were unavoidable. They first developed a signature recognition scheme to filter out the 'imperfect' or 'suspicious' data points and applied time-axis shifting before applying conventional statistical methods to obtain ensemble-averaged structures. It must also be noted that because of the limitation of LDV, data in the adjacent probe stations are uncorrelated. Their experiments did seem to show that their turbulent vortex rings follow similarity developments from as early as 2.5 orifice diameters downstream from the exit. Notwithstanding the noticeable success of the theory in predicting the mean quantities (e.g. velocities, circulation, impulse, entrainment) and the turbulence quantities (e.g. stresses and production), their study, while careful and comprehensive, suffered from a number of limitations (that were recognised and noted by the authors) which include

- Spatial structure is inferred using Taylor's hypothesis from single-point measurements, together with the application of similarity theory, i.e. data from all the streamwise and spanwise probe stations are scaled into a single position in similarity space, by temporal information.
- Only two components of the velocity were measured.
- Ring dispersion[1] was significant and difficult to visualise and correct for when relying on point measurements, i.e. dispersion can only judged from instantaneous velocity components with respect to the ensemble-averaged value.

[1]The term dispersion is not clearly defined in Glezer & Coles (1990). It is a general term to indicate the location difference of the ring cores from one instantaneous realisation to another. In this dissertation, this term refers to the distance from the instantaneous ring core locations to that of the ensemble-averaged ring.

- The invariance of the impulse was assumed but could not be checked.

Therefore some results may not be true to nature and some detailed physics could be hidden and masked. The limitations mentioned above thus leave the present study room to verify and correct their results and reveal more mechanics of turbulent vortex rings than that presented in Glezer & Coles (1990).

The mathematical background of the similarity theory will be discussed in detail in chapter 4.

2.2.2 Maxworthy's model

Maxworthy (1974) performed flow visualisation experiments to measure the vortex rings' bubble radius and propagation velocity, and proposed a semi-empirical model which does not rely on impulse invariance, because impulse was observed to be continuously lost in the wake. The loss of impulse was modelled by an equivalent drag. This model of drag together with a model related to ring-bubble entrainment and a hypothesis of partial self-similarity were assumed to explain and predict the observed decay of ring propagation velocity and growth of the bubble volume. The result showed that the radius (hence the bubble volume) and the propagation speed of a vortex ring grow and decay as power laws of time (with a dimensionless time properly defined). The results reduce to the similarity scaling law in an extreme condition. More details can be found in Maxworthy (1974), or in the review articles Shariff & Leonard (1992) and Lim & Nickels (1995). The model is also briefly summarised in appendix A.

2.2.3 Johnson's model

The experimental study by stroboscopic photography and hot-wire anemometry in Johnson (1970) found that turbulent rings did not reach a similarity stage until about 1000 diameters away from the ring generator. This model was based on fully-empirical data fitting, and no strong physical reasoning was given. This model also gave a power-law function of ring's propagation distance (and hence velocity) and radius; see Lim & Nickels (1995) or appendix B.

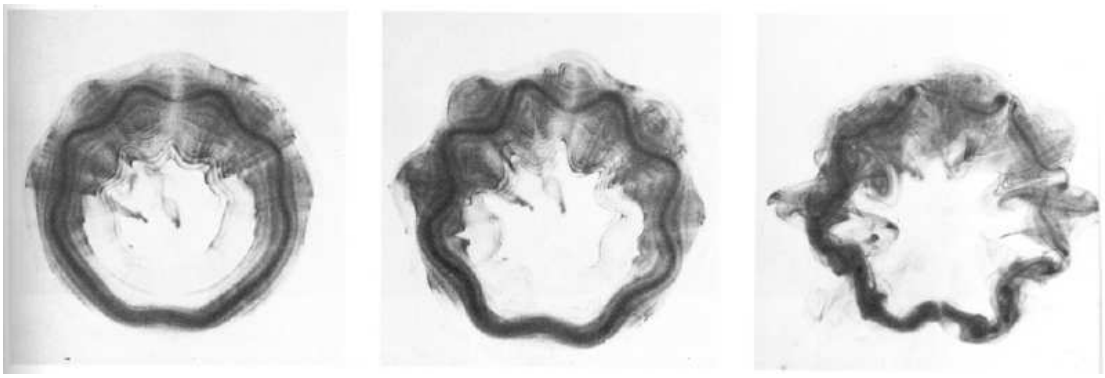

Figure 2.4: Sequential photographs of a $Re = 2000$ ring in its azimuthal plane. Dye visualisation. Figure taken from van Dyke (1982).

2.3 Azimuthal instability

Vortex rings which are well formed at the nozzle/orifice exit, under certain conditions, can undergo an instability along the core circumference in the form of waves; see figure 2.4. This type of azimuthal instability is an important mechanism in the transition of a laminar vortex ring to turbulence. Although this type of waviness is most investigated on laminar or transitional rings, it will be shown in chapter 7 that azimuthal waves are also observed in a fully turbulent ring. In this section, some of the analyses of the azimuthal waves in a vortex ring are reviewed.

The first experimental work showing the existence of azimuthal waves was Krutzsch (1939), but the physics of the waves were not studied in detail until the 1970s', by a number of experimental and analytical studies, for example Widnall & Sullivan (1973), Widnall *et al.* (1974), Maxworthy (1977), Widnall & Tsai (1977), Saffman (1978), Weigand & Gharib (1994), Dazin *et al.* (2006a), Dazin *et al.* (2006b) and later numerical studies like Shariff *et al.* (1994) Bergdorf *et al.* (2007).

Maxworthy (1972) found that the instability develops for Reynolds numbers based on piston diameter larger than 600. Widnall & Sullivan (1973) suggested that, in the absence of viscosity, a vortex ring with a thin core is almost always unstable to a small wave-like perturbation, and also showed that the number of waves increased with decreasing core size. Their model successfully predicted the amplification rate and the shape of the instability waves but was not able to predict

the number of waves. Widnall *et al.* (1974) developed a model of the waves observed on a straight filament in Moore & Saffman (1975a), and gave an explanation of the instability mechanism on a vortex core by considering the effect of the straining field. They were the first to suggest theoretically that the direction of the growth of the instability wave should be at 45° with respect to the direction of propagation of the vortex and the result was confirmed later by Maxworthy (1977) and Shariff *et al.* (1994). Widnall & Tsai (1977) further refined these ideas and gave a rigorous theory based on expansion of the steady-flow solution for the ring field and of the unsteady wave perturbations in an asymptotic series in the core-radius to ring-radius ratio. Their model predicted the wave number and the growth rate for thin-core vortex rings with constant vorticity or with a continuous distribution of vorticity in an ideal fluid. Saffman (1978) used a vortex sheet roll-up model to predict the vorticity distribution of the core and successfully described the variation of the wavelength of the instability with Reynolds number for vortex rings produced with a tube. The models of Widnall & Tsai (1977) and Saffman (1978) were later confirmed by PIV results in Dazin *et al.* (2006a) and Dazin *et al.* (2006b). The observation of secondary structure outside of the main waves in Dazin *et al.* (2006b) was further supported by the numerical results in Bergdorf *et al.* (2007).

A mean flow inside the vortex ring core usually accompanies the appearance of the waves, when the amplitude of the waves on the vortex ring becomes significant. This flow was referred to as an axial flow by Moore & Saffman (1975b) (in a straight vortex filament) and by Maxworthy (1977) (in a vortex ring core). The axial flow was also observed in a numerical study in Shariff *et al.* (1994) by solving the incompressible Navier-Stokes equation, in Archer *et al.* (2008) by Direct Numerical Simulation (DNS) and in an experimental study in Naitoh *et al.* (2002) using the smoke-wire technique. Maxworthy (1977) observed that the axial flow appears after the wave breaking and takes the form of a propagating wave, while Naitoh *et al.* (2002) noticed two types of axial flow and both of which start to increase before the start of the azimuthal wave breaking and the velocities of the axial flow increase gradually. They also found that the axial flow was conical shaped, which was inferred by an opposite sensed axial flow in the core centre (inside of the cone) and the surrounding circumferences (outside of the cone). The magnitude of the veloc-

ity was found to be about 25% of the ring propagation velocity. Their results were supported by Archer *et al.* (2008).

2.4 Vortex ring formation time

An interesting phenomenon associated with the formation of vortex rings at long stroke lengths was not discovered until the work of Gharib *et al.* (1998), who examined the vortex-formation process for longer stroke lengths, $L/D > 4$, and observed a robust limit on the maximum growth of rings formed using a piston-cylinder apparatus. The dimensionless ratio L/D, the formation number, is also known as the formation time because L is related to time by $L = U_p t$ for a constant piston velocity.

Gharib *et al.* (1998) investigated the nozzle-generated vortex ring formation experimentally by PIV, and found that the primary vortex ring accepts the vorticity flux from the vortex generator until the formation time $L/D \approx 4$. Beyond this time, the primary ring pinches off such that the extra vorticity ejected from the generator is rejected by the primary ring and forms a series of trailing rings in the wake due to the Kelvin-Helmholtz-like instability; see figure 2.5.[1] Quantitatively speaking, the pinch-off happens when the impulse-normalised energy of the primary ring exceeds the impulse-normalised energy of the feeding shear layer. They also found that the formation time at which the primary ring pinches off is universal, because the pinch-off mechanism is independent of the piston velocity and does not depend strongly on the piston velocity programme (history). However, the numerical study of Rosenfeld *et al.* (1998) showed that the vortex formation number could be reduced by as much as 75%, or increased by 35%, by manipulating the temporal and spatial profiles of the nozzle exit velocity. The physics of the formation number was subsequently further explained by models in Mohseni & Gharib (1998) and Mohseni (2001) and by numerical results in Mohseni *et al.* (2001).

The numerical study in Mohseni *et al.* (2001) and later experimental study in Dabiri & Gharib (2005) suggested that stronger vortices (vortex rings with larger

[1]The flow visualisation results was also supported by Gan & Nickels (2007), in which an electrochemical method called 'Baker's method' was used to visualise laminar rings at large stroke lengths. One of the benefits of the method is that it does not involve any foreign scalar to mark the flow.

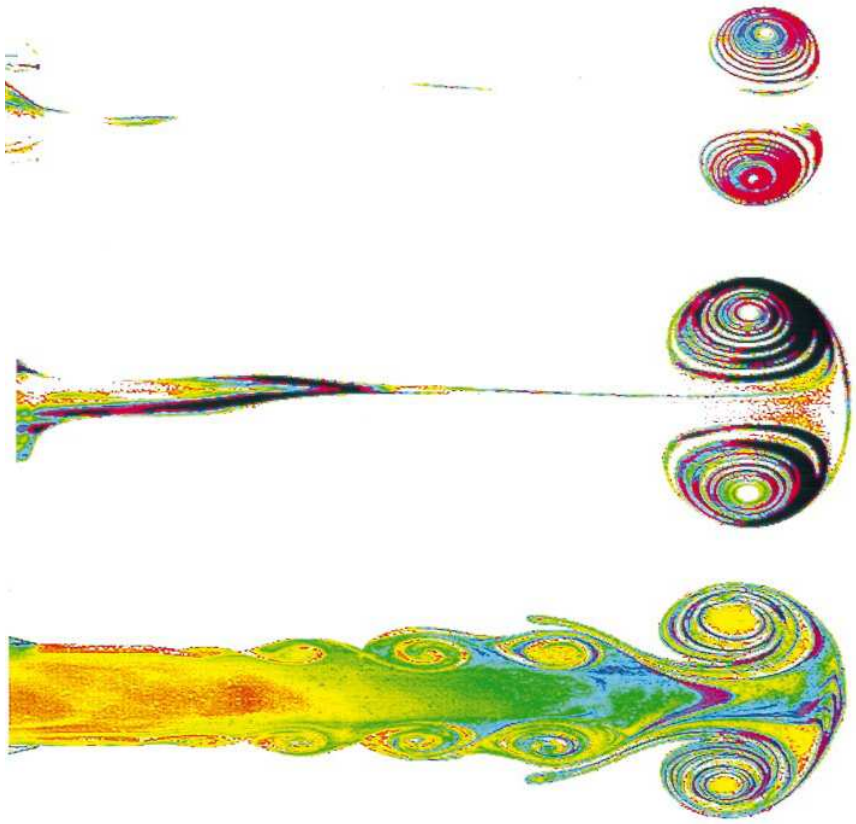

Figure 2.5: Visualisation of vortex rings at downstream position about nine nozzle diameters for $L/D = 2$, 3.8, 14.5, at a dimensionless time $U_p t/D = 8$. Figure taken from Gharib *et al.* (1998).

circulation) tend to be more energetic and therefore advance the formation number more rapidly; conversely, the vortex-formation process can be extended by either a stronger or a larger shear layer feeding the vortex ring, both of which tend to delay the advancement of the dimensionless vortex formation time. The formation number is also strongly influenced by the existence of a non-zero background flow (Dabiri & Gharib, 2004a; Krueger *et al.*, 2003): co-flow decreases the formation number while counter-flow increases it.

The concept of formation number was later adopted to explain some other general vortex shedding physics. For example, Jeon & Gharib (2004) studied the flow generated by a starting circular cylinder and by a steadily oscillating circular cylinder, aiming to identify the signature of optimal vortex formation in the wake; Milano & Gharib (2005) studied the vortex wake of an oscillating flat plate and applied a genetic algorithm to optimize the time-averaged thrust generated by the plate; Ringuette *et al.* (2007) studied the wake of an accelerating low-aspect-ratio flat plate, and investigated the pinch-off of the vortex pair behind the plate. These studies all suggested a universal formation number ≈ 4 by properly defining it in different configurations.

The physics of formation number is also closely related to the concept of optimal vortex formation in application of biological propulsion and physiological flow, which was mentioned in chapter 1 (e.g. the jellyfish swimming and the blood flow in the cardiac left ventricle). The entrainment of ambient fluid by the forming vortex ring, as well as the added mass of non-entrained fluid surrounding the vortex, must be accelerated with the vortex ring (Dabiri, 2009), and the propulsive reaction force experienced by the vortex generator is proportional to the sum of the shear layer source fluid, entrained fluid, and the added mass of the fluid surrounding the vortex ring (Dabiri, 2005).

Chapter 3

Experimental Methodology

This chapter introduces the facilities and the tools used to conduct the experiments of this study and the basic experimental conditions. A brief description of the apparatus to generate turbulent vortex rings is firstly given in section 3.1. The properties and component connections and arrangements of the investigation tool of this study-PIV are given in section 3.2. The PIV working principle with its detailed error analysis is a wide topic in experimental fluid mechanics, and is out of the scope of this dissertation. Finally, the experimental condition parameters are discussed and summarised in section 3.3.

3.1 Apparatus

The apparatus used in the project is the large vortex-ring rig in the hydraulics laboratory in the Engineering Department, which was designed in 2002. A sketch of this apparatus is presented in figure 3.1.

The rectangular tank is made of $15mm$ thick perspex with a bottom cross-sectional area of $750mm \times 750mm$ and a height of $1500mm$. The top of the tank is uncovered. The tank is therefore transparent from all viewing directions. A $940mm$ long tube made from $10mm$ thick perspex with an inner diameter of $\varnothing 146mm$ is vertically supported inside a metal frame, and the frame is mounted on the top of the tank. A PVC piston connected to a brass bar is inserted thought the tube to work as the piston-nozzle system. The outer diameter of the piston is about $\varnothing 144mm$ and the gap between the tube and the piston is sealed by two o-rings of

$\varnothing 6mm$. The diameter of the piston-nozzle system was specifically designed to give excellent spatial resolution to the vortex ring formed while there is still a significant distance from the nozzle to the tank wall to prevent any imaging effects. A perspex plate of $500mm \times 500mm \times 20mm$ is mounted horizontally and flush with the exit of the tube. A three-dimensional view of the tank is also sketched in figure C.1.

The motion of the piston is driven by a stepper motor supplied by SmartDrive Ltd. (SMR343-100-E-PN). The motor is wired such that it can provide up to $7Nm$ torque at a range of loaded rotation speeds. The motion of the stepper motor is controlled by a programmable controller Taranis (SmartDrive Ltd.). Taranis also connects to two limit switches to set the upper and lower bounds of the piston motion. The velocity programme of the piston motion is determined by programming a BASIC language written on a PC and uploaded onto the controller. Various velocity programmes can be specified but only a simple top-hat shaped programme imposing an impulsive start and stop was used in this research work. The motor is able to drive the piston at a constant speed of up to $1000mms^{-1}$ with an acceleration and deceleration of about $2000mms^{-2}$. The piston movement is carefully calibrated by a storage oscilloscope and a ruler. In particular, a potentiometer is attached to the motor shaft, and it is also connected to a storage oscilloscope. If the motor speed programme is strictly top-hat shaped, a straight slope will be displayed on the oscilloscope screen. The exact piston motion duration, read by the oscilloscope, together with the motion distance, gives the piston movement speed.

In order to study the longer distance/time range of rings, while maintaining reasonable spatial resolution, a small orifice of $D = 50mm$ is cut in the centre of a horizontal plate to make the ring generator orifice like. The geometry of this orifice is shown in figure 3.3. Such a configuration also has the benefit of eliminating the effect of the piston vortex on the primary vortex ring; see section 2.1 and Cater *et al.* (2004).

3.2 Image recording tools

Two-dimensional and stereoscopic PIV are used as the tools for this study. Two important reasons for the choice of PIV as the basic investigation tool is that, first it is a non-invasive method, i.e. the flow will not be affected by any instrument placed

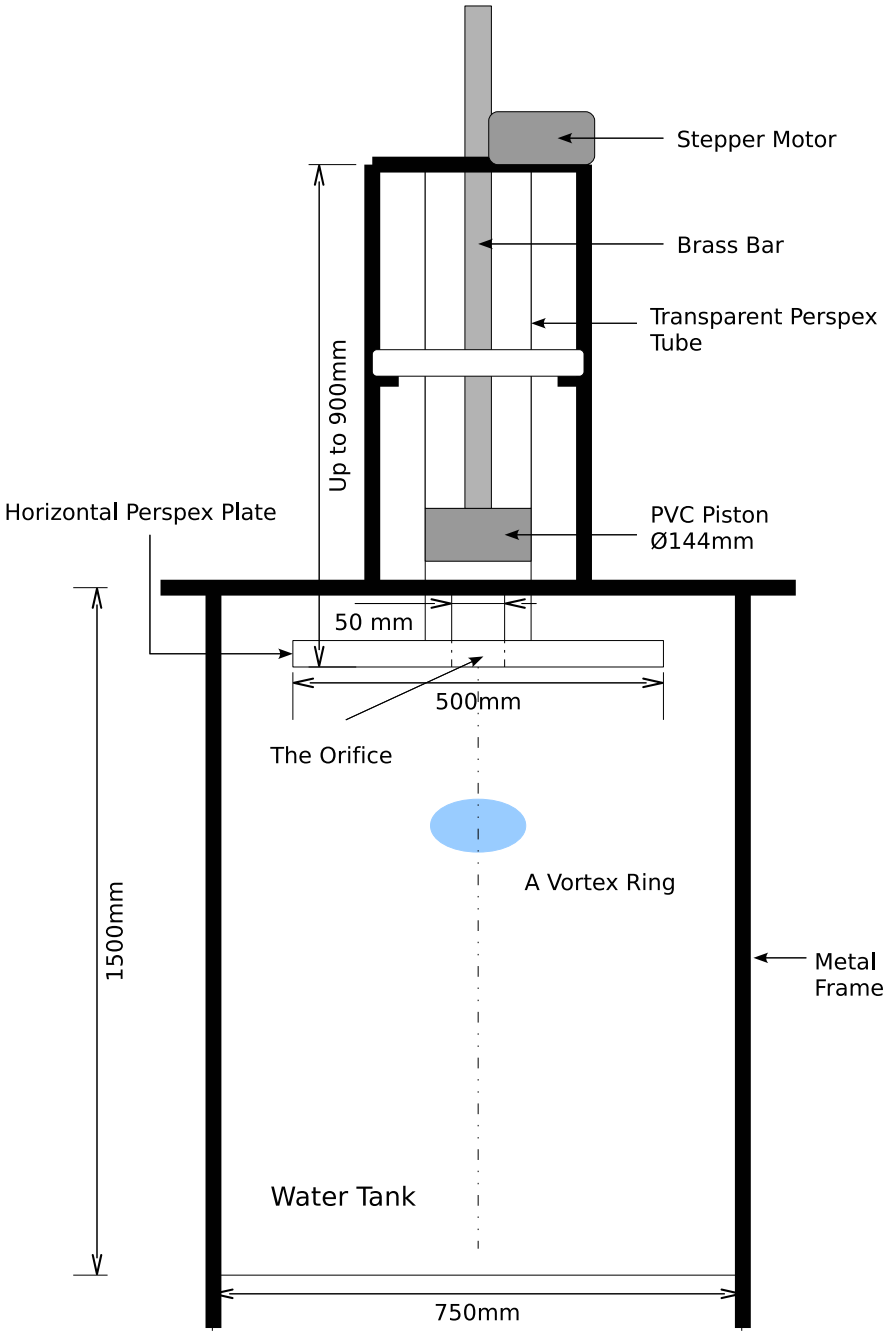

Figure 3.1: Schematic diagram of the vortex ring generator. The diagram is not to scale.

into the flow field; second, it can give planar information about velocities of two and three components. State-of-the-art camera also offers excellent temporal resolution. Moreover, because water will be used as the working media, seeding particles with proper size and density cause negligible distortion of the fluid flow and they can follow the flow precisely. One of the major weaknesses of such optical measurement tools is that they do not give a truly instantaneous velocity at a point. The velocity at a point is an averaged result of a very small volume (spatial resolution, depending on the cross-correlation interrogation window size) within a very short duration of time (PIV Δt). If single-frame single-exposure mode is used, PIV Δt also indicates the temporal resolution.[1] A Taylor series expansion of position at a point as a function of time, resulting from motion in an arbitrary direction is

$$\vec{r}(t+\Delta t) = \vec{r}(t) + \vec{v}(t)\Delta t + \frac{1}{2}\vec{a}(t)\Delta t^2 + ..., \tag{3.1}$$

where $\vec{r}$ denotes the position, Δt is the PIV Δt, $\vec{v}$ and $\vec{a}$ are the instantaneous velocity and acceleration respectively. Rearranging equation 3.1, the velocity can be written as

$$\vec{v}(t) = \frac{\vec{r}(t+\Delta t) - \vec{r}(t)}{\Delta t} + \mathcal{O}(\Delta t). \tag{3.2}$$

If a very small Δt is chosen, the error term can be neglected; as $\Delta t \to 0$, equation 3.2 gives the true instantaneous velocity at a point. The PIV Δt is restricted by the camera field of view (FOV) and the characteristic velocity scale of the flow (see Raffel *et al.*, 2007). In this study, PIV Δt values are in order of milliseconds.

Equation 3.1 also implies

$$\vec{r}(t-\Delta t) = \vec{r}(t) - \vec{v}(t)\Delta t + \frac{1}{2}\vec{a}(t)\Delta t^2 + ... \tag{3.3}$$

Thus, equation 3.1 can be added to equation 3.3, only if single-frame single-exposure mode is used, to given an estimation of acceleration, which can be written as

$$\begin{aligned} \vec{a}(t) &= \frac{\vec{r}(t+\Delta t) - 2\vec{r}(t) + \vec{r}(t-\Delta t)}{\Delta t^2} + \mathcal{O}(\Delta t^2) \\ &= \frac{[\vec{r}(t+\Delta t) - \vec{r}(t)] - [\vec{r}(t) - \vec{r}(t-\Delta t)]}{\Delta t^2} + \mathcal{O}(\Delta t^2) \\ &= \frac{\vec{v}(t) - \vec{v}(t-\Delta t)}{\Delta t} + \mathcal{O}(\Delta t). \end{aligned} \tag{3.4}$$

[1] Detailed explanations of terminologies: interrogation window size, PIV Δt, single-frame single-exposure mode, can be found in Lavision (2007b).

The last step is a reduction in accuracy level because of equation 3.2. Again, the error term can be neglected if a very small Δt is chosen. This acceleration can be applied to multiple points in space to compute the material derivative

$$\frac{D\vec{u}(x,y,z,t)}{Dt} = \frac{\partial\vec{u}(x,y,z,t)}{\partial t} + \vec{u}(x,y,z,t)\cdot\nabla\vec{u}(x,y,z,t), \tag{3.5}$$

and hence the pressure gradients in each direction with certain approximations made (see section 5.2.4).

The PIV system is provided by LaVision Ltd. The system consists of four components:

- *The PC* - A CCD-camera image acquisition and processing programme developed by LaVision Ltd., DaVis 7.2, is installed on the PC. All the raw images recorded by the cameras are stored in the PC and subsequently analysed by DaVis 7.2 to give the velocity information. The software is able to analyse both two-dimensional and stereoscopic PIV data. The working conditions, e.g. the camera recording frequency and duration, are also set in the software.

- *The cameras* - A pair of high-speed Photron APX cameras (LaVision HighSpeedStar 4) are used as the recording devices. They can either be lined up to provide a larger FOV, or be used to capture the information from the same area to give stereoscopic PIV data. Each camera has 2Gb buffer memory and is able to operate at $2000Hz$ recording rate at 1024×1024 pixels sensor resolution. The highest camera performance requirement of this study is $600Hz$ frame-rate and two seconds duration, which is far below their performance limit. The cameras are calibrated by a dual-plane calibration plate, and the image distortions (relatively weak in all the experiments of this study, because the refractive indices of water and perspex are close) are corrected by a third-order polynomial fitting process.

- *The laser* - The particle illumination is realised by a Pegasus-PIV Laser which consists of a dual-cavity diode pumped Nd:YLF laser head. Each of the heads is capable of emitting a beam of $527nm$ wavelength (green colour) and $10mJ$ energy under working conditions up to $2000Hz$, which is powerful enough to

illuminate the entire FOV and fast enough to cope with camera working frame-rates. Because in all the experiments of this study, single-frame single-exposure recording mode is used, only one of the two laser heads is needed. The laser beam is converted to a sheet by passing through a cylindrical diverging lens. The focal length of the cylindrical lens determines the sheet angle. The beam also passes through two coaxial telescope lenses before the cylindrical lens. The thickness of the sheet can be adjusted by changing the separation of the telescope lenses.

- *The programmable timing unit* - The programmable timing unit is the core device that takes the command from the PC and trigger the cameras and the laser to work in the designed manner. In this study, the start of the camera recording and hence the laser emission (controlled by the cameras) is triggered by the piston motion. The motor controller Taranis can be programmed to send a $5V$ TTL signal once the motor is energised. The TTL signal is used as the starting command.

A block diagram of all the device (the PIV system and the motor control system) connections, is shown in figure 3.5. The detailed description of all the devices and the explanations of the camera calibration process can be found in Lavision (2007c), Lavision (2007d), Lavision (2007e) and Lavision (2007b). The PIV working principles can be found in Raffel *et al.* (2007), Lavision (2007a), Lavision (2007b), Adrian (1991) and Prasad (2000).

3.3 Experimental conditions

Two-dimensional PIV experiments are carried out for two Reynolds numbers (different by a factor of two) in order to investigate the possible dependence of structural differences on Reynolds numbers. The Reynolds number for the vortex rings, based on circulation (equation 2.4) is calculated by converting the piston speed and the stroke length to those effectively for a smaller orifice. The water temperature, stabilised after 48 hours, is measured to be $21°C$ (measured by a thermocouple), which gives a kinematic viscosity ν of $0.984 \times 10^{-6} m^2 s^{-1}$. For the first condition, the effective Re_1 is set to 41280 ± 500 (written as 41280 for simplicity in the following

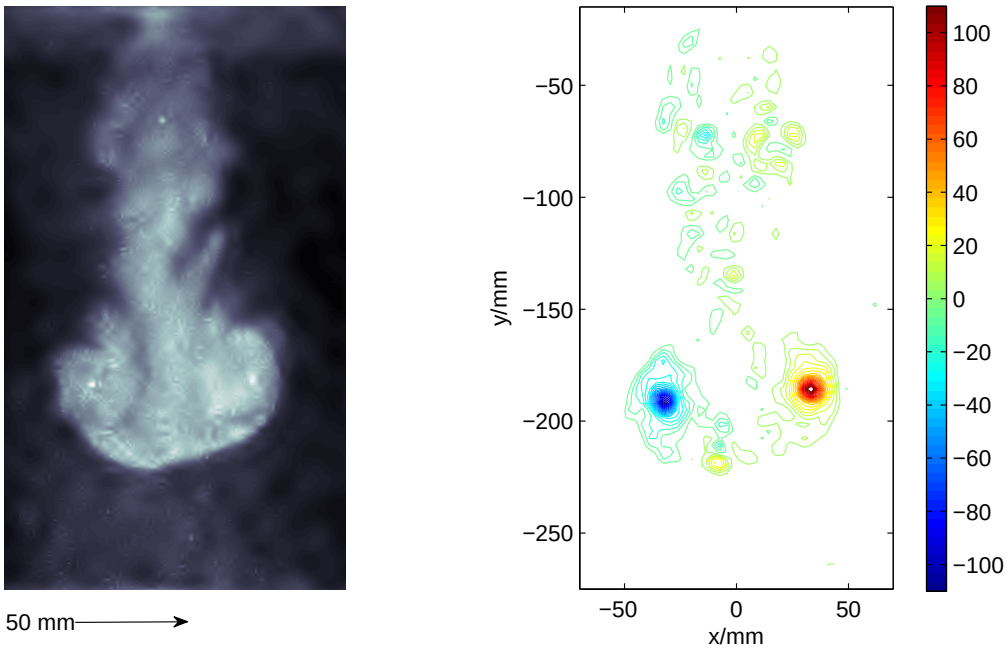

(a) (b)

Figure 3.2: (a): flow visualisation of ring's centre cross section, using wavelet-based denoised image of extremely high particle density at $Re = 20039$; (b): the corresponding vorticity field.

text) in order to match the one in Glezer & Coles (1990). Since the starting portion of the similarity theory (which starts from about $2.5D$ downstream of the nozzle exit, Glezer & Coles, 1990) is of interest, $-y/D$ is limited to eight (where $-y$ is the downstream distance measured from the orifice exit); for the second condition, the FOV is increased to about $10D$ and the effective Re_2 is set to 20039 ± 500 (written as 20039 for simplicity in the following text). The effective L/D ratio for the small orifice for both cases is also a match to Glezer & Coles (1990): 3.43. It must be pointed out that although the transition map in figure 2.3 indicates that at $Re \cong 20000$ and $L/D \cong 3.5$, the rings are in transition zone between laminar and turbulent regime, figure 3.2 suggests that the rings are already turbulent. In both cases, y is limited to the top half of the tank to eliminate the boundary effect from the tank bottom. The experimental set-up is summarised schematically in figure 3.3.

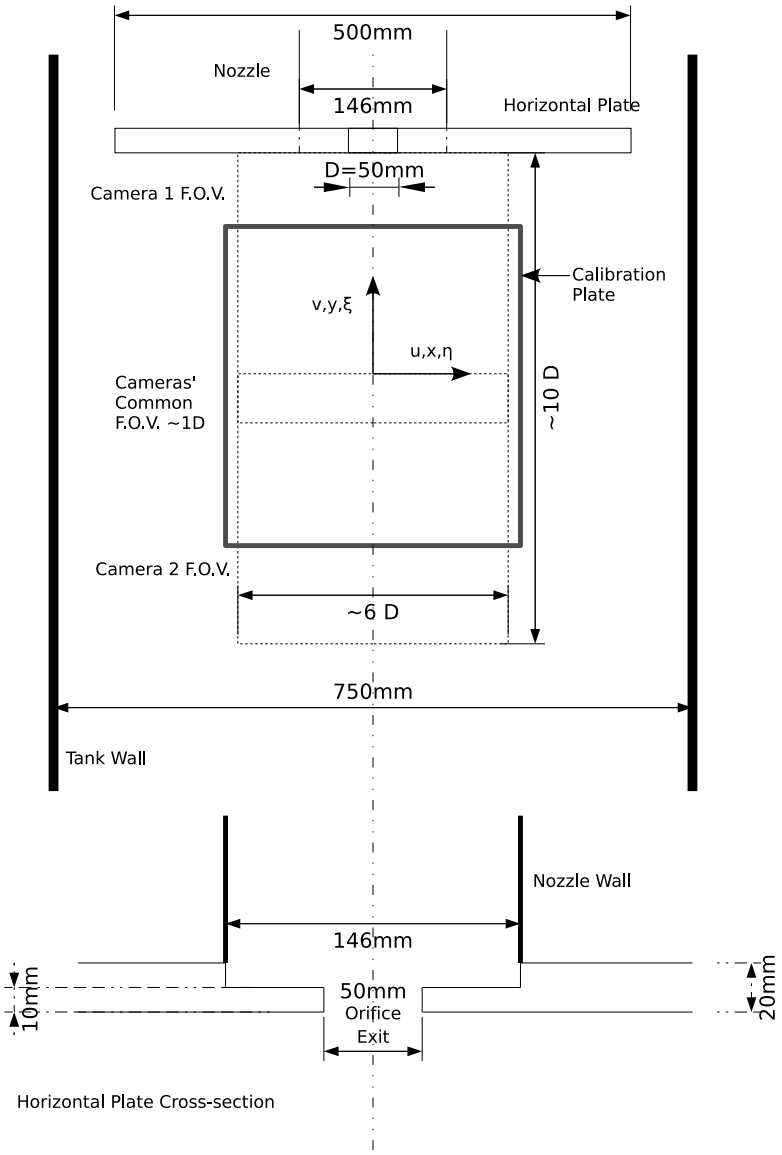

Figure 3.3: Schematic diagram of the testing section in the centre section of the tank (piston and motor not shown) and the centre section of the horizontal plate. The diagram is not to scale.

The centre of the measurement station for the first stereoscopic PIV recording[1] is at $224mm$ $(4.48D)$ downstream from the orifice exit. The FOV covers about $2.7D$ in the streamwise direction. A forward backward-scattering (FB) set-up is used, i.e. both cameras are on the same side of the laser sheet Lavision (2007b). After the water-perspex-air refraction is taken into consideration, the effective viewing angle between the two cameras is approximately 90^o, giving about the same resolution for in-plane and out-of-plane velocities. Figure C.1 (A) shows a sketch of the first stereoscopic recording set-up.

For both two-dimensional and stereoscopic experiments, the FOV is the centre cross-section of the tank parallel with the tank front wall, which also cuts the orifice diameter. Therefore the front top surface of the calibration plate needs to lie in this plane exactly, as does the centre plane of the laser sheet; see figure 3.3. The reason to choose the centre cross-section is apparent: this section reflects the ring diameter and all the quantities inferred from this section are equivalent when presented in Cartesian coordinates and cylindrical coordinates. The orientation of the laser sheet, due to the working-space restriction, is altered once from horizontal to vertical with the help of an optical-quality mirror placed underneath the tank at 45^o to the ground; see figure C.1 (A). The laser sheet is set at different thickness for two-dimensional and stereoscopic recording, respectively. It is typically $1-2mm$ for two-dimensional PIV and $4-5mm$ for stereoscopic PIV, because the third direction needs to be resolved. The laser thickness of the stereoscopic PIV was chosen such that particles with the maximum characteristic out-of-plane velocity typically displace about a quarter of the thickness within a chosen PIV Δt.

The two cameras run in single-frame single-exposure mode, which requires time-series cross-correlation PIV analysis. This mode gives the best possible temporal resolution, which equals the PIV Δt. Camera recording frequency under this mode determines the PIV Δt. They are set at 380 Hz (PIV $\Delta t \approx 2.6$ ms) for the two-dimensional Re_1 case, 200 Hz (PIV $\Delta t = 5.0$ ms) for the two-dimensional Re_2 case and 500 Hz (PIV $\Delta t = 2.0$ ms) for the first stereoscopic case.

The cross-correlation interrogation window size and overlap size are set to 16×16 pixels and 25% to give spatial resolution of $2.48mm$ and $3.15mm$ for the two-

[1]The second stereoscopic PIV recording is for the three-dimensional reconstruction method, which will be discussed in chapter 7.

dimensional Re_1 and Re_2 cases, respectively . They are set to 32×32 pixels and 50% overlap to give $2.15mm$ resolution for the first stereoscopic case. Note that these resolutions, in comparison with the ring diameter, are similar to that of Glezer & Coles (1990)'s LDV experiments. There are 85×85 data points in one camera's calculated vector mesh for two-dimensional PIV and 67×64 data points for stereoscopic PIV. The proper choices of the camera recording frequency (hence the PIV Δt) and the interrogation window size depend on the camera FOV size, as well as the characteristic velocity of the flow being measured.

The *Kolmogorov microscale* of length is defined as

$$\eta_\kappa = \left(\frac{\nu^3}{\epsilon}\right)^{\frac{1}{4}}, \tag{3.6}$$

where ν is the kinematic viscosity and ϵ is the energy dissipation rate per unit mass (Friedlander & Topper, 1962; Tennekes & Lumley, 1972). The internal dynamics of turbulence transfers energy from large scales to small scales and this energy transfer proceeds at a rate dictated by the energy of the large eddies (in order of u^2) and their time scale (in order of l/u). Because this energy must be dissipated, thus, the dissipation rate may be estimated as (Tennekes & Lumley, 1972)

$$\epsilon \sim u^2 \times \frac{u}{l} = \frac{u^3}{l}, \tag{3.7}$$

provided there exists only one l, where u and l are the characteristic velocity and length scales of the large eddies, i.e. in turbulent vortex-ring flows, $u \sim U_p$, $l \sim D$.[1] Substituting equation 3.7 into 3.6,

$$\eta_\kappa = \left(\frac{ul}{\nu}\right)^{-\frac{3}{4}} l = Re^{-\frac{3}{4}} l. \tag{3.8}$$

Therefore the spatial resolutions of this study are approximately: $140\eta_\kappa$ for the two-dimensional Re_1 case, $110\eta_\kappa$ for the two-dimensional Re_2 case and $120\eta_\kappa$ for the first stereoscopic case. The experimental parameters are also summarised in table 3.1.

Other optimal conditions, e.g. the size of the seeding particles (the density of the particles is usually required to be as close to the flow media density as possible),

[1] The estimation of the dissipation rate is sometimes made by assuming production rate balances dissipation rate. This argument, however, is not always correct. In some turbulent flows, e.g. grid turbulence, there is no production because of zero mean strain rate.

Case	PIV Δt	Temporal resol.	Spatial resol.	
2D Re_1	2.6 ms	2.6 ms	2.48 mm	$\approx 140\ \eta_\kappa$
2D Re_2	5.0 ms	5.0 ms	3.15 mm	$\approx 110\ \eta_\kappa$
1^{st} stereoscopic	2.0 ms	2.0 ms	2.15 mm	$\approx 120\ \eta_\kappa$

Case	Int. window size	Int. window overlap
2D Re_1	$16 \times 16\ pixel^2$	25%
2D Re_2	$16 \times 16\ pixel^2$	25%
1^{st} stereoscopic	$32 \times 32\ pixel^2$	50%

Table 3.1: Experimental parameters. $Re_1 = 41280$, $Re_2 = 20039$. η_κ: the *Kolmogorov microscale* of length. For 1^{st} stereoscopic PIV case, $Re = 41280$. Abbreviations: '2D': two-dimensional; 'resol': resolution; 'Int': interrogation.

particle seeding density (amount of particles per unit volume of the fluid), camera aperture size (camera exposure time in single-frame single-exposure mode is fixed by the frame-rate), parameter setting in the cross-correlation computations, post-processings etc. are explained in detail in Raffel *et al.* (2007) and Lavision (2007b).

Because the flow field of a vortex ring is neither stationary nor isotropic, the mean velocities used in turbulence quantity calculations can only be obtained from an ensemble-averaging process. In order to find the minimum number of realisations required for statistical convergence, 50 is used as the initial trial number to perform a convergence test. The time interval between firing vortex rings is set to about ten minutes, to allow velocity fluctuations in the tank to decay to a negligibly low level.[1] The convergence test is only applied to two-dimensional PIV experiments. The quantity designed for the the convergence criteria is written as

$$\tau_N = \frac{1}{N}\sum_{i=1}^{N}\left[(u_i - \overline{u_N})^2 + (v_i - \overline{v_N})^2\right], \tag{3.9}$$

where

$$\overline{u_N} = \frac{1}{N}\sum_{i=1}^{N} u_i \qquad \overline{v_N} = \frac{1}{N}\sum_{i=1}^{N} v_i, \tag{3.10}$$

and u, v are the radial and axial velocity component respectively as defined in figure 3.3. The quantity τ_N as a function of N is effectively the convergence speed

[1] This was verified by doing PIV measurements on the flow field just before firing the next vortex ring (at the end of the ten-minute time interval). Velocity field of negligible magnitude was obtained.

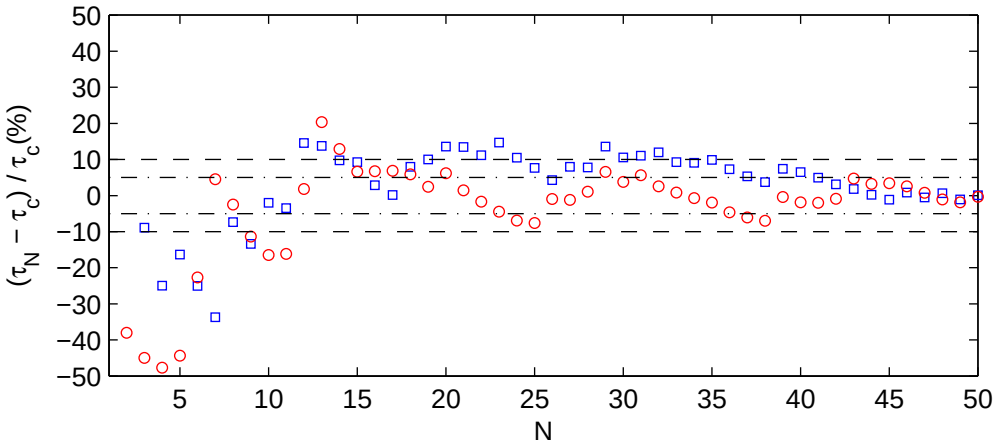

Figure 3.4: Convergence test for the number of realisations needed for each Re case. τ_N is defined in equation 3.9; $\tau_c = \tau_{50}$. The testing point's position is about $0.1D$ outside the left core centroid (in the core centre region) for both Re cases where the rings are at $5.5D$ downstream from the exit. ○: $Re_1 = 41280$; □: $Re_2 = 20039$. ——: $\pm 10\%$, — · —: $\pm 5\%$.

of the turbulent normal stresses. The result of the convergence test is presented in figure 3.4.

The convergence testing points for both Re cases are put in the core centre region, where the maximum turbulent stress intensities occur (see figure 5.23 and 5.24), therefore stresses there converge most slowly compared with stresses of points away from the core centre (see also Gan & Nickels, 2008). Figure 3.4 proves that 50 realisations should guarantee good convergence: after 40 realisations, it converges within $\pm 5\%$.

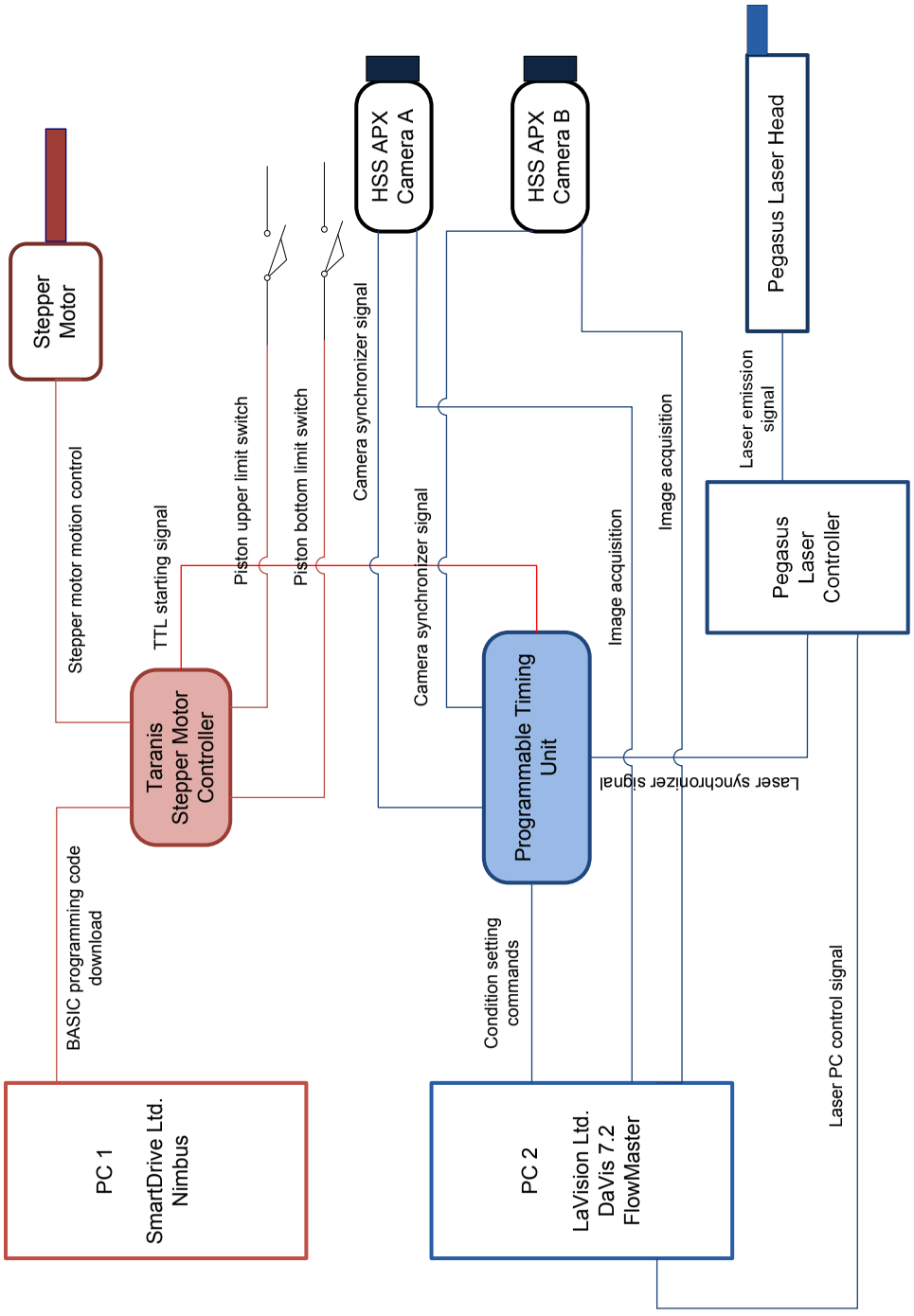

Figure 3.5: Wiring of the measurement systems. It shows the motor system (marked with red colour) and the PIV system (marked with blue colour). The only connection between the motor system and the PIV system is the TTL signal from Taranis, which is the starting signal of the image recording.

Chapter 4

Theoretical Background

In this chapter, the similarity theory derived in Glezer & Coles (1990) is briefly summarised and discussed. The important presumption of the theory: impulse invariance, is firstly discussed in section 4.1. The development of the theory, which is based on dimensional analysis, and the inferred scaling laws of various quantities are summarised in section 4.2.

4.1 The impulse invariance

Based on dimensional analysis, the streamfunction of vortex ring motion in unbounded fluid can be fully described by its hydrodynamic impulse I, the density of the fluid ρ and the kinematic viscosity ν. At the same time, the streamfunction is also a function of space and time. Therefore, the streamfunction can be written as

$$\psi = f(I, \rho, \nu) \tag{4.1}$$

$$= g(y, r, t), \tag{4.2}$$

where y and r are in cylindrical coordinates, r is the axis in the radial direction from the axis of symmetry, y is the axis in the streamwise direction from the orifice exit, and t is the time from the beginning of the piston movement. In Cartesian coordinates and in centre cross-section (the measurement plane in figure 3.3 or the laser plane in figure C.1 A), r is equivalent to $(x - x_o)$, where x_o is spanwise coordinate of the axis of the symmetrical flow field: the mean ring-centre trajectory

(see the centre-line mark in figure 3.1). The coordinate system adopted in this study is defined in figure 3.3. Hydrodynamic impulse hence can be written as

$$\boldsymbol{I} = \frac{1}{2}\rho \int_V (\vec{r} \times \vec{\omega}) \, \mathrm{d}V, \tag{4.3}$$

where $\vec{\omega}$ is the vorticity vector and V is the entire fluid volume.

A primary assumption in the derivation of the similarity theory is that the hydrodynamic impulse is an invariant. Maxworthy (1974) observed that the vortical structure is continuously shed from the main ring to the wake and concluded that a similarity transformation of the ring is not possible. Glezer & Coles (1990), however, argued that if the hydrodynamic impulse is considered as the total mechanical impulse of the non-conservative body force required to generate the velocity field from zero, and if the entire unbounded flow field is considered instead of just the main ring itself, this quantity should be considered as invariant. It will be shown in section 5.1 that, even when the entire flow field is considered and the flow structure is far away from the boundaries, the hydrodynamic impulse I is not very constant. In fact, a later study (Saffman, 1976) showed that the hydrodynamic impulse is not equivalent to mechanical impulse, and this point will also be further commented on in section 5.1.

4.2 The similarity theory

While the similarity transformation does not strictly require the invariance of the impulse (the local value could be used from a dimensional perspective), it is this assumption that leads to specific predictions for the variation of the other quantities of interest. As a result, it is difficult to directly test for similarity without making this assumption. If the invariance of the hydrodynamic impulse I is accepted, 4.1 and 4.2 can be rewritten as

$$\psi \left(\frac{\rho}{\nu I}\right)^{\frac{1}{2}} = f_2 \left[y \left(\frac{\rho\nu}{I}\right)^{\frac{1}{2}}, r \left(\frac{\rho\nu}{I}\right)^{\frac{1}{2}}, \frac{t\rho\nu^2}{I} \right]. \tag{4.4}$$

Equation 4.4 applies for both laminar and turbulent rings, because the viscosity is a parameter. If the Reynolds number is sufficiently high and the flow is highly turbulent, the dependence of the streamfunction on the kinematic viscosity ν can

be neglected, leaving only I and ρ to govern the flow (equation 4.1 and 4.4). Before the energy of the vortex ring dies out significantly the ring is still considered highly excited and turbulent. Mathematically, before the circulation Γ has decayed significantly, the ratio Γ/ν is still large and the effect of the kinematic viscosity is still considered negligible, i.e. the physics is essentially inviscid dominant, and ν can be dropped from equation 4.1. This is also one of the reasons why this experiment is limited to the early development of turbulent vortex rings: at large times viscous decay and cross-annihilation of vorticity will become important in the ring core area. Equation 4.4 then becomes

$$\psi t^{\frac{1}{4}} \left(\frac{\rho}{I}\right)^{\frac{3}{4}} = f_3 \left[y \left(\frac{\rho}{It}\right)^{\frac{1}{4}}, r \left(\frac{\rho}{It}\right)^{\frac{1}{4}} \right]. \tag{4.5}$$

With a proper pair of spatial and temporal virtual origins defined (y_o, t_o), equation 4.5 can be written as

$$S = \psi \left(t - t_o\right)^{\frac{1}{4}} \left(\frac{\rho}{I}\right)^{\frac{3}{4}} = S\left(\xi, \eta\right), \tag{4.6}$$

where S is the dimensionless streamfunction; ξ, η are the dimensionless quantities for the axial and radial coordinate y and r, respectively:

$$\xi = \left(y - y_o\right) \left[\frac{\rho}{I\left(t - t_o\right)}\right]^{\frac{1}{4}} \qquad \eta = r \left[\frac{\rho}{I\left(t - t_o\right)}\right]^{\frac{1}{4}}. \tag{4.7}$$

The velocity components can be derived from the streamfunction in cylindrical coordinates:

$$v = \frac{1}{r}\frac{\partial \psi}{\partial r} \qquad u = -\frac{1}{r}\frac{\partial \psi}{\partial y}. \tag{4.8}$$

Therefore, in similarity coordinates, the dimensionless velocities are

$$U = u \left(\frac{\rho}{I}\right)^{\frac{1}{4}} \left(t - t_o\right)^{\frac{3}{4}} \qquad V = v \left(\frac{\rho}{I}\right)^{\frac{1}{4}} \left(t - t_o\right)^{\frac{3}{4}}, \tag{4.9}$$

where u, v are the radial and axial velocity component respectively, as defined in figure 3.3; U, V are the corresponding dimensionless quantities. It is worth noting that equation 4.7 and 4.9 are of the same form in Cartesian coordinates and cylindrical coordinates if only the centre cross-section (the measurement plane in figure 3.3) is considered. Equation 4.8 has different forms in the two coordinate systems.

Hence the following set of rules must be satisfied if the rings are to obey the similarity property (and the impulse is invariant):

1. Take equation 4.7,

$$\frac{\xi}{\eta} = \frac{y - y_o}{r}, \tag{4.10}$$

$$r = \frac{\eta}{\xi}(y - y_o), \tag{4.11}$$

and because ξ and η are both constants,

$$r \sim (y - y_o). \tag{4.12}$$

2. The first equation in 4.7 also implies

$$\xi^4 = (y - y_o)^4 \left[\frac{\rho}{I(t - t_o)}\right], \tag{4.13}$$

$$(y - y_o)^4 = \xi^4 \left(\frac{I}{\rho}\right)(t - t_o), \tag{4.14}$$

and because ξ and (I/ρ) are both constants,

$$(y - y_o)^4 \sim t - t_o. \tag{4.15}$$

3. From the second equation of 4.9,

$$V^{\frac{1}{3}} = v^{\frac{1}{3}} \left(\frac{\rho}{I}\right)^{\frac{1}{12}} (t - t_o)^{\frac{1}{4}}, \tag{4.16}$$

$$v^{-\frac{1}{3}} = V^{-\frac{1}{3}} \left(\frac{\rho}{I}\right)^{\frac{1}{12}} (t - t_o)^{\frac{1}{4}}, \tag{4.17}$$

and because V and I/ρ is are both constants, using 4.15,

$$v^{-\frac{1}{3}} \sim (t - t_o)^{\frac{1}{4}} \tag{4.18}$$

$$\sim (y - y_o). \tag{4.19}$$

The essence of the similarity theory is that, if the scaling law is correct, with a pair of virtual space and time origins located, the virtual origins just play the role of the 'singular point' of the universe. In other words, all the quantities associated with the turbulent vortex ring, e.g. peak vorticity, circulations, stresses and turbulence productions or even dissipation, when properly scaled, would collapse on to straight rays (with positive slopes) or on conical surfaces which come out from the origins.

Because positive slopes are not very intuitive when viewing decaying quantities; for instance, the circulation of the ring decays, hence it may be counter-intuitive to see a positive slope, even if it has been scaled. All the data presented in this dissertation are thus plotted following the common method of similarity theories' representations, which will be explained later.

This similarity theory is not valid for the entire history of a vortex ring. When significant circulation is lost, the viscous effect will become dominant, so ν cannot be dropped from equation 4.1, and all the scaling laws need to be reconsidered.

Chapter 5

Results and Discussion

This chapter presents the experimental results given by the ensemble-averaging process. One-dimensional results are presented in section 5.1 and two-dimensional contour information is given in section 5.2.

5.1 The similarity property

This section gives the evolution of various basic and important quantities describing the turbulent vortex rings: ring growth rates, peak velocities, celerities, core sizes, bubble volumes, entrainment fractions, and circulations, as functions of downstream distance, or time, from section 5.1.1 to 5.1.7. These results show that the evolution of these quantities are basically Reynolds number independent, in the language of similarity scaling laws. A detailed study of vorticity shedding manner of a typical individual turbulent vortex ring is described in section 5.1.8, which is found to be unsteady predominantly. The presumption of the similarity theory: impulse invariance, is revisited and commented in section 5.1.9 with the support of the experimental data.

5.1.1 Ring growth rates

The simplest test of the similarity theory is to consider the validity of equation 4.12, the variation of the ring radius as a function of streamwise distance. The results are shown in figure 5.1. The ring size is determined by locating the centroids of both cores in the measurement plane and each core is defined by the area which is

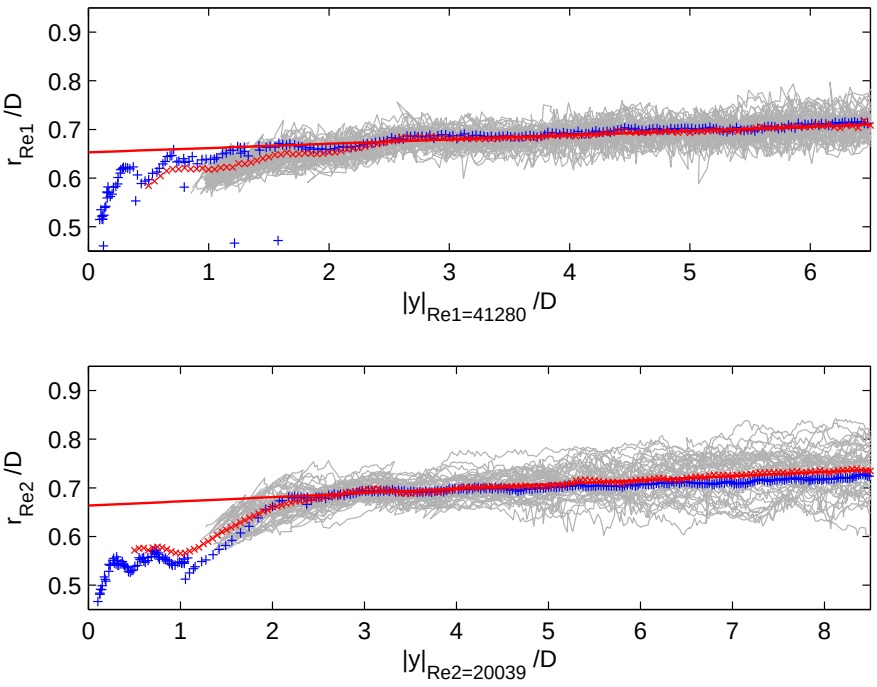

Figure 5.1: Ring-bubble radius r as a function of downstream distance for both Reynolds numbers. The grey lines are traces of each of the 50 realisations; $\times$: the ensemble-averaged radius based on location; $+$: the ensemble-averaged radius based on arrival time; $-$: the first-order least-squares fit of $\times$ for $|y|/D \geqslant 3.5$.

enclosed by a contour of 40% of the peak vorticity of the local core area. The 40% vorticity criterion is not a unique definition of core size. The vorticity contours in individual rings are usually very noisy, and the 40% threshold thus puts more weight on the near-core vorticity and gives a more reliable core centroid location. A more rigorous investigation of core sizes will be given in section 5.1.4.

The Cartesian coordinates of the core centroid x_Λ and y_Λ are calculated by the following formulas:

$$x_\Lambda = \frac{\iint x\omega \mathrm{d}x\mathrm{d}y}{\iint \omega \mathrm{d}x\mathrm{d}y} \qquad y_\Lambda = \frac{\iint y\omega \mathrm{d}x\mathrm{d}y}{\iint \omega \mathrm{d}x\mathrm{d}y}, \tag{5.1}$$

where ω is the vorticity of the azimuthal component, or the component normal to

the measurement plane, i.e. in two-dimensional Cartesian coordinates,

$$\begin{aligned} \vec{\omega} &= \nabla \times \vec{u} \\ &= \left(\frac{\partial v}{\partial x} - \frac{\partial u}{\partial y} \right)_z \\ &= \omega_z. \end{aligned} \tag{5.2}$$

The Pade approximation is used to calculate the differentiation in equation 5.2 numerically, which gives an error of $\mathcal{O}\left[(\Delta x)^4, (\Delta y)^4\right]$ (see Moin, 2001). Pade approximation is an implicit scheme which requires the solution of a matrix equation. Note that at $L/D \cong 3.5$, formation wake phenomena appear (see Gharib *et al.*, 1998) and due to the highly turbulent nature of the rings, vorticity is continuously shed from the ring bubble area. There are two points worth emphasising here:

1. Gharib *et al.* (1998) indicated that the formation wake starts to be visible for $3.6 \leqslant L/D \leqslant 4.5$, while in this experiment, at $L/D = 3.43$ a significant formation wake is already observed. Two reasons may be responsible for the shorter formation time: first, more energetic or stronger vortices can advance the formation time more rapidly (see section 2.4); second, a different ring-generator configuration is used in this experiment, which may influence the shear layer stability.

2. The detailed vorticity shedding deserves further study. The falling of the ring bubble circulation from the ensemble-averaged results seems to show a continuous loss (see figure 5.15), but the ensemble-averaging process can smear some interesting details of the individual behaviour. The vorticity shedding pattern of an individual ring is further discussed in section 5.1.8.

To minimize the error in determining the centroids, the wake is excluded when determining the core area. It is worth noting that individual realisations are also very important in the study of turbulent vortex rings, since the inevitable dispersion in core position and geometry tends to smear out actual behaviour. It is for this reason that each of the 50 individual realisations is plotted (grey lines in figure 5.1). Moreover, since the y-axis, the downstream position, is plotted as the abscissa, it is more sensible to ensemble-average quantities based on location.

The entire FOV is divided into a number of stations along the streamwise direction starting from the orifice exit; see figure 5.2. The distance between neighbouring stations is $0.05D$. All the 50 realisations are ensemble-averaged when the apparent centre of the ring bubble (judged from the locations of the two core centroids) reaches each station, regardless of the arrival time (indicated by the PIV image number). The difference of the arrival times of the 50 rings is very small, which will be indicated later in section 5.2.1.

As can be seen in figure 5.1, compared with the result of averaging based on arrival time (the plus sign data), averaging based on stations(the cross sign data) fits the individual trace zone (grey zone) better, especially at early times. A first-order least-squares fit is applied for stations after $3.5D$ downstream of the orifice exit, from which the virtual origins can be determined, which are $y_o = +74.32D$ for Re_1 rings and $y_o = +76.37D$ for Re_2 rings. The '+' sign indicates *upstream* of the orifice exit level.

Furthermore, from the slopes of these fitting lines, the (ring bubble) growth rates (cone angles) can also be estimated, which are 0.0176 and 0.0174 respectively. These numbers are comparable with the results of early experiments: the cone angles typically vary from 0.0091 to 0.0168, in Johnson (1970), Sallet & Widmayer (1974) and Glezer & Coles (1990). The agreement with the early research is one reason why this plot is used to determine the virtual origin. Note that different approaches are used to determine the ring radius in this study compared with some of the early research, where flow visualisation was used. Core vorticity centroids are not always located at the rotating centre of a passive scalar, especially for turbulent cores, for which the vorticity contour is not always exactly circular. Hence the growth rate here is slightly different from the flow visualisation results.

Individual traces for Re_2 are obviously more scattered. The reason is that a turbulent vortex ring has an azimuthal wave-like instability, similar to that analysed for laminar and transient rings in section 2.3; see figure 2.4, 7.2 and 7.3. For the lower Reynolds number case, the rings move slower so the waves may have bigger amplitudes at the same streamwise location. This situation makes the core centroids look more scattered in the measurement plane. Due to their turbulent nature, the shed vorticity from the core along the azimuthal direction is highly unlikely to be uniform, the consequence of which is the uneven distribution of local circulation

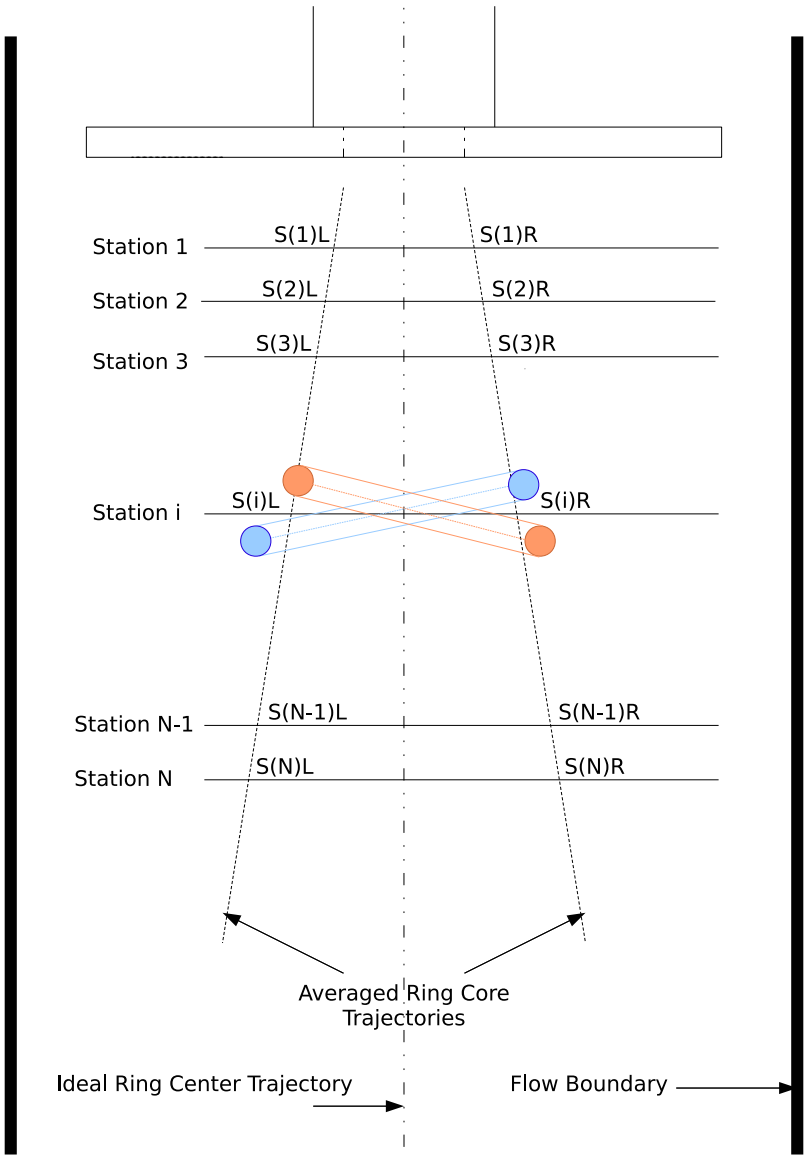

Figure 5.2: Illustration of virtual stations in the flow field. The neighbouring stations are spaced for $0.05D$, where D is the orifice diameter. Station 1 is at $0.5D$ downstream from the orifice exit. Two typical vortex rings are shown when they reach the station i. The variation of the core positions is exaggerated.

along the azimuthal direction, causing the ring to tilt and disperse from the mean trajectory. These are important properties of turbulent vortex rings, hence one cannot apply an artificial treatment such that the cores appear exactly on top of each other. This point will be returned to in section 5.2.

5.1.2 Peak velocities

The virtual origins just estimated are used to determine other similarity quantities. First the peak velocity in the field of interest (FOI) is plotted against streamwise distance in figure 5.3. The peak instantaneous velocity, which is in the axial direction, is located on the centre of the ring bubble axis. This axis is shown as the ideal ring centre trajectory in figure 5.2, for the ensemble-averaged ring. The dimensionless peak velocity V_{peak} can be calculated from equation 4.9 and 4.14 as

$$\begin{aligned} V_{peak} &= v_{peak}\left(\frac{\rho}{I}\right)^{\frac{1}{4}}(t-t_o)^{\frac{3}{4}} \\ &= v_{peak}\left(\frac{\rho}{I}\right)^{\frac{1}{4}}\left[(y-y_o)^4\,\xi^{-4}\left(\frac{\rho}{I}\right)\right]^{\frac{3}{4}} \\ &= v_{peak}\left(\frac{\rho}{I}\right)(y-y_o)^3\,\xi^{-3}. \end{aligned} \tag{5.3}$$

Both plots in figure 5.3 show that similarity theory slightly underestimates the decay of the peak velocity.[1] The disagreement is less clear for Re_1 rings, where it is only noticeable at the last few points, but it is reasonable to anticipate that the deviation will grow further downstream. It is worth emphasising, that this is the quantity which Glezer & Coles (1990) used to determine the virtual origin, via a free first-order least-squares fit applied to a $v_{peak}^{-1/3}$ against y plot (equation 4.19), which is shown in figure 5.4. The fitting lines of these figures indicate a different pair of virtual origins: $+51.72D$ and $+43.86D$ for Re_1 and Re_2 rings respectively. If these origins are fixed in equation 4.12, a first-order least-squares fit of figure 5.1 would not be as good and the growth rate (the cone angle) indicated would be unreasonably large, if compared with the early experiments.

[1] In this dissertation, when quantities are plotted as a function of ring streamwise distance and scaled accordingly to the similarity theory, they will be constant, if the similarity theory is satisfied.

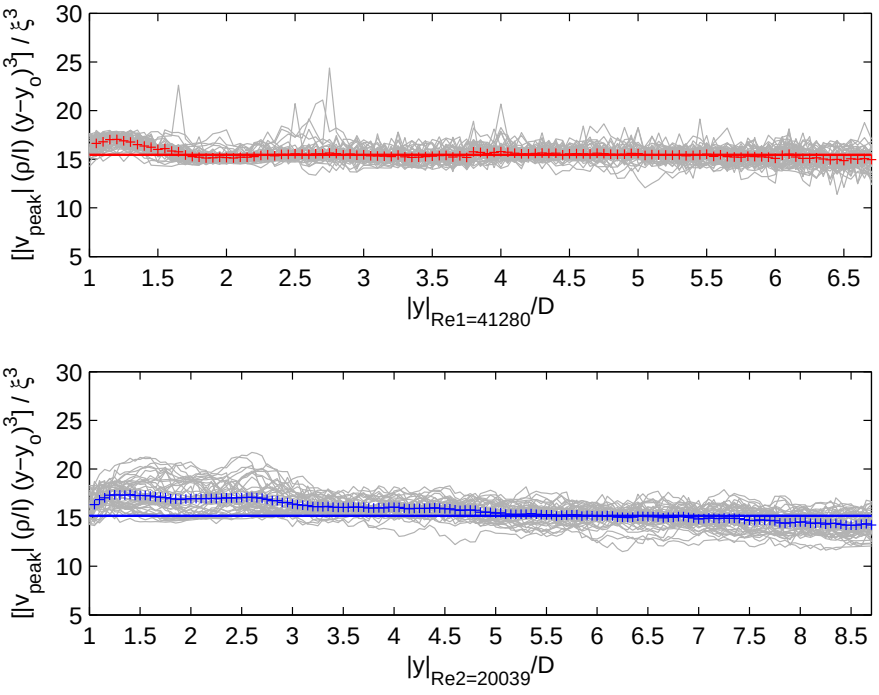

Figure 5.3: Peak axial velocity v_{peak} on the ring centre trajectory as a function of downstream distance. Velocity is scaled accordingly to similarity theory. Grey lines are the traces of each of the 50 realisations; $+$: the ensemble-averaged value from individual realisations; $-$: the zero-order least-squares fit of $+$ for $|y|/D \geqslant 3.5$, which represents the perfect similarity-theory fitting. The virtual origin y_o is obtained from figure 5.1.

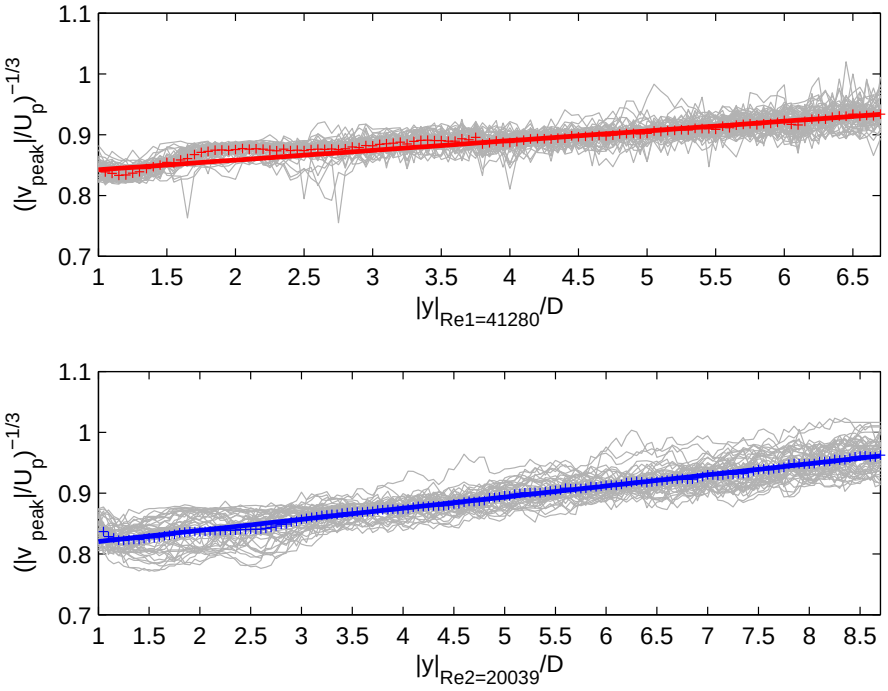

Figure 5.4: The fitting of v_{peak} on the ring centre trajectory to downstream distance. Grey lines are the traces of each of the 50 realisations; $+$: the ensemble-averaged value from individual realisations; $-$: the first-order least-squares fit of $+$, for $|y|/D \geqslant 3.5$.

5.1.3 Ring celerities

Interestingly, the results of this experiment show that the similarity theory seems to predict the ring translation speed, or celerity, very well. Because the ring bubble and the ring core structure can be clearly observed moving downstream at a certain speed, it is possible to numerically compute this speed based on the ring core streamwise location as a function of time. If equation 4.7 is differentiated, the equation for translation speed can be obtained. Equation 4.7 can be rearranged to be

$$(y - y_o) = \xi \left(\frac{I}{\rho}\right)^{\frac{1}{4}} (t - t_o)^{\frac{1}{4}}. \tag{5.4}$$

Differentiate y with respect to time t,

$$\begin{aligned} u_t = \frac{\mathrm{d}y}{\mathrm{d}t} &= \frac{1}{4}\xi \left(\frac{I}{\rho}\right)^{\frac{1}{4}} (t - t_o)^{-\frac{3}{4}} \\ &= \frac{1}{4}\xi \left(\frac{I}{\rho}\right)^{\frac{1}{4}} \left[(y - y_o)^4 \xi^{-4} \left(\frac{\rho}{I}\right)\right]^{-\frac{3}{4}} \\ &= \frac{1}{4}\xi^4 \left(\frac{I}{\rho}\right) (y - y_o)^{-3}. \end{aligned} \tag{5.5}$$

Therefore,

$$\xi = \left[4u_t \left(\frac{\rho}{I}\right) (y - y_o)^3\right]^{\frac{1}{4}}. \tag{5.6}$$

From equation 4.9 and 5.5, the dimensionless celerity can be written as

$$\begin{aligned} U_t &= u_t \left(\frac{\rho}{I}\right)^{\frac{1}{4}} (t - t_o)^{\frac{3}{4}} \\ &= \frac{1}{4}\xi \left(\frac{I}{\rho}\right)^{\frac{1}{4}} (t - t_o)^{-\frac{3}{4}} \left(\frac{\rho}{I}\right)^{\frac{1}{4}} (t - t_o)^{\frac{3}{4}} \\ &= \frac{1}{4}\xi. \end{aligned} \tag{5.7}$$

The dimensionless streamwise distance $|\xi|$ is plotted in figure 5.5. The strong noise at the beginning is due to the incomplete formation process: the main ring has not pinched off yet. Note that according to Maxworthy's turbulent vortex ring model (see appendix A), C_D takes a value between 1.8 and 2.7. Equation A.11 then gives a scaling law: $u_t \sim (y-y_o)^{-4.8} - (y-y_o)^{-5.7}$, which would not give a reasonable fit for the current data. This is one of the reasons Maxworthy's model is not used as

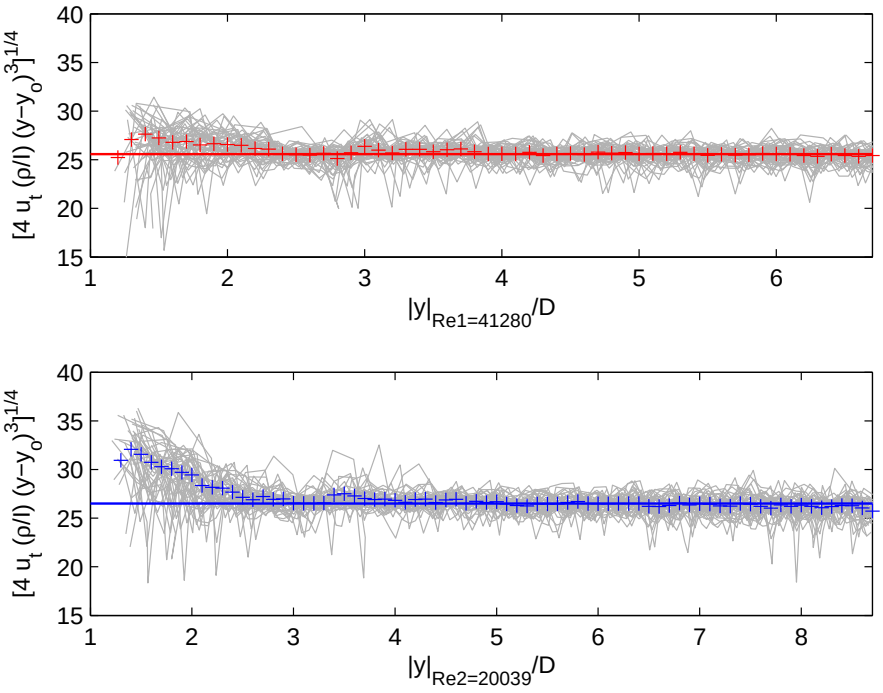

Figure 5.5: Ring celerity u_t scaled accordingly to similarity theory. The dimensionless quantity $|\xi|$ is determined from this plot, which is the quantity on the ordinate; the dimensionless celerity $U_t = (1/4)\,\xi$. Grey lines are the traces of each of the 50 realisations; $+$: the ensemble-averaged value from individual realisations; $-$: the zero-order least-squares fit of $+$ for $|y|/D \geqslant 3.5$, which represents the perfect similarity-theory fitting. The virtual origin y_o is obtained from figure 5.1.

the best candidate of the theoretical support for this study. The discrepancy could be mainly due to the different experimental approaches - PIV experiments give much higher spatial and temporal resolution than the experiment in Maxworthy (1974).

5.1.4 Ring core size

The measured/computed ring celerities can be compared with theoretical celerities. Theoretically, a vortex ring with a thin core propagates at a speed u_t^* which depends

on its instantaneous parameters, and can be written as[1]

$$u_t^* = \frac{\Gamma}{4\pi R_b}\left\{\log\left(\frac{8R_b}{\delta}\right) + C + \mathcal{O}\left[\frac{\delta}{R_b}\log\left(\frac{\delta}{R_b}\right)\right]\right\}, \tag{5.8}$$

where the asterisk is used to differentiate the theoretical value from the measured one; Γ is the circulation of the ring, R_b and δ respectively denote the instantaneous ring bubble and core radii, and C is a constant depending on the core vorticity distribution profile. For a Gaussian core vorticity distribution, $C \approx -0.558$ (Lim & Nickels, 1995; Saffman, 1970; Shariff & Leonard, 1992), where Gaussian core vorticity distribution (as a function of the radial distance r, from the peak) is given as

$$\omega(r) = \frac{\Gamma}{\pi\delta^2}\exp\left[-\frac{r^2}{\delta^2}\right]. \tag{5.9}$$

Equation 5.8 works well for a thin core ring with an isolated bubble volume, therefore it makes sense to equate Γ to the bubble circulation instead of the total circulation for the turbulent ring case, because the shed circulation from a turbulent ring bubble is usually weak and in a rather random distribution pattern, and thus does not produce self-induced propagation velocity. Also because the equation is derived for steady laminar rings, velocities calculated from ensemble-averaged rings are compared with u_t^*. The instantaneous bubble circulation can be obtained from figure 5.15, and the averaged instantaneous ring bubble radius can be obtained from figure 5.1, thus they give an instantaneous theoretical speed u_t^*. The ring core radius need to be determined.

Because the vorticity distribution in the core area is roughly described by a two-dimensional Gaussian distribution, it is difficult to find a characteristic threshold to define the core radius with a strong reason. (If the distribution is a two-dimensional top-hap shaped, the radius can be definitely defined at the discontinuities.) A different useful definition is therefore adopted here. The ring core radius is considered to be "the radius at which the tangential velocity is at a maximum" (Saffman, 1978). This point will be revisited later. Thus, as long as the points of the core centroid and the points of the maximum tangential velocity can be located, the radius is computable.

[1] Strictly speaking, because equation 5.8 is only valid for a thin-cored *steady* laminar vortex ring, it is not valid for a thick core turbulent ring. This equation is not expected to describe the ring velocity particularly well, it merely serves as a theoretical reference.

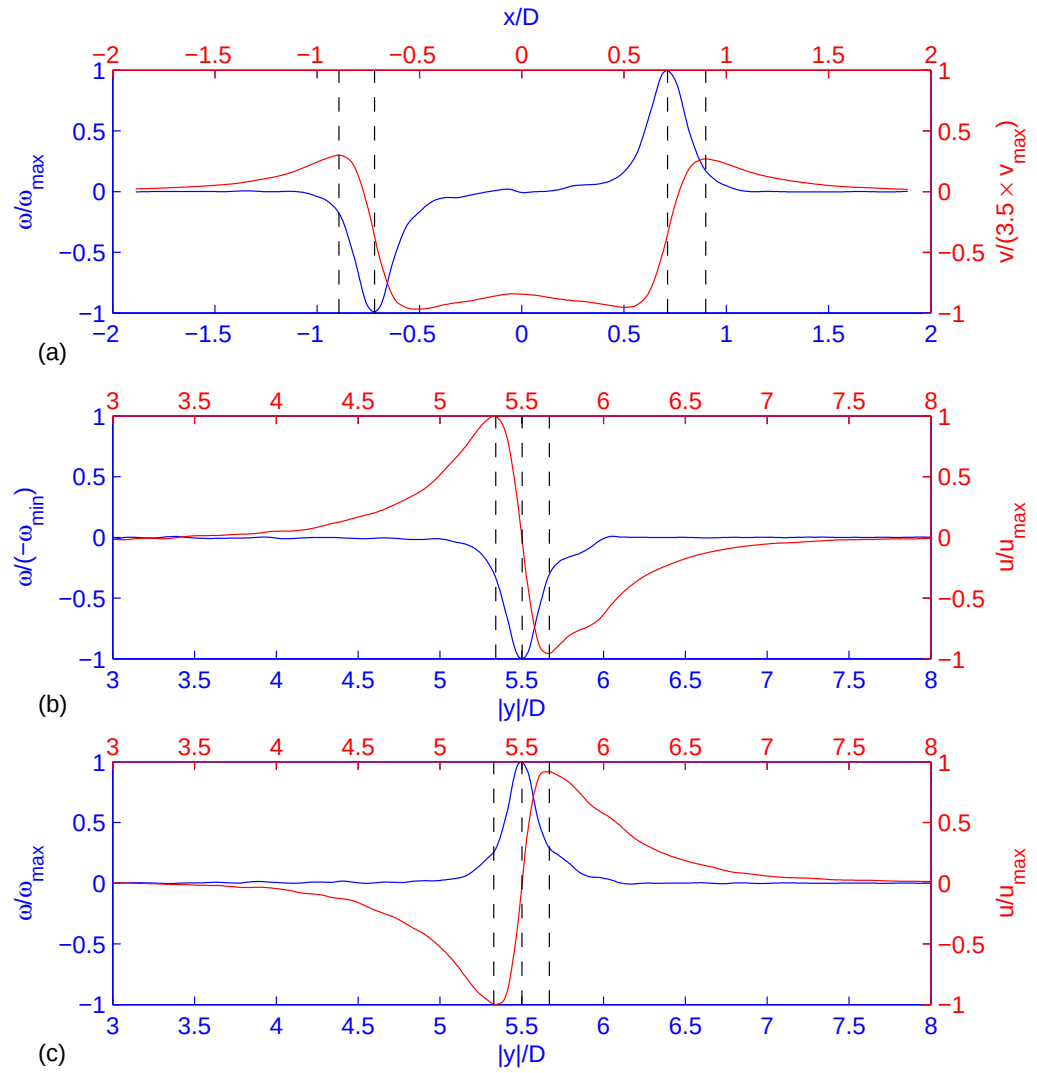

Figure 5.6: This figure shows the method used to determine the ring core size. The ensemble-averaged vorticity and velocity fields when the rings reach $5.5D$ downstream of the orifice exit after the core centroid shifting correction method (section 6.2) is plotted. Traces – denote the vorticity profiles, Traces – denote the velocity profiles, –– show the six distances characterising the core size. $Re = 20039$. (a): spanwise cut through the ring centre; (b) and (c): streamwise cut through the two cores.

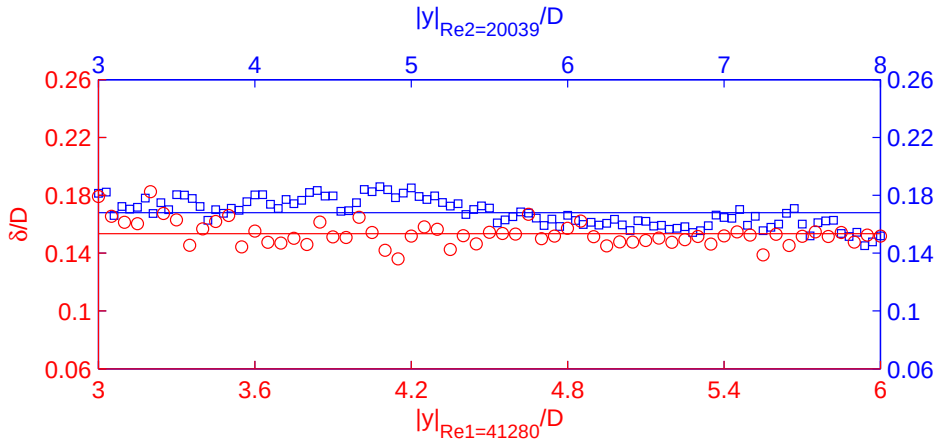

Figure 5.7: The ring core sizes as a function of streamwise distances for both Reynolds numbers. □ $Re = 20039$; ○ $Re = 41280$. The two solid lines are the averaged core sizes.

In figure 5.6, the ensemble-averaged $Re = 20039$ ring at 5.5 orifice diameters downstream is used to illustrate the method to compute the core radius. The way of calculating the core centroid position has been discussed in section 5.1.1. Slices in radial and axial directions are cut through the ring bubble centre location (spanwise) and the two core centroids (streamwise), respectively. Hence there are six points characterising the core radius. For instance, from figure 5.6(a), two cores radii are determined by locating the two maximum positive axial velocities and the corresponding core centroids; figure 5.6(b) illustrates that radius of the left core is determined by locating the extreme magnitudes (both positive and negative) of the radial velocities; similarly, figure 5.6(c) is for the right core. The six characteristic radii are averaged to quantify the core radius at 5.5D downstream.[1] The results of the core radius for the two Reynolds numbers are plotted in figure 5.7.

It must be stressed that the core radius computed from the ensemble-averaged

[1]Ideally, to clearly identify the contours of the maximum tangential velocity, the ring should be put in a reference frame such that the ring moves at the same speed as the observer, as in section 5.1.5. By changing the reference frame, closed contours of various tangential velocities enclose the corresponding core can be marked theoretically. However, because these contours are not necessarily perfectly circular and the centroid does not necessarily locate the exact centre, it is extremely difficult, if not impossible, to find the tangential angle along the contour, therefore difficult to identify the contour of the maximum tangential velocity. This method was thus abandoned.

velocity and vorticity contours is strongly correlated with the level of apparent dispersion, i.e. at a more downstream location, the radius would appear larger, and this would not be the true radius. Therefore in order to exclude the dispersion effect, the averaged vorticity and velocity contours used in calculating the radius are the ones after the centroid position shift corrections (see section 6.2). Note that the circulation is computed from the ensemble-averaged vorticity contour. The results would be the same if individual circulation were computed first, before the averaging process, because

$$\overline{\Gamma} = \overline{\oint_C \vec{u} \cdot \, \mathrm{d}\mathbf{r}} = \oint_C \overline{\vec{u}} \cdot \, \mathrm{d}\mathbf{r}. \tag{5.10}$$

It may be a little counter-intuitive to see the ring core radius decrease downstream. The reason could be, first, that at such high Reynolds numbers, vorticity viscous diffusion is relatively weak and the duration of time for the plotted distances is too short for the vorticity diffusion to make a significant effect, and moreover, as mentioned before, the vortex stretching due to the increase of ring-bubble diameter can cancel the vorticity diffusion effect; second, the ring core radius is not uniform in the azimuthal direction due to its turbulent nature (see figure 7.2 or 7.3), which influences the ensemble-averaged results. The scattering in radius for both Reynolds numbers in figure 5.7 are within 10% of the averaged value.

The determination of the core radius by the maximum tangential velocity criteria is not arbitrary. It can be shown by a simplified analytical model that, this radius is closely related to the standard deviation of a Gaussian distribution. For the sake of easy analysis, the vorticity distribution around a vortex ring core is assumed to be axisymmetric Gaussian about the core centre. In the centre plane of the ring (the PIV measurement plane, see figure 3.3), there are effectively two axisymmetric Gaussian cores with one positive valued and the other negative. Mathematically, a simplified model of equation 5.9 can be written as

$$\omega(r) = A \exp\left(-\frac{r^2}{\delta_s^2}\right), \tag{5.11}$$

where δ_s is the standard deviation of the Gaussian distribution, r is the radius from the origin and $A = \omega(0)$, which is a constant.

A single perfect two-dimensional Gaussian core (described by equation 5.11) is now considered. It is here further assumed that the Gaussian distribution in

equation 5.11 is the cross-section of an infinitely long filament and it is isolated, i.e. there is no influence from the existence of the other core. If the geometrical centre of this ideal core is placed in the origin of a two-dimensional polar coordinate system (r, β), by the definition of circulation, the tangential velocity $v_\beta(r)$ can be written as

$$v_\beta(r) = \frac{\Gamma(r)}{2\pi r}. \tag{5.12}$$

Here it is assumed that the the tangential velocity is not a function of angular position β. The radial velocity $v_r(r)$ is orthogonal, and is irrelevant to the calculation of the circulation $\Gamma(r)$. From equation 5.24, $\Gamma(r)$ can be deduced from the vorticity distribution

$$\Gamma(r) = \int_0^r \omega(r) 2\pi r \, \mathrm{d}r. \tag{5.13}$$

Combining equation 5.11, 5.12 and 5.13,

$$\begin{aligned} v_\beta(r) &= \frac{1}{2\pi r} \int_0^r A \exp\left(-\frac{r^2}{\delta_s^2}\right) 2\pi r \, \mathrm{d}r \\ &= -\frac{1}{2}\delta_s^2 \frac{A}{r} \int_0^r \exp\left(-\frac{r^2}{\delta_s^2}\right) \mathrm{d}\left(-\frac{r^2}{\delta_s^2}\right) \\ &= \left(\frac{A\delta_s^2}{2}\right) \frac{1}{r} \left[1 - \exp\left(-\frac{r^2}{\delta_s^2}\right)\right]. \end{aligned} \tag{5.14}$$

Now let $\alpha = r/\delta_s$, such that equation 5.14 reduces to

$$v_\beta(\alpha) = \left(\frac{A\delta_s}{2}\right) \frac{1}{\alpha} \left[1 - \exp\left(-\alpha^2\right)\right]. \tag{5.15}$$

The radius where the maximum tangential velocity occurs can be found by plotting the function

$$f(\alpha) = \frac{1}{\alpha} \left[1 - \exp\left(-\alpha^2\right)\right], \tag{5.16}$$

or by finding the root of

$$\frac{d[f(\alpha)]}{d\alpha} = 0. \tag{5.17}$$

Equation 5.16 and 5.17 are plotted in figure 5.8. It is clear that $v(\beta)$ is at its maximum at $\alpha = 1.12$, or $r = 1.12\delta_s$. In order to compare the maximum $v(\beta)$ to the experimental value, it is necessary to calculate δ_s. This is done by fitting a Gaussian distribution to the measured averaged core vorticity distribution. The

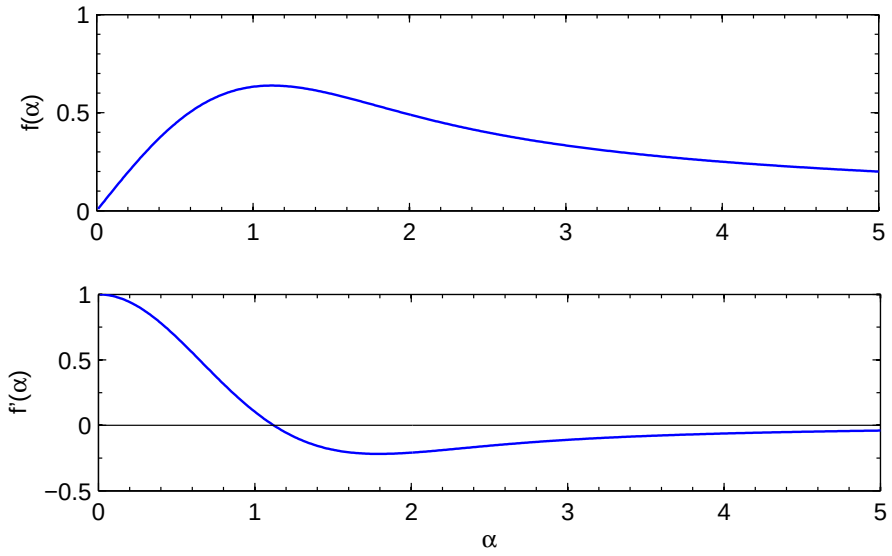

Figure 5.8: Determination of the location of the theoretical maximum tangential velocity

four characteristic vorticity distributions illustrated in figure 5.6 (two in (a) and one in each of (b) and (c)), are first normalised by their maximum values (thus $\omega(0) = 1$ in equation 5.11) and then averaged. A Gaussian curve is then fitted to find the standard deviation corresponding to the minimum r.m.s. value. The Gaussian fit is shown in figure 5.9.

Figure 5.9 gives $\delta_s = 0.141D$ as a best fit, which then further gives a radius where maximum $v_\beta(r)$ locates: $r = 1.12 \times 0.141D = 0.158D$. Figure 5.7 reads a value of $0.171D$ at $5.5D$ for $Re = 20039$ rings. The difference between the measured radius and the theoretical one is $0.013D$, or $1.3\%D$. The small discrepancy is due to the imperfect Gaussian core of the experimental data (see figure 5.9) and the assumptions made for deriving the analytical radius.

Because the computed instantaneous radius has an undesired scattering (figure 5.7), the averaged core radius is used in equation 5.8 to calculate the theoretical ring celerities u_t^*. The measured and the theoretical celerities are plotted in figure 5.10 for both Reynolds numbers. The trend of the measured values agrees very well with the theoretical ones but the theory overestimates the true celerities. This is again because, first, equation 5.8 assumes thin-core laminar rings and sec-

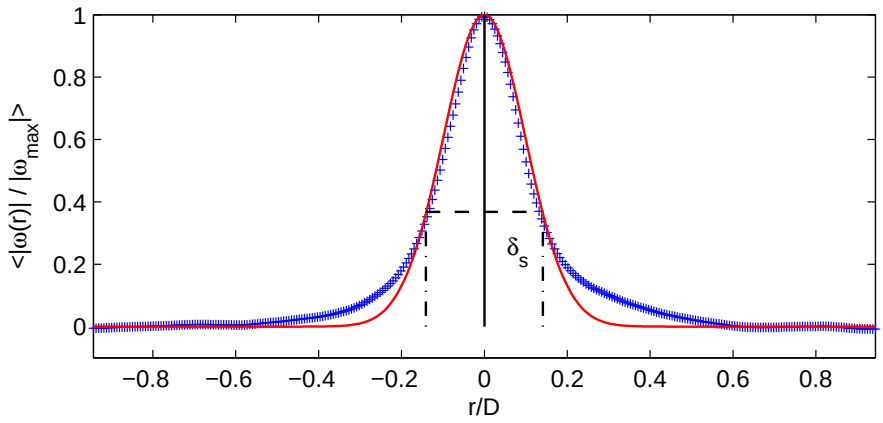

Figure 5.9: The Gaussian fit of the core vorticity distribution calculated from measured velocities. $+$ denotes the averaged experimental vorticity value, on a horizontal slice through one of the core centroids, $-$ denotes the Gaussian fit, equation 5.11. $\langle\rangle$ denotes the averaging of four characteristic vorticity curves. Note that the experimental data (a 85×85 matrix for one camera, see section 3.3) has been refined by a factor of ten by two-dimensional cubic spline interpolation, in order to improve the fitting quality.

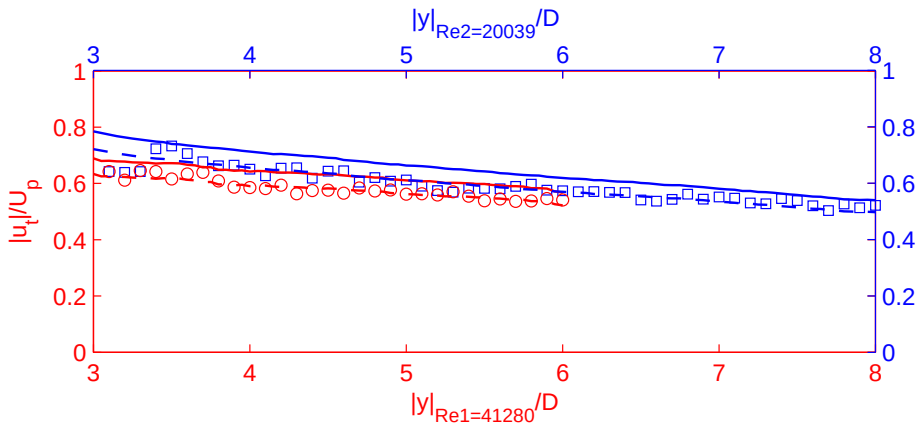

Figure 5.10: The theoretical ring celerities denoted by the two solid lines versus the measured ones. $\square$ denotes the $Re = 20039$ case and $\circ$ denotes the $Re = 41280$ case. $--$ denotes the recalculation of equation 5.8 with $C = -0.8$

ond, the core vorticity is not strictly Gaussian (see figure 5.9), which affects the value C takes in equation 5.8. The influence on the theoretical celerity by the core radius is insensitive because of the logarithmic term, with 10% change of δ causing a 3% change of u_t^*. This means that whether it is strictly a thin-core ring or not is not sensitive to the theoretical celerity. Nevertheless, the neglected term is $\mathcal{O}\left[\delta/R_b \log\left(\delta/R_b\right)\right] \sim \mathcal{O}\left(-0.3\right)$; if this term corrects C to take an effective value of -0.8 in the computation of equation 5.8, then the theoretical curves fit the measured data very well; see figure 5.10.

5.1.5 Ring bubble volume

If the ring translation velocity is subtracted from the ring's instantaneous velocity field, the resultant velocity field will be that of an observer moving at the same velocity as the ring, i.e. the reference frame will be moving at the same velocity as the ring. Assuming that the ring is completely isolated, two stagnation points can be found with one located at the windward tip and the other at the leeward tip. Because of the existence of a wake, only the windward stagnation point is easily recognised but that is enough to determine the stagnation streamline which forms an open ellipse. Figure 5.11 shows a typical ensemble-averaged vortex ring in the moving reference frame, in which the vortex-ring bubble is clearly seen and only one of the stagnation points - the windward stagnation point - can be determined. The streamlines are plotted by a time advancing scheme of *virtual* particles in a *frozen* velocity field, such that they are tangential to the velocity vector everywhere.

The streamlines can also be plotted by computing the streamfunctions numerically. If the velocity field is assumed to be perfectly axisymmetric, in cylindrical coordinates, the streamfunction ψ is associated with the azimuthal vorticity ω_θ by:

$$\frac{\partial^2\psi}{\partial y^2} + \frac{\partial^2\psi}{\partial r^2} - \frac{1}{r}\frac{\partial\psi}{\partial r} = -\omega_\theta r \tag{5.18}$$

or

$$\frac{\partial^2\psi}{\partial y^2} + \frac{\partial^2\psi}{\partial r^2} - u_y = -\omega_\theta r, \tag{5.19}$$

where r, y, θ represent the radial, axial and azimuthal directions in the cylindrical coordinate system. With proper mixed boundary conditions set ($\psi = 0$ on the axis of symmetry; $\partial\psi/\partial y = -u_r r$ on the top and bottom boundaries; $\partial\psi/\partial r = u_y r$ on

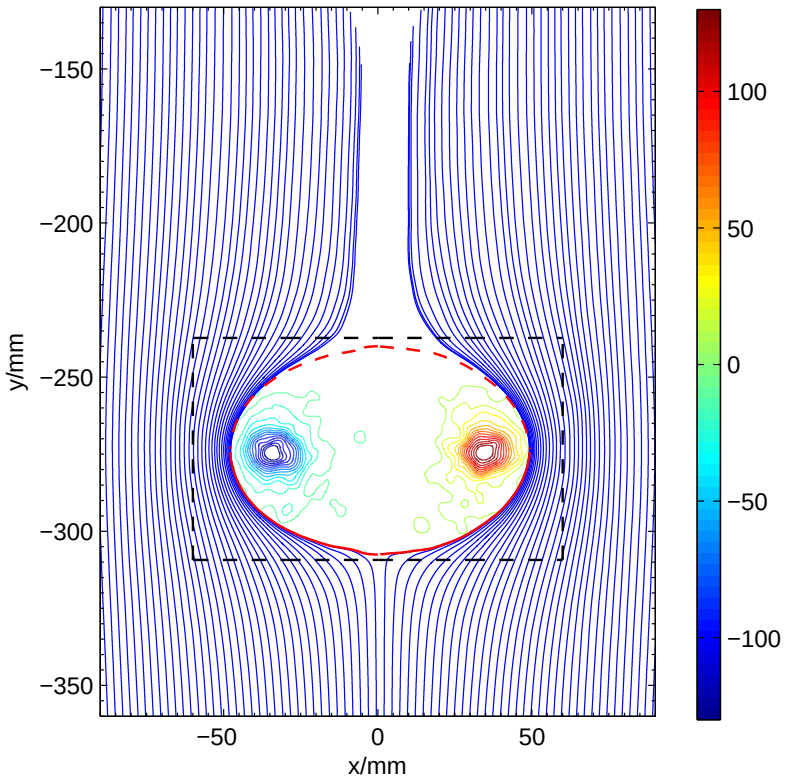

Figure 5.11: The streamline pattern of an ensemble-averaged vortex ring of $Re = 41280$ in a reference frame moving at the same velocity as the ring at $5.55D$ downstream from the orifice exit. The colour bar denotes the absolute vorticity intensity of the ring with the unit of sec^{-1}. – denotes the traced stagnation streamline which ends at the maximum radius; –– denotes the mirror imaged of – based on the centre-line. – denote the streamlines. The black –– box will be explained in section 5.2.2.

the maximum radial distance boundary), streamfunctions can be computed by a two-dimensional implicit method (Moin, 2001). Therefore, not only the pattern of the streamlines, but also the numerical value of each streamline can be known. The streamfunction value is not required for determining the bubble volume; the pattern is almost the same as shown in figure 5.11, so it is not shown here.

With the approximation that the bubble is an axisymmetric oblate spheroid, (the red-coloured solid and broken lines in figure 5.11 show that the centre section of the bubble in the PIV measurement plane is close to an ellipse), it is possible to compute the volume of the bubble by numerical integration. In order to locate the windward stagnation point more precisely, the original data-point mesh is first refined by a factor of ten using two-dimensional cubic spline interpolation, after which this refined mesh is also used to increase the accuracy of the numerical integration scheme. The volume of the ring bubble can be approximated by

$$\Omega_{bubble} = 2 \times \int_{y_a}^{y_b} \pi r^2(y)\, \mathrm{d}y, \tag{5.20}$$

where y_a denotes the y coordinate of the windward stagnation point and y_b denotes the y coordinate of the point at the centre of the ellipse; $r(y)$ is determined by the stagnation streamlines, with $r(y) = 0$ on the axis of symmetry.

The ring bubble volume can be represented by a dimensionless variable $\widehat{\Omega}$, by taking equation 4.7 and 4.14:

$$\begin{aligned}
\Omega &= 2 \int_{y_a}^{y_b} \pi r^2(y)\, \mathrm{d}y \\
&= 2 \int_{\xi_a}^{\xi_b} \pi \left\{ \eta \left[\frac{I}{\rho} (t - t_o) \right]^{\frac{1}{4}} \right\}^2 \mathrm{d} \left\{ \xi \left[\frac{I}{\rho} (t - t_o) \right]^{\frac{1}{4}} \right\} \\
&= 2 \int_{\xi_a}^{\xi_b} \pi \eta^2 \left(\frac{I}{\rho} \right)^{\frac{1}{2}} (t - t_o)^{\frac{1}{2}} \left(\frac{I}{\rho} \right)^{\frac{1}{4}} (t - t_o)^{\frac{1}{4}}\, \mathrm{d}\xi \\
&= 2\pi \left(\frac{I}{\rho} \right)^{\frac{3}{4}} (t - t_o)^{\frac{3}{4}} \int_{\xi_a}^{\xi_b} \eta^2\, \mathrm{d}\xi \\
&= 2\pi \left(y - y_o \right)^3 \xi^{-3} \int_{\xi_a}^{\xi_b} \eta^2\, \mathrm{d}\xi \\
&= \left(y - y_o \right)^3 \xi^{-3} \widehat{\Omega}.
\end{aligned} \tag{5.21}$$

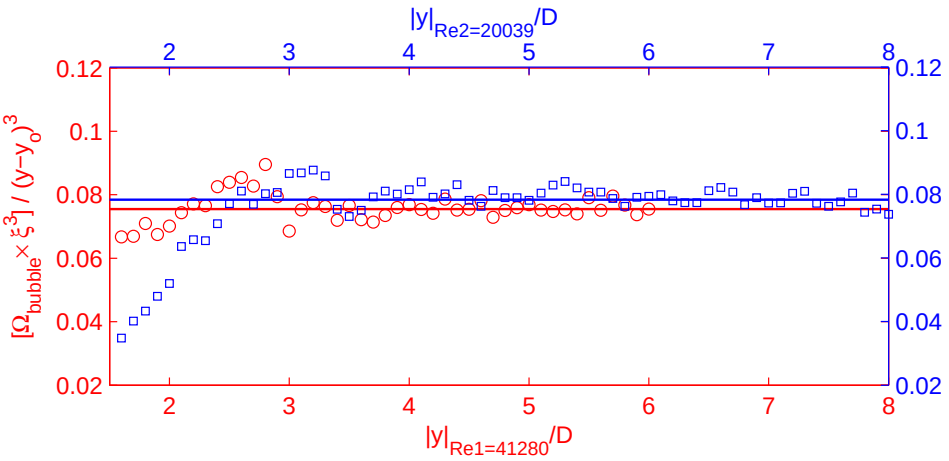

Figure 5.12: Ring bubble volume as a function of downstream distance calculated from the ensemble-averaged velocity field. ○: Re_1 rings; □: Re_2 rings. The volume is scaled accordingly to the similarity theory. − the zero-order least-squares fit for $|y|/D \geqslant 3.5$, which represents the perfect similarity-theory fitting. The virtual origin y_o is obtained from figure 5.1.

Hence

$$\widehat{\Omega} = \frac{\xi^3 \Omega}{(y - y_o)^3}. \tag{5.22}$$

The scaled ring volume as a function of streamwise distance is plotted in figure 5.12.

It can be observed that the two data sets obey the similarity theory quite well after 3.5D. There is a subtle waviness in the two data sets, which may indicate an oscillation of the ensemble-averaged ring bubble. The reason for this is left for future study. It may be related to vorticity shedding from the core area or it may be related to the waviness on the core changing the imaged cross-sectional area (and hence the inferred ensemble-averaged volume).

5.1.6 Entrainment fraction

Fluid entrainment fractions for vortex rings can also be computed from the ring bubble volumes. The entrainment fraction is defined in the same way as Dabiri & Gharib (2004b) for the purpose of comparing the quantity to that of the laminar

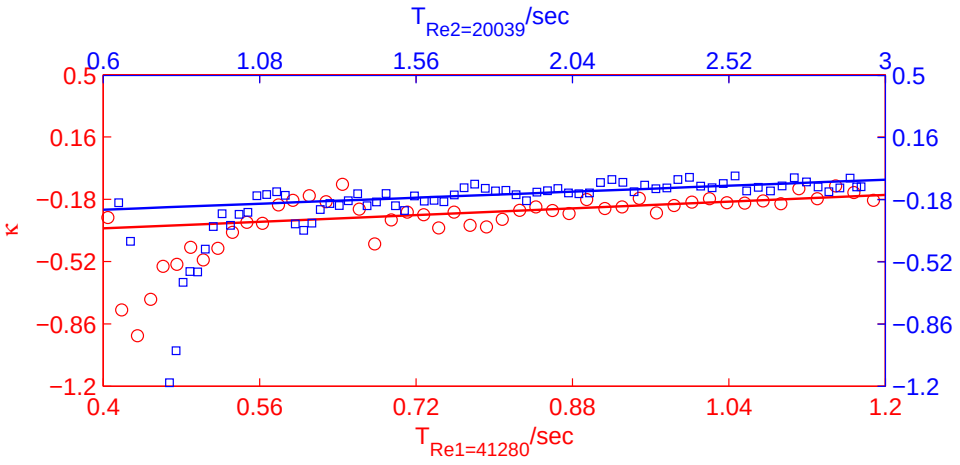

Figure 5.13: The entrainment fraction κ as a function of time calculated from the ensemble-averaged velocity field. ○: Re_1 case; □: Re_2 case. − the first-order least-squares fit for $T \geqslant 0.72sec$ and $T \geqslant 1.56sec$ for Re_1 and Re_2 rings, respectively.

rings'.

$$\kappa(t) = \frac{\Omega_{bubble}(t) - \Omega_{ejected}(t)}{\Omega_{bubble}(t)} = 1 - \frac{\Omega_{ejected}(t)}{\Omega_{bubble}(t)}, \tag{5.23}$$

where κ is the entrainment fraction, Ω_{bubble} is the ring bubble volume, $\Omega_{ejected}$ is the total volume of the fluid ejected from the orifice during the formation process and all three quantities are functions of time. In contrast to the laminar rings of comparable L/D in Dabiri & Gharib (2004b), which indicate an entrainment fraction of about 0.3, figure 5.13 shows two major differences: first the entrainment fraction is negative, meaning that the ring bubble volume is smaller than the fluid volume ejected from the piston nozzle, in which the formation wake is responsible for the missing part; second the laminar ring shows a fairly constant entrainment fraction as a function of time while entrainment fractions in figure 5.13 increase with time with slopes of 0.050 and 0.033 for Re_1 and Re_2 respectively. Note that the bubble volumes of turbulent rings at two Reynolds numbers are similar at the same downstream distances as shown in figure 5.12 but $Re = 41280$ rings travels much faster than the $Re = 20039$ rings; the ratio of the real celerities of the two Res can be calculated from figure 5.5.

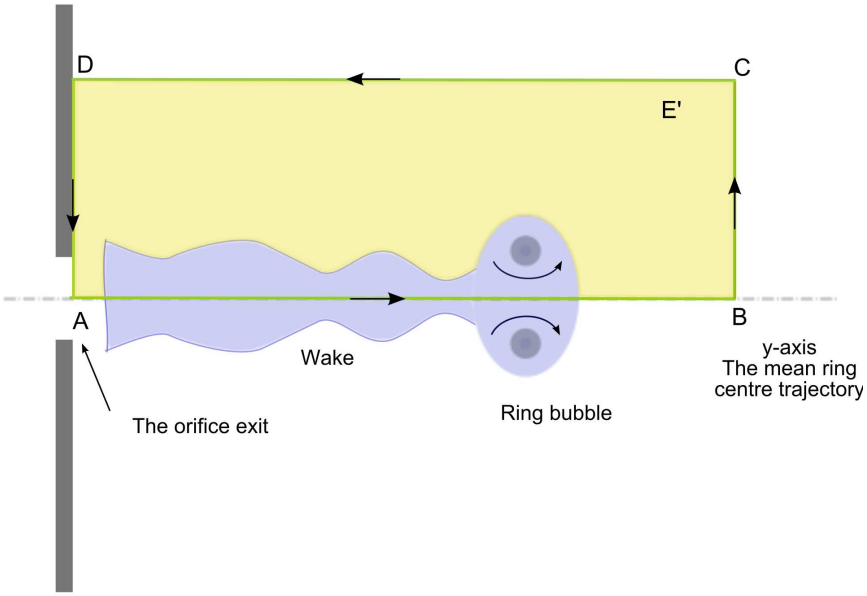

Figure 5.14: Schematic diagram of the contour of the circulation integral.

5.1.7 Circulation

As mentioned above, vorticity is continuously shed from the ring bubble volume to the wake and it is in the wake where most cancellation and annihilation of opposite-signed vorticity takes place. This mechanism causes the circulation of the ring bubble area and the entire FOV to decrease. The circulation of a vortex ring is defined as a line integral of the closed loop $A \rightarrow B \rightarrow C \rightarrow D \rightarrow A$ in figure 5.14. If the Kelvin-Stokes theorem is applied to the velocity field, the circulation can be written as

$$\begin{aligned} \Gamma = \oint_L \vec{u} \cdot \mathrm{d}\mathbf{r} &= \int_{E'} \nabla \times \vec{u} \cdot \mathrm{d}\mathbf{s} \\ &= \int_{E'} \vec{\omega} \cdot \mathrm{d}\mathbf{s}, \end{aligned} \tag{5.24}$$

where L is the closed loop $ABCDA$ enclosing region E', and E' denotes half of the area of interest (see figure 5.14). If the bubble circulation is computed, the integral range E' is reduced to half of the bubble region. If E' is infinitely large, i.e. the three boundaries of the contour BC, CD, DA can be placed far enough from the ring and the wake, their contour integral is negligible. Thus, the closed loop integral

can be reduced to

$$\Gamma \approx \int_A^B \vec{u} \cdot \mathrm{d}\mathbf{r} = \int_0^{-\infty} v \cdot \mathrm{d}y. \tag{5.25}$$

The dimensionless circulation $\widehat{\Gamma}$ can then be calculated from equations 4.9, 4.7 and 4.14 as

$$\begin{aligned}
\Gamma = \int_0^{-\infty} v \cdot \mathrm{d}y &= \int_0^{-\infty} V \left(\frac{I}{\rho}\right)^{\frac{1}{4}} (t-t_o)^{-\frac{3}{4}} \cdot \mathrm{d}\left[\xi \left(\frac{I}{\rho}\right)^{\frac{1}{4}} (t-t_o)^{\frac{1}{4}}\right] \\
&= \int_0^{-\infty} \left(\frac{I}{\rho}\right)^{\frac{1}{2}} (t-t_o)^{-\frac{1}{2}} V \cdot \mathrm{d}\xi \\
&= \left(\frac{I}{\rho}\right)^{\frac{1}{2}} (t-t_o)^{-\frac{1}{2}} \int_0^{-\infty} V \cdot \mathrm{d}\xi \\
&= \left(\frac{I}{\rho}\right) (y-y_o)^{-2} \xi^2 \int_0^{-\infty} V \cdot \mathrm{d}\xi \\
&= \left(\frac{I}{\rho}\right) (y-y_o)^{-2} \xi^2 \widehat{\Gamma}.
\end{aligned} \tag{5.26}$$

Therefore,

$$\widehat{\Gamma} = \left(\frac{\rho}{I}\right) \frac{(y-y_o)^2}{\xi^2} \Gamma. \tag{5.27}$$

From equation 5.24, it can be easily shown that

$$\widehat{\Gamma} = \int_0^{-\infty} V \cdot \mathrm{d}\xi = \int_{\epsilon'} \widehat{\omega} \cdot \mathrm{d}\xi \mathrm{d}\eta, \tag{5.28}$$

where ϵ' denotes half of the area of interest ϵ in similarity coordinates; $\widehat{\omega}$ is the dimensionless vorticity which will be defined in equation 5.31.

The plot of the circulation is presented in figure 5.15, which has been scaled according to the similarity scaling law (equation 5.27). The circulation is computed from the ensemble-averaged vorticity contours. Equation 5.10 shows that the averaged circulation is independent of the order of the averaging processes. The theory underestimates the decay of the bubble circulation by a very small factor up to the extent of the FOV. It is not very clear in the Re_1 rings, but downstream there is a small deviation. While the circulation of the bubble decays roughly in line with the similarity theory the circulation of the entire field decays much more rapidly. This then may be predominantly due to annihilation of vorticity in the wake. Although

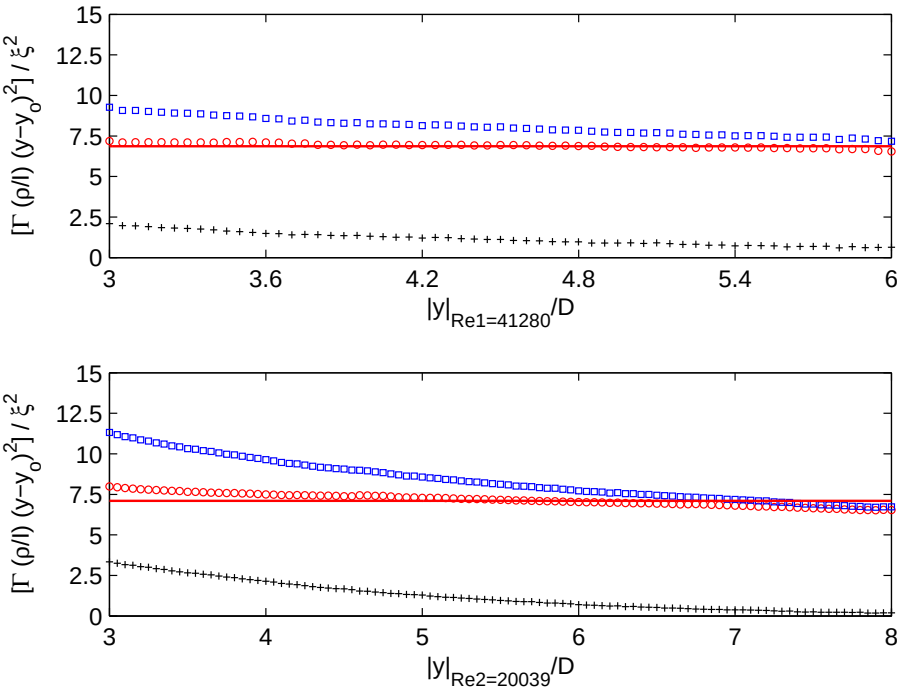

Figure 5.15: Circulation as a function of streamwise distance computed from $\Gamma_{B'} = \int_{B'} \omega_\theta \mathrm{d}x\mathrm{d}y$, based on the ensemble-averaged vorticity contours for both Re rings. □: the whole flow field, where B' represents left/right half of the entire flow fields; ○: the ring bubble area, where B' represents the rectangular region of $1.4D$ in the streamwise direction and $1.2D$ in the radial direction aside on the ring's mean trajectory; +: the wake part, equal to the difference between □ and ○. The circulations of the ring bubble area are scaled according to the similarity law (equation 5.27), in which the two − are the zero-order least-squares fits for $|y|/D \geqslant 3.5$ with y_o obtained from figure 5.1.

vorticity leaving the PIV measurement plane due to three-dimensional effects may also be responsible, since there is a weak anisotropy in the wake, this effect is not believed to be as important as the annihilation effect. Further downstream, the amount of vorticity obtained from shedding from the ring bubble is not enough to compensate for that being continuously annihilated in the wake. The vorticity shedding process only involves the lowest level around the ring cores, therefore the effect is less significant. This is discussed next.

5.1.8 Instantaneous vorticity shedding pattern

The continuous falling pattern of the ring bubble circulation (the amount of the single-signed vorticity) shown in figure 5.15 is the ensemble-averaged behaviour. In this section, the vorticity shedding pattern of an individual ring is investigated. Because the ring is highly turbulent, the viscous effect is insignificant compared with the inviscid effect, thus it is believed that the inviscid vorticity shedding is the major cause of the circulation reduction while the viscous annihilation effect is rather weak, if not insignificant at all, although ultimately viscosity kills all the circulation. Figure 5.16 shows snapshots at six streamwise distances of a typical $Re = 20039$ ring, which illustrate the vorticity contours around its left core.

The computational algorithm is designed such that the connected contour of a specified level enclosing the core centroid is traced. Closed contours of the same level but not enclosing the core are not included for circulation computation. This algorithm is designed specially for tracking the inviscidly shed vorticity, which will show abrupt changes in the circulation plot, while if annihilation is the only mechanism, the change would be smooth. The robustness of the algorithm is clearly shown by figure 5.16 (b), in which a closed contour of the same level to the 'south-east' of the core is not marked by the black line, or by the sudden drop of circulation between (a) and (b) on the red trace and between (d) and (e) on the blue trace.

Figure 5.16 (a), (b), (c) show that inviscid shedding of vorticity blobs is only associated with the lower vorticity levels and the shedding process is accompanied by a reattachment or reconnection process. This can be observed in (c), an increase of the red trace circulation is due to some part of the blob in the south-east corner of (b) being entrained into the core. For the next higher vorticity levels (inner contours),

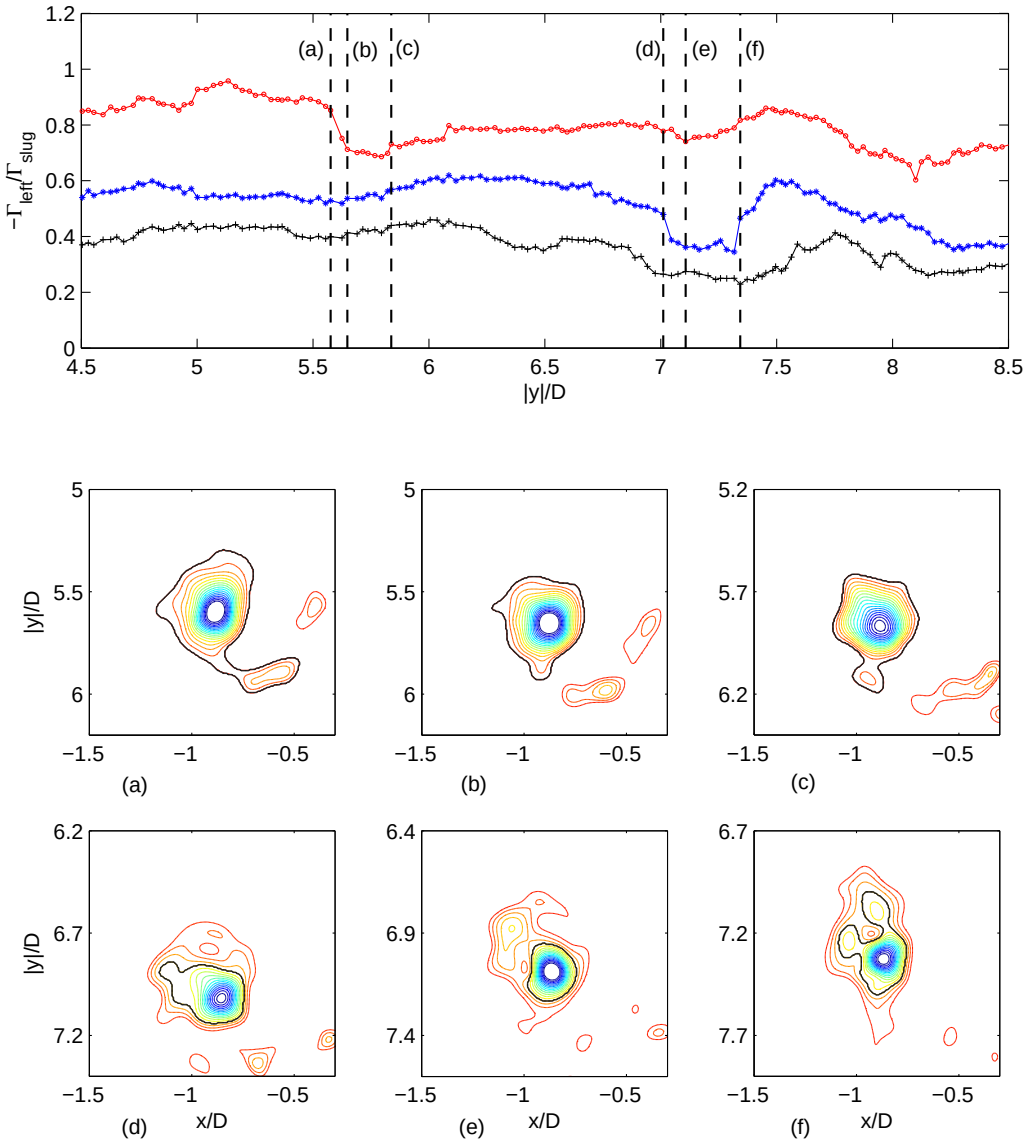

Figure 5.16: The vorticity shedding pattern of an instantaneous $Re = 20039$ ring. Only the circulation and the vorticity contours of the left core are shown. $-\circ-$, $-*-$ and $-+-$ denote the circulations enclosed by the vorticity level $\omega_\theta = -15s^{-1}$ (about 14% of the peak vorticity level), $-30s^{-1}$ and $-45s^{-1}$ respectively. Contour levels in (a)-(f): -95.0(5.0)-15.0, higher and lower levels not shown. (a), (b), (c) correspond to the $-\circ-$ data, $-$ indicates the connected $\omega_\theta = -15s^{-1}$ contour; (d), (e), (f) correspond to the $-*-$ data, $-$ indicates the connected $\omega_\theta = -30s^{-1}$ contour.

the 'diffusion' of higher vorticity to lower levels is also by inviscid shedding, as shown by (d) and (e). The reattachment is even clearer in this level, shown by (e) and (f), and by the abrupt increase of circulation of the blue trace, just before (f). The circulation plot of $\omega_\theta = -45s^{-1}$ contour does not show any noticeable abrupt change, which suggests that the viscous effect has the major responsibility in the inner most core regions. It is worth mentioning that Weigand & Gharib (1994) observed a step-like shedding of vorticity of a $Re = 7500$ ring with a long term behaviour, which is also supported by the numerical results in Bergdorf *et al.* (2007). The 'step' is believed to be due to the same shedding pattern shown here in figure 5.16. However, in this study, it is more sawtooth-like due to reattachment events. The discrepancy is probably because of the fact that it is not the long-term behaviour being focused in this study, the ring may not have decayed enough and the stepwise shedding has not started yet.

Because the bubble circulation decay of an instantaneous turbulent vortex ring in this study is predominantly an unsteady effect, strictly speaking, the similarity theory can only give a long-term general prediction of it, but not a local instantaneous description.

5.1.9 Hydrodynamic impulse

The hydrodynamic-impulse invariance is an important assumption in deriving the similarity theory. This quantity is discussed here with the experimental evidence. The hydrodynamic impulse of a vortex ring is calculated from equation 4.3. In the case of an axisymmetrical flow, the impulse vector is along the streamwise direction and can be derived from equation 4.3:

$$\begin{aligned} I_y &= \frac{1}{2}\rho \int_V (r\omega_\theta)\, \mathrm{d}V \\ &= \frac{1}{2}\rho \int_0^\infty r\omega_\theta \cdot 2\pi r\, \mathrm{d}r \int_{-\infty}^0 \mathrm{d}y \\ &= \pi\rho \int_0^\infty \int_{-\infty}^0 \omega_\theta r^2\, \mathrm{d}y\mathrm{d}r \\ &= \pi\rho \int_{E'} \omega_\theta r^2\, \mathrm{d}\mathbf{s}, \end{aligned} \tag{5.29}$$

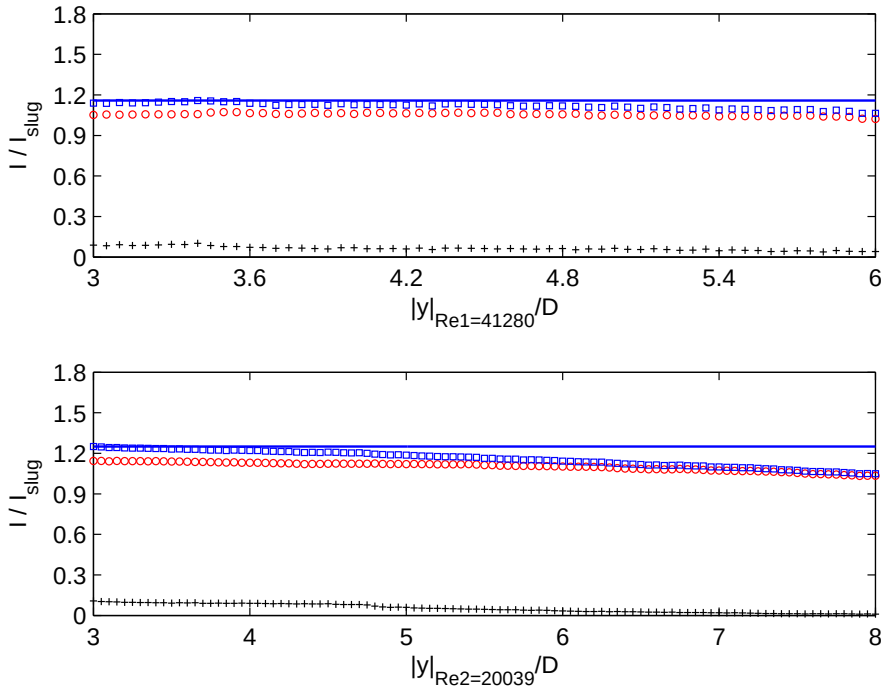

Figure 5.17: Hydrodynamic impulse as a function of streamwise distance computed from equation 4.3, based on the ensemble-averaged vorticity contours for both Re rings. The quantity is normalised by slug impulse. □: the whole flow field; ○: half of the ring bubble area, which is simplified as a rectangular region of $1.4D$ in the streamwise direction and $1.2D$ in the radial direction aside on the ring's mean trajectory; +: the wake part, equal to the difference between □ and ○; −: the maximum impulse level of the whole flow field.

where y, r and θ denote the streamwise, radial and azimuthal directions; E' refers to half of the FOV shown in figure 5.14. The integral range can be altered for computing full field (E') and bubble impulses (B') respectively, as those used for computing circulation.

The variation of the hydrodynamic impulse as a function of streamwise distance is presented in figure 5.17, in an attempt to show how the decay of the circulation is related to the behaviour of the impulse. A small decay is observed in the bubble impulse which agrees with Maxworthy (1974), as well as the full-field impulse, although it is much less severe than the decay of the full-field circulation. The amount

of decay of the full-field impulse up to the last points in figure 5.17 is about 8% and 16% for Re_1 and Re_2 rings, respectively and the decay of the bubble impulse is about 5% and 10%, respectively (note the different end points for the two cases). On one hand, the increase of the ring radius (see figure 5.1) leads to an increase in impulse (see equation 4.3, 5.29); on the other hand, the vortical structures shed from the bubble are less intense, and hence result in only a small loss of ring impulse. The slug model underestimates both impulse and circulation (Didden, 1979; Lim & Nickels, 1995; Shariff & Leonard, 1992), for reasons given in section 2.1. It is noteworthy that the impulse involved in the similarity theory is the hydrodynamic impulse, which is computed from equation 4.3. Saffman (1976) derived the impulse required to set a region of fluid into unsteady vortical motion that includes an extra term, which is not always easy to measure empirically. This impulse is written as

$$\boldsymbol{I} = \frac{1}{2}\rho \int_V (\vec{r} \times \vec{\omega})\ \mathrm{d}V + \rho \int_s \phi \boldsymbol{n}\, \mathrm{d}\boldsymbol{S}, \tag{5.30}$$

where $\boldsymbol{n}$ is the unit normal vector of the surface $\boldsymbol{S}$, directed into the region of compact vorticity; ϕ is the velocity potential at the surface $\boldsymbol{S}$ of the body. Physically, the second term is associated with the momentum of vortex ring added-mass (non-entrained fluid of non-zero velocity surrounding the ring bubble, as mentioned in the end of section 2.4). Notwithstanding the dominance of the first term in many circumstances - hence it is often used by itself for force estimation - the second term can be substantial sometimes (Krueger & Gharib, 2003).

5.1.10 Virtual time origins

Finally, the virtual time origins of both Reynolds number cases can be determined by plotting the ring locations against arrival times (equation 4.15), as is shown in figure 5.18. The two virtual time origins are $T = -2.61sec$ and $T = -5.28sec$ for Re_1 and Re_2 rings, respectively.

5.2 The raw turbulence quantities

Section 5.2.1 presents the two-dimensional contours of the ensemble-averaged vortex ring structures: the velocity components and vorticity contours. Section 5.2.2 and

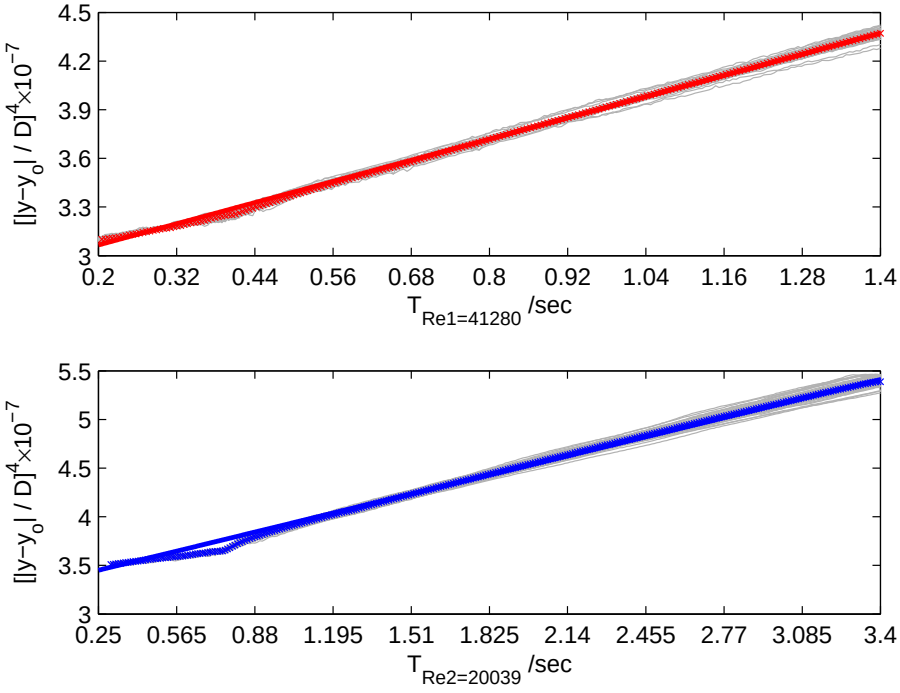

Figure 5.18: Determination of the virtual time origins by intersecting the line to the time axis. Grey lines are the traces of each of the 50 realisations.

5.2.3 present the intensity distribution of the turbulent stresses and production in the ring centre cross-section. Section 5.2.4 presents the results of the pressure gradient distribution in the centre cross-section, and hence pressure distribution. All of these contour plots are shown in the similarity coordinates, and the Reynolds number independence is also verified.

5.2.1 The mean structure

If the similarity theory is considered to work well in this experiments, at least over some distance, the velocity components can be scaled accordingly to equation 4.9. In order to verify the validity of the scaling law, testing ranges are set for the ring-bubble centre position from $-4D$ to $-6D$ for the Re_1 rings and $-5.5D$ to $-7.5D$ for the Re_2 rings, in the streamwise direction, such that rings are located as far downstream as possible while the whole ring structure can still be seen. Velocity components at each station within the testing ranges are then scaled according to equation 4.9. Figure 5.19 shows that the scaling law works well and curves of both Reynolds numbers tend to collapse, indicating that Reynolds number is not a strong factor influencing the mean velocity, although the higher Reynolds number rings have a slightly more 'peaked' core. Mean velocity and vorticity contours are presented from figure 5.20 to figure 5.22 by taking equation 4.7 for scaling the coordinates and 4.9 for scaling the velocities. The dimensionless vorticity can be easily derived as

$$\begin{aligned}
\widehat{\omega_\theta} &= \frac{\partial V}{\partial \eta} - \frac{\partial U}{\partial \xi} \\
&= \frac{(\rho/I)^{\frac{1}{4}} (t-t_o)^{\frac{3}{4}} \partial v}{(\rho/I)^{\frac{1}{4}} (t-t_o)^{-\frac{1}{4}} \partial x} - \frac{(\rho/I)^{\frac{1}{4}} (t-t_o)^{\frac{3}{4}} \partial u}{(\rho/I)^{\frac{1}{4}} (t-t_o)^{-\frac{1}{4}} \partial y} \\
&= (t-t_o) \left(\frac{\partial v}{\partial x} - \frac{\partial u}{\partial y} \right) \\
&= (t-t_o)\, \omega_\theta. \qquad (5.31)
\end{aligned}$$

It is worth noticing that, even though figure 5.3 indicates that the similarity theory does not work perfectly for the entire data range presented, for the range tested here, the theory works well. The time scale involved in equation 4.9 is set to be the averaged arrival time of the 50 rings at the station being tested. The largest

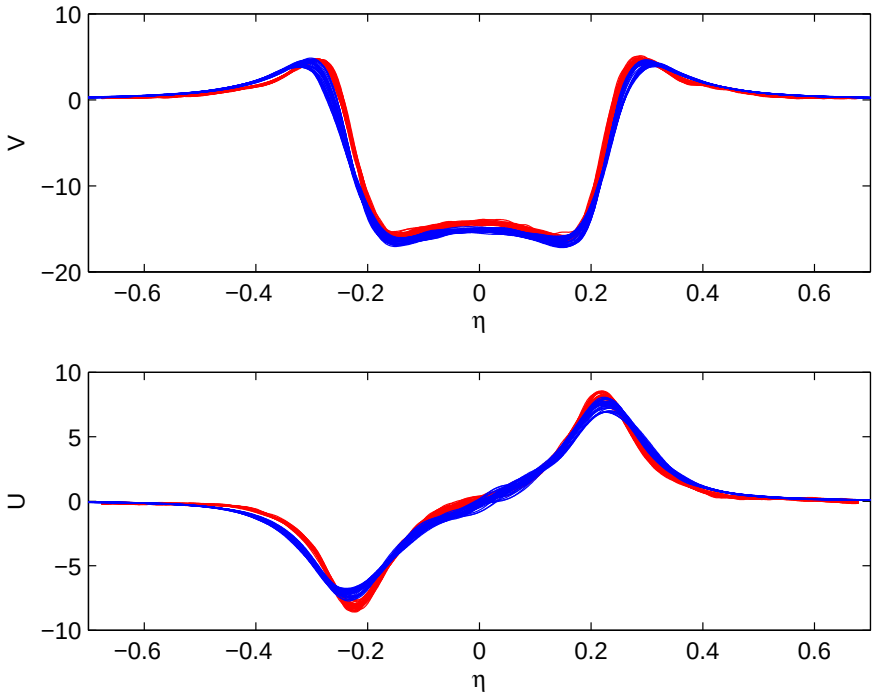

Figure 5.19: Velocity components at all the testing stations scaled by similarity theory for two Reynolds number cases. The axial component is chosen to cut the two core centres (at each station locations); the radial component is chosen to be $0.1D$ below the core centre, simply because this quantity vanishes across the centres. – traces: $Re_1 = 41280$; – traces: $Re_2 = 20039$.

arrival time difference at a station is typically below $\pm 0.06sec$ for Re_1 rings and $\pm 0.15sec$ for Re_2 rings, which are negligible compared to the virtual time origins t_o.

It must be clarified that when the real coordinates x and y are scaled to similarity ones ξ and η, in equation 4.7, the grid spacings $\Delta\xi$ and $\Delta\eta$ are slightly different for different times. The time duration of the testing range for the two Reynolds numbers are typically $0.35sec$ and $0.71sec$, respectively, which can be deduced from figure 5.10 or 5.5 or 5.18. This gives grid spacing differences of about $\pm 1\%$ (see equation 4.7). The non-uniform spacing grids (between times) could be interpolated to give uniform ones, but this would significantly increase algorithm difficulties and computational expense. Because the differences are typically about 1%, interpolation is not applied, and the grid spacings used in all the similarity contours shown below are computed

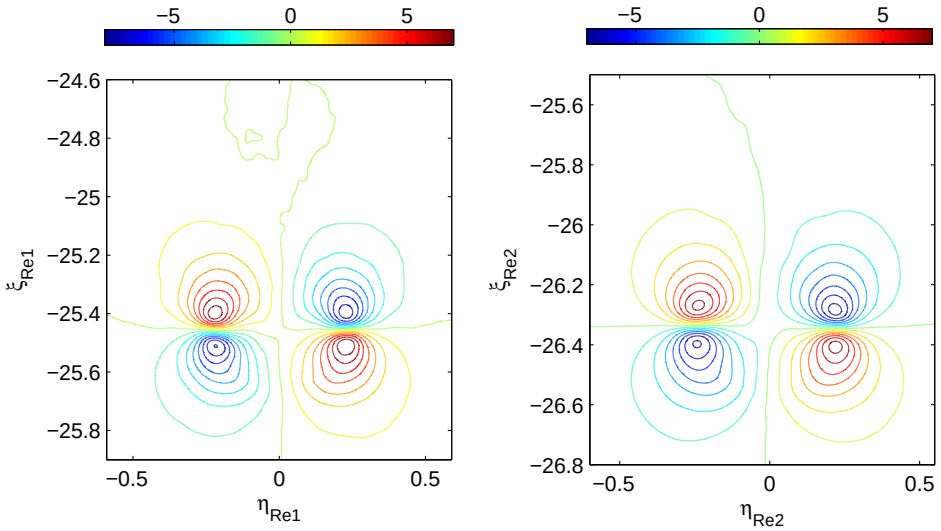

Figure 5.20: Radial velocity U contours in similarity coordinates.

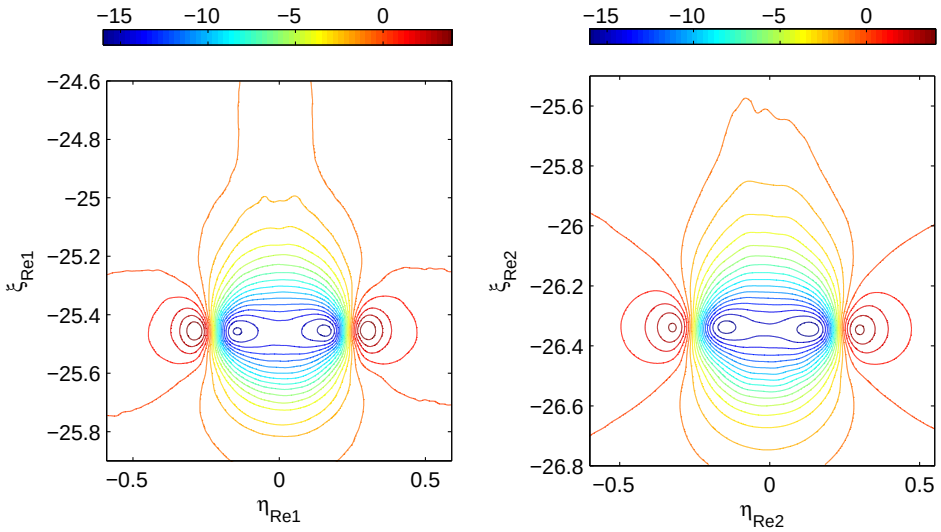

Figure 5.21: Axial velocity V contours in similarity coordinates.

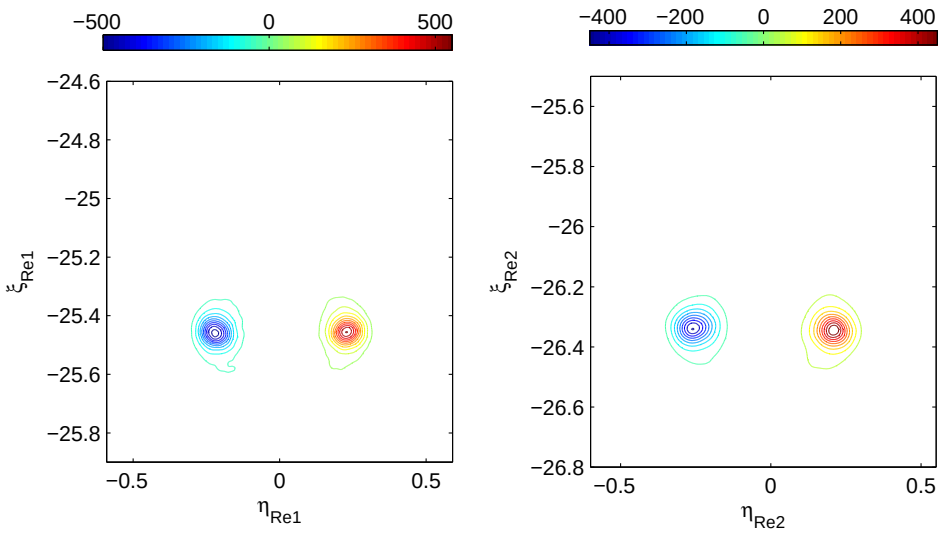

Figure 5.22: Vorticity $\partial V/\partial\eta - \partial U/\partial\xi$ contours in similarity coordinates, obtained from the velocity contours.

from the averaged arrival times in the testing range, when applying equation 4.7.

When quantities are presented in similarity coordinates, essentially they have gone through a double averaging process. The first involves averaging the 50 realisations at each of the stations described in figure 5.2, to give an averaged contour. There are 41 stations in the testing range ($2D$ for both Reynolds numbers) because the station spacing is $0.05D$. The similarity scaling law, equation 4.9 and 4.7 (effectively a Taylor's hypothesis reconstruction, Taylor, 1938) indicates a second averaging of these 41 stations. Therefore each contour here is the average of 2050 instantaneous realisations, although they are not all independent.

5.2.2 The turbulence stresses

In order to better understand the turbulence structure, it is necessary to examine the turbulence stresses and production. Since the mean structure appears to follow similarity well, turbulence quantities (stresses and production, Davidson, 2004; Tennekes & Lumley, 1972) here are scaled using the similarity transformations and they are presented in similarity coordinates in figures 5.23 to 5.25 and figure 5.29, for rings of both Reynolds numbers. The relationships between the dimensional quantities

and the similarity quantities can be deduced from equation 4.9. Particularly,

$$\begin{aligned} -\overline{U'U'} &= -\overline{u'u'}\left(\frac{\rho}{I}\right)^{\frac{1}{2}}(t-t_o)^{\frac{3}{2}} \\ -\overline{V'V'} &= -\overline{v'v'}\left(\frac{\rho}{I}\right)^{\frac{1}{2}}(t-t_o)^{\frac{3}{2}} \\ -\overline{U'V'} &= -\overline{u'v'}\left(\frac{\rho}{I}\right)^{\frac{1}{2}}(t-t_o)^{\frac{3}{2}}, \end{aligned} \tag{5.32}$$

where the superscript prime, here-and-after denotes the velocity fluctuation.

Peak turbulence quantities can be clearly identified and are found to be located very close to the mean vortex cores. When comparing these structures with the LDV results[1], perhaps the most distinguishable difference is the degree of asymmetry, which is partly because of the different experimental approaches. Note that the LDV results are perfectly symmetrical since they were measured at only one side and reflected for presentation in the contour plots; see figure D.1, D.2 and D.3. This small asymmetry also exposes the most important contributor of the turbulence quantities, dispersion, the reasons for which have been discussed in section 5.1.1. The second obvious difference, is the existence of secondary cores beside the main cores shown in the LDV results, which seems only be possible when rings are located exactly at the same location and are of the same size and shape. This difference will be further discussed in chapter 6.

Because the core centroids have a random scatter in the centroid cluster plot; see figure 5.26, small details near the core centre (if they exist) will be smoothed away by the averaging process. In order to examine how dispersion affects the stress level and distribution, the core dispersion level is plotted in figure 5.27. The core dispersion is quantified by the r.m.s. value γ, which is defined as

$$\gamma = \sqrt{\frac{1}{N}\Sigma_N\left[(x_c-\overline{x_c})^2+(y_c-\overline{y_c})^2\right]}, \tag{5.33}$$

where $N = 50$ (realisations), $\overline{x_c}$ and $\overline{y_c}$ are the ensemble-averaged core location coordinates, x_c and y_c are instantaneous core location coordinates of a single realisation. In figure 5.27, γ is normalised by the mean core centroid streamwise location.

Note that the effect of dispersion is to add to the turbulence intensities, since it adds an extra effective fluctuation. Figure 5.27 is able to explain several facts: first,

[1]From here onwards, LDV results refer to the results presented in Glezer & Coles (1990).

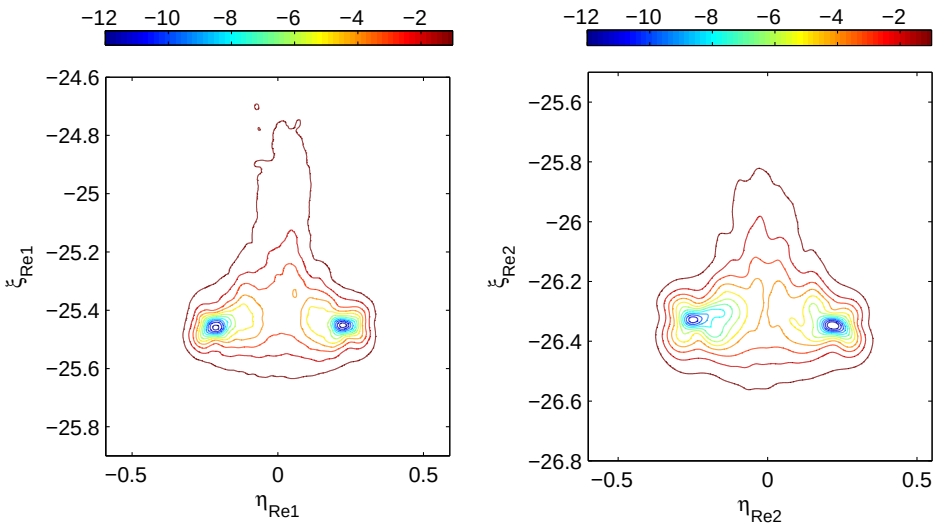

Figure 5.23: Contours of radial normal Reynolds stresses $-\overline{U'U'}$ in similarity coordinates. Higher levels in the core centre area are not shown.

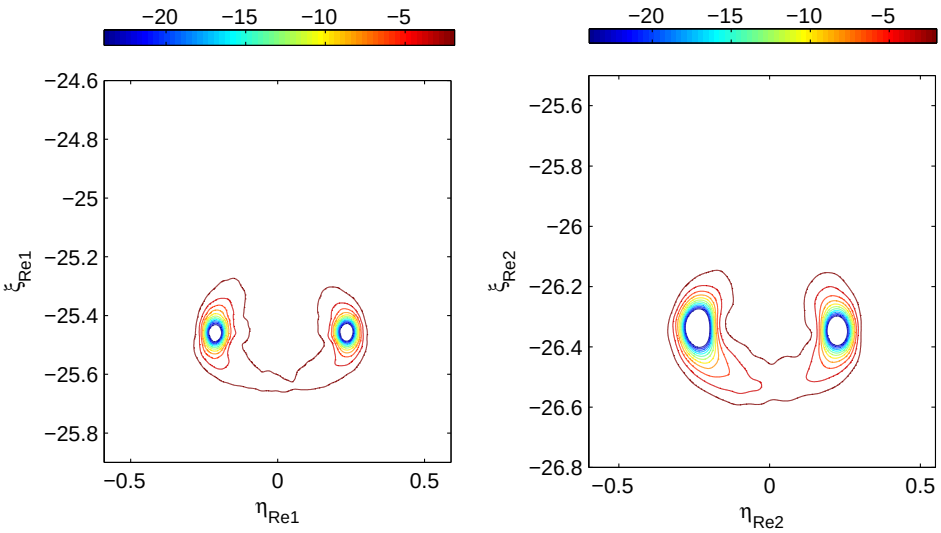

Figure 5.24: Contours of axial normal Reynolds stresses $-\overline{V'V'}$ in similarity coordinates. Higher levels in the core centre area are not shown.

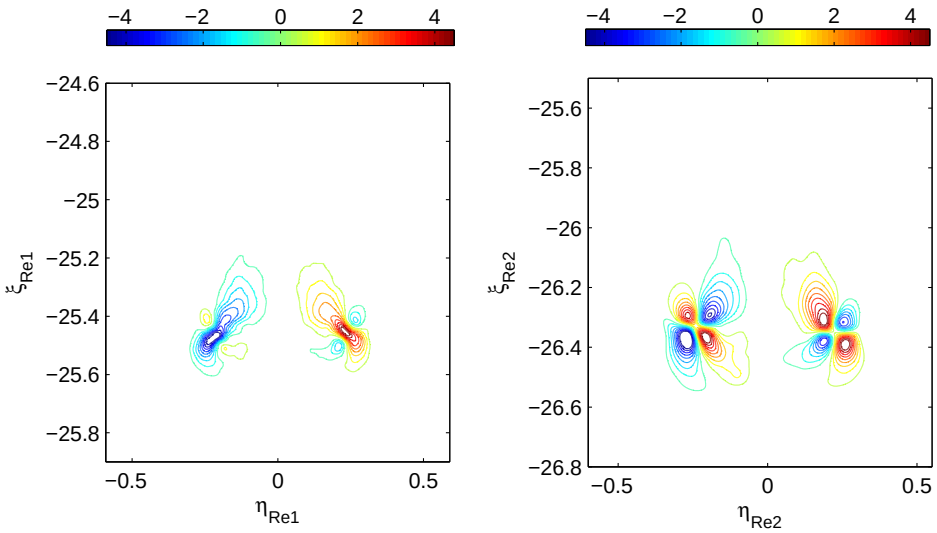

Figure 5.25: Contours of Reynolds shear stresses $-\overline{U'V'}$ in similarity coordinates. Higher levels in the core centre area are not shown.

the Re_1 rings have a more symmetrical dispersion, therefore stresses and production contours are more symmetrical; second, the left core dispersion is more severe in the Re_2 plot, which causes the intensities of the left core to exceed that of the right core in figure 5.24; third, dispersion increases as the ring moves downstream, which may be the reason why the turbulence intensity level does not decay (shown in figure 5.28), while the similarity theory predicts that, the stress level at every point will decrease as $t^{-3/2}$ or y^{-6}, hence the level of the stress integrated over the bubble area will decrease as t^{-1} or y^{-4}. The radial component of the Reynolds stress is used to illustrate this relationship. From equation 4.9, 4.7 and 4.14,

$$\begin{aligned}
\int_B -\overline{u'u'}\,\mathrm{d}r\mathrm{d}y &= \int_S -\overline{U'U'}\left(\frac{I}{\rho}\right)^{\frac{1}{2}}(t-t_o)^{-\frac{3}{2}}\left[\left(\frac{I}{\rho}\right)^{\frac{1}{2}}(t-t_o)^{\frac{1}{2}}\right]\mathrm{d}\xi\mathrm{d}\eta \\
&= \left(\frac{I}{\rho}\right)(t-t_o)^{-1}\int_S -\overline{U'U'}\,\mathrm{d}\xi\mathrm{d}\eta \\
&= \xi^4\left(\frac{I}{\rho}\right)^2(y-y_o)^{-4}\int_S -\overline{U'U'}\,\mathrm{d}\xi\mathrm{d}\eta, \qquad (5.34)
\end{aligned}$$

where B and S denote the centre cross-sectional area of the ring bubble volume in

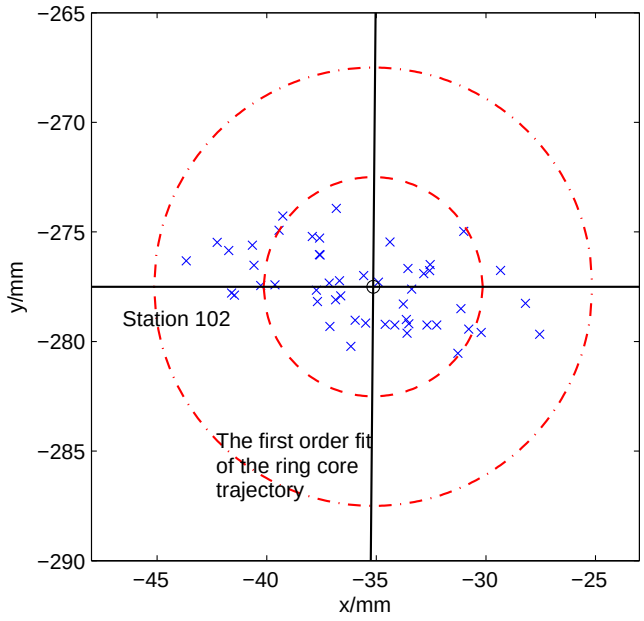

Figure 5.26: The left-hand-side core centroid footprints cluster at station 102 (see figure 5.2) for 50 the realisations of $Re = 41280$ rings. $\times$ denotes each of the core centroids; $\circ$: the intersection point of the station 102 line and the first-order fit of the ring core trajectory; $--$ denotes a $5mm$ radius circle centred at $\circ$; $-\cdot-$ denotes a $10mm$ radius circle centred at $\circ$.

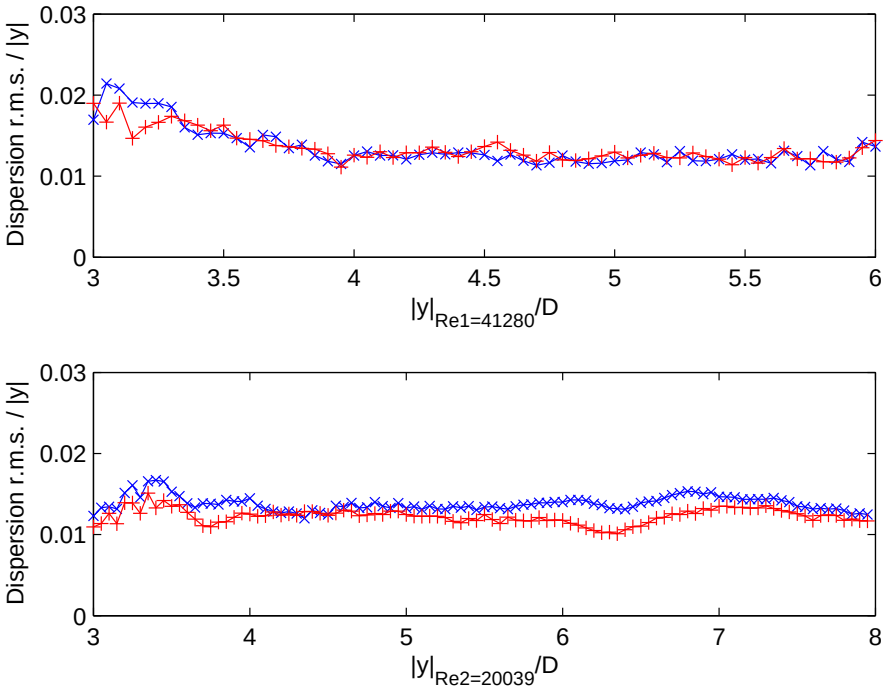

Figure 5.27: The r.m.s. of the apparent core centroids dispersion with respect to the mean core centroid streamwise location, equation 5.33. This quantity is normalised by the rings' streamwise location. Therefore a horizontal line indicates an increasing dispersion level. $\times$: left core; $+$: right core.

real and similarity coordinates, respectively. Because

$$\xi^4 \left(\frac{I}{\rho}\right)^2 \int_S -\overline{U'U'}\,\mathrm{d}\xi\mathrm{d}\eta = const., \tag{5.35}$$

then

$$\int_B -\overline{u'u'}\,\mathrm{d}r\mathrm{d}y \sim t^{-1} \sim (y - y_o)^{-4} \tag{5.36}$$

and

$$\int_S -\overline{U'U'}\,\mathrm{d}\xi\mathrm{d}\eta = \xi^{-4} \left(\frac{\rho}{I}\right)^2 (y - y_o)^4 \int_B -\overline{u'u'}\,\mathrm{d}r\mathrm{d}y. \tag{5.37}$$

The same procedure can also be applied to the other two stresses. It must be emphasised here that the integral of stresses over a planar bubble area is used to reveal the stresses dependence on time and downstream distance. If the assumption of axisymmetry is adopted, it is always possible to estimate the stress levels in a three-dimensional bubble volume. This however, is not done, because it will not give more information, since it would be inferred from the two-dimensional results.

Despite the differences, general agreement with the broad features noted in the LDV results is apparent, for instance, a wake can only be observed in the radial component of the normal stresses, not in the axial component; see figure D.1 and D.2.

In figure 5.28, the summation of the magnitude of the Reynolds stress over the ring bubble area as a function of ring streamwise location is plotted. The magnitudes of the total stress in the bubble region can be written as

$$\int_B |\tau|\,\mathrm{d}\boldsymbol{B} = \int_B |\tau|\,\mathrm{d}r\mathrm{d}y, \tag{5.38}$$

where $\tau = -\overline{u'u'}, -\overline{v'v'}$, or $-\overline{u'v'}$. In order to exclude the effect of the wake, the three stress levels are only computed in the ring bubble area. For simplicity, the bubble area is chosen to be a rectangular region of $1.4D$ in streamwise direction and $2.4D$ in radial direction, which is big enough to include the bubble but small enough to exclude the wake (see figure 5.11). For bubble circulation and impulse computation, only half of this rectangular region is needed, i.e. $1.4D$ in streamwise direction and $1.2D$ in radial direction, as mentioned in the captions of figure 5.15 and 5.17. Note that $5.55D$ is closed to the end of the FOV, which is $6D$, and the bubble volume increases from the orifice exit to $6D$ (see figure 5.12). Therefore the

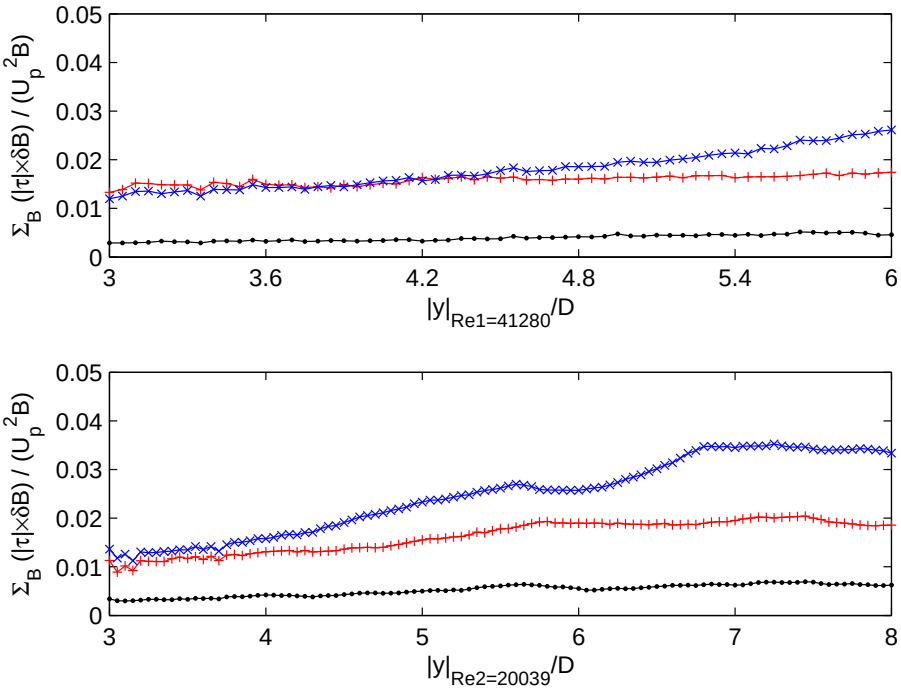

Figure 5.28: The summation of the magnitude of the Reynolds stress over the ring bubble area $\int_B |\tau| \, \mathrm{d}\boldsymbol{B}/U_p^2 B$ as a function of ring streamwise location. τ: $-\overline{u'u'}$, $-\overline{v'v'}$ or $-\overline{u'v'}$; B: the rectangular region of $1.4D$ in streamwise direction and $2.4D$ in radial direction; see figure 5.11. +: axial normal Reynolds stress; ×: radial normal Reynolds stress; •: Reynolds shear stress.

rectangular region can cover all the elliptical bubbles in the testing range. This integrand (over the rectangular area) is approximately equal to the integrand over the elliptical bubble area, because the stress levels outside the elliptical bubble area are insignificant. This rectangular-region is used for both cases and in all similar calculations below. Referring to figure 5.12, one finds that the bubble volume of the two Re rings only differs by less than 10%.

5.2.3 The turbulence production

The turbulence production is thought to be mainly due to the large scales, hence it can be estimated (whereas it is believed that the spatial resolution is not sufficient

to calculate the dissipation in these measurements - see section 3.3 - so this will not be attempted). In two-dimensional Cartesian coordinates, turbulence production can be written as

$$p = -\overline{u_i^{'} u_j^{'}} e_{ij} = -\sum_{i=1}^{3}\sum_{j=1}^{3}\left(\frac{1}{2}\overline{u_i^{'} u_j^{'}}\frac{\partial \overline{u_i}}{\partial x_j} + \frac{1}{2}\overline{u_i^{'} u_j^{'}}\frac{\partial \overline{u_j}}{\partial x_i}\right), \tag{5.39}$$

where $\overline{u_i}$, $\overline{u_j}$ are mean velocities and $u_i^{'}$, $u_j^{'}$ are velocity fluctuations; e_{ij} is the strain-rate tensor for the mean velocities. The subscripts of the above equation can only go up to two because of the lack of information of the third component using two-dimensional PIV analysis. The mathematical relationship between the raw turbulence production and its dimensionless form can be deduced in a similar way as equation 5.32. Take term $-\overline{u'u'}\partial\overline{u}/\partial x$ as an example. Because $\partial\overline{u}/\partial x$ has the same dimension as vorticity, from equation 5.31 and 5.32,

$$\begin{aligned} -\overline{U'U'}\frac{\partial \overline{U}}{\partial \eta} &= \left(\frac{\rho}{I}\right)^{\frac{1}{2}}(t-t_o)^{\frac{3}{2}}\left(-\overline{u'u'}\right)(t-t_o)\frac{\partial \overline{u}}{\partial x} \\ &= \left(\frac{\rho}{I}\right)^{\frac{1}{2}}(t-t_o)^{\frac{5}{2}}\left(-\overline{u'u'}\frac{\partial \overline{u}}{\partial x}\right). \end{aligned} \tag{5.40}$$

Therefore

$$P = \left(\frac{\rho}{I}\right)^{\frac{1}{2}}(t-t_o)^{\frac{5}{2}}\,p. \tag{5.41}$$

The two-dimensional production contour is presented in similarity coordinates in figure 5.29 according to the similarity scaling law of equation 5.41. Following a similar procedure as equation 5.34,

$$\begin{aligned} \int_B p\,\mathrm{d}r\mathrm{d}y &= \int_S P\left(\frac{I}{\rho}\right)^{\frac{1}{2}}(t-t_o)^{-\frac{5}{2}}\left[\left(\frac{I}{\rho}\right)^{\frac{1}{2}}(t-t_o)^{\frac{1}{2}}\right]\mathrm{d}\xi\mathrm{d}\eta \\ &= \left(\frac{I}{\rho}\right)(t-t_o)^{-2}\int_S P\,\mathrm{d}\xi\mathrm{d}\eta \\ &= \xi^8\left(\frac{I}{\rho}\right)^3(y-y_o)^{-8}\int_S P\,\mathrm{d}\xi\mathrm{d}\eta, \end{aligned} \tag{5.42}$$

where B and S denote the centre cross-sectional area of the ring bubble volume in real and similarity coordinates. Hence

$$\int_S P\,\mathrm{d}\xi\mathrm{d}\eta = \xi^{-8}\left(\frac{\rho}{I}\right)^3(y-y_o)^8\int_B p\,\mathrm{d}r\mathrm{d}y. \tag{5.43}$$

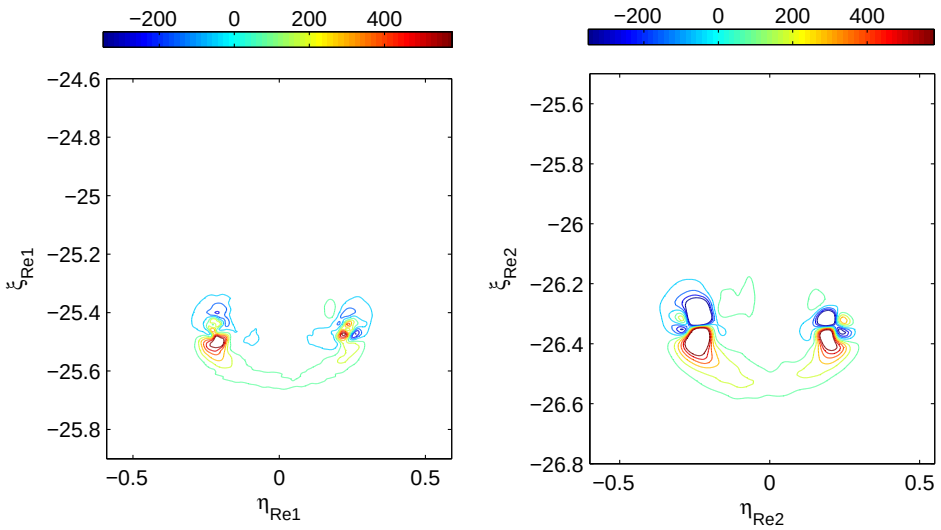

Figure 5.29: Turbulence production contours in similarity coordinates. Only the first four terms in equation 5.45 are included. Higher levels in the core centre area are not shown.

In an attempt to investigate components in the third direction, stereoscopic PIV measurements were made to provide the planar information of the out-of-plane velocity component, such that the subscripts are able to be increased to three for some terms in equation 5.39. Thus among the nine terms in the production expression, seven can be determined. The divergence free condition gives

$$\frac{\partial w}{\partial z} = 0 - \left(\frac{\partial u}{\partial x} + \frac{\partial v}{\partial y} \right), \tag{5.44}$$

leaving only $\partial u/\partial z$ and $\partial v/\partial z$ undetermined. The description of the stereoscopic PIV set-up has been given in section 3.3. Stereoscopic measurements have only been made for the $Re_1 = 41280$ case. It is believed that the effect of the involvement of the additional velocity information is similar in the $Re_2 = 20039$ case. Equation 4.9 is also used to scale the dimensional velocity into similarity forms U and V for the stereoscopic PIV results. For the out-of-plane component, the similarity velocity and coordinate are similar as U and η, which can be named W and ζ. Thus, the

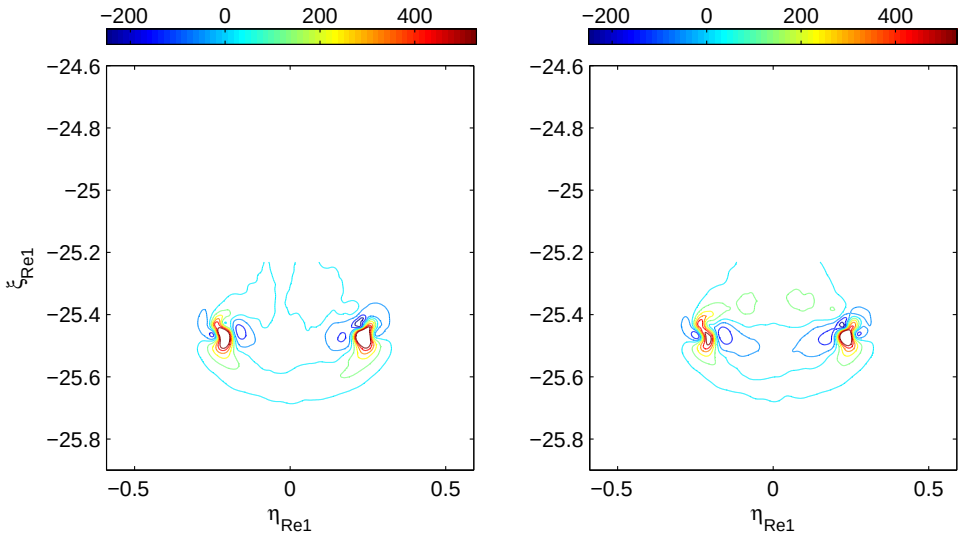

Figure 5.30: Part of the turbulence production in similarity coordinates. Higher levels in the core centre area are not shown. The figure on the right is calculated from all the seven terms in equation 5.45, the one on the left is produced using the first four terms aiming to show the effect of the third velocity component to the resultant contour. Note that the core centroid locations (ξ, η) are conserved in similarity coordinates, despite the independent experimental set-up.

similarity-scaled production P becomes

$$\begin{aligned} P \;=\; & \left(-\overline{U'U'}\frac{\partial \overline{U}}{\partial \eta}\right) + \left(-\overline{U'V'}\right)\left(\frac{\partial \overline{U}}{\partial \xi} + \frac{\partial \overline{V}}{\partial \eta}\right) + \left(-\overline{V'V'}\frac{\partial \overline{V}}{\partial \xi}\right) \\ & + \left(-\overline{W'W'}\frac{\partial \overline{W}}{\partial \zeta}\right) + \left(-\overline{U'W'}\frac{\partial \overline{W}}{\partial \eta}\right) + \left(-\overline{V'W'}\frac{\partial \overline{W}}{\partial \xi}\right). \end{aligned} \tag{5.45}$$

Figure 5.30 to figure 5.32 show that the turbulence production is predominantly reflected in the $x-y$ plane (the two-dimensional PIV measurement plane). In other words, the production is mainly contributed by the terms

$$\left(-\overline{U'U'}\frac{\partial \overline{U}}{\partial \eta}\right) + \left(-\overline{U'V'}\right)\left(\frac{\partial \overline{U}}{\partial \xi} + \frac{\partial \overline{V}}{\partial \eta}\right) + \left(-\overline{V'V'}\frac{\partial \overline{V}}{\partial \xi}\right), \tag{5.46}$$

with the contribution from the out-of-plane components

$$\left(-\overline{W'W'}\frac{\partial \overline{W}}{\partial \zeta}\right) + \left(-\overline{U'W'}\frac{\partial \overline{W}}{\partial \eta}\right) + \left(-\overline{V'W'}\frac{\partial \overline{W}}{\partial \xi}\right) \tag{5.47}$$

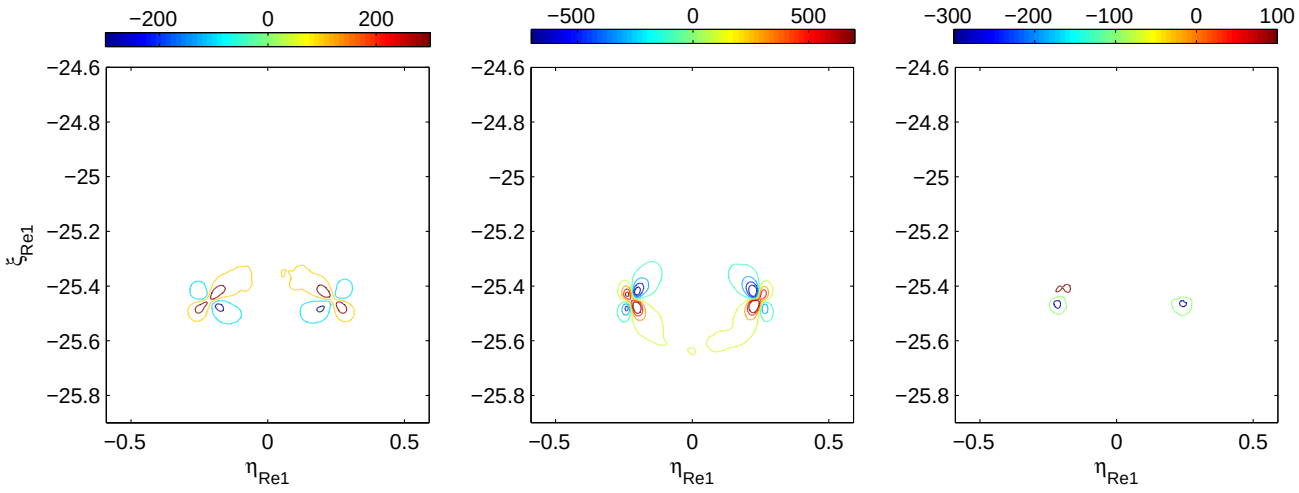

Figure 5.31: Part of the turbulence production; normal components from left to right: $-\overline{U'U'}\partial\overline{U}/\partial\eta$, $-\overline{V'V'}\partial\overline{V}/\partial\xi$, $-\overline{W'W'}\partial\overline{W}/\partial\zeta$ in similarity coordinates. Higher levels in the core centre area are not shown.

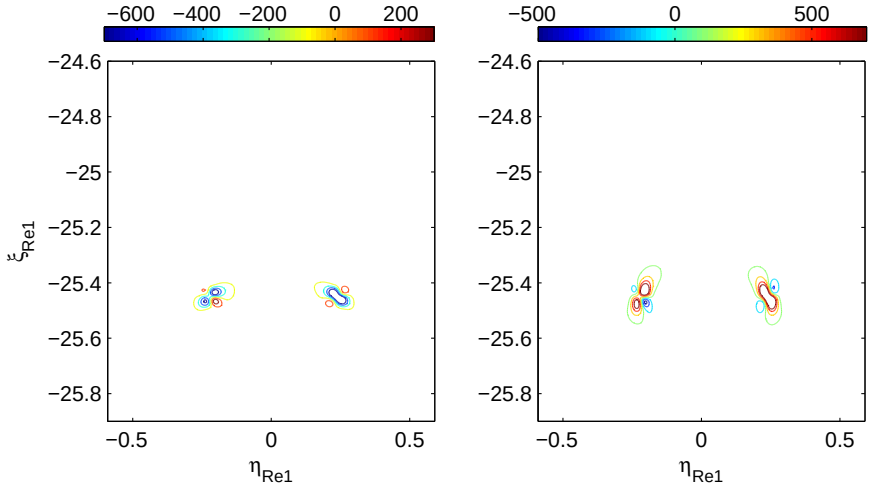

Figure 5.32: Part of the turbulence production; shear components from left to right: $-\overline{U'V'}\partial\overline{U}/\partial\xi$, $-\overline{U'V'}\partial\overline{V}/\partial\eta$, in similarity coordinates. Higher levels in the core centre area are not shown. $-\overline{V'W'}\partial\overline{W}/\partial\xi$ and $-\overline{U'W'}\partial\overline{W}/\partial\eta$ are not shown, because their intensities are too low, about 5% of the others.

generally weak except for the one which comes from the normal stress. It should be noted that in many studies, the vortex ring is assumed to be axisymmetric, hence cylindrical coordinates are frequently applied. In cylindrical coordinates, turbulence production is written as

$$p_{cyl} = \left(-\overline{u'u'}\frac{\partial \overline{u}}{\partial r}\right) + \left(-\overline{u'v'}\right)\left(\frac{\partial \overline{u}}{\partial y} + \frac{\partial \overline{v}}{\partial r}\right) + \left(-\overline{v'v'}\frac{\partial \overline{v}}{\partial y}\right) + \left(-\overline{w'w'}\right)\frac{u}{r}, \quad (5.48)$$

where y and r denote the axial and radial direction; u, v and w denote the radial, axial and azimuthal velocity components. In similarity coordinates, equation 5.48 can be written as

$$P_{cyl} = \left(-\overline{U'U'}\frac{\partial \overline{U}}{\partial \eta}\right) + \left(-\overline{U'V'}\right)\left(\frac{\partial \overline{U}}{\partial \xi} + \frac{\partial \overline{V}}{\partial \eta}\right) + \left(-\overline{V'V'}\frac{\partial \overline{V}}{\partial \xi}\right) + \left(-\overline{W'W'}\right)\frac{U}{\eta}, \quad (5.49)$$

in which only the term

$$\left(-\overline{W'W'}\right)\frac{U}{\eta} \quad (5.50)$$

accounts for the out-of-plane component.

Note that the first four terms in equation 5.45 and 5.49 are exactly the same. Thus different coordination systems applied only affect the rest of the terms. In order to investigate this effect, equation 5.47 and 5.50 are plotted and compared, in figure 5.33, from left to right. The two plots in figure 5.33 are comparable. The small difference of the intensity levels near the cores might be due to terms related to $\partial u/\partial z$ and $\partial v/\partial z$, which cannot be computed. The strong noise near the centre of equation 5.50 plot is due to the low value of η.

Reynolds stresses obtained from the stereoscopic PIV recordings are also presented in figure 5.34 and figure 5.35 as a comparison with figure 5.23 to figure 5.25. For Reynolds normal stresses, the $-\overline{W'W'}$ component is comparable with (but smaller than) $-\overline{U'U'}$, but they are about half of the $-\overline{V'V'}$. The non-negligibility of the out-of-plane component occurs for two main reasons: first, the rings are strongly three-dimensional and are possibly dispersed in a direction with a component perpendicular to the PIV plane; second, there possibly exists significant azimuthal velocities along the core region (see section 2.3), which is also reflected in the azimuthal component in figure 7.5. The main contribution to the Reynolds shear

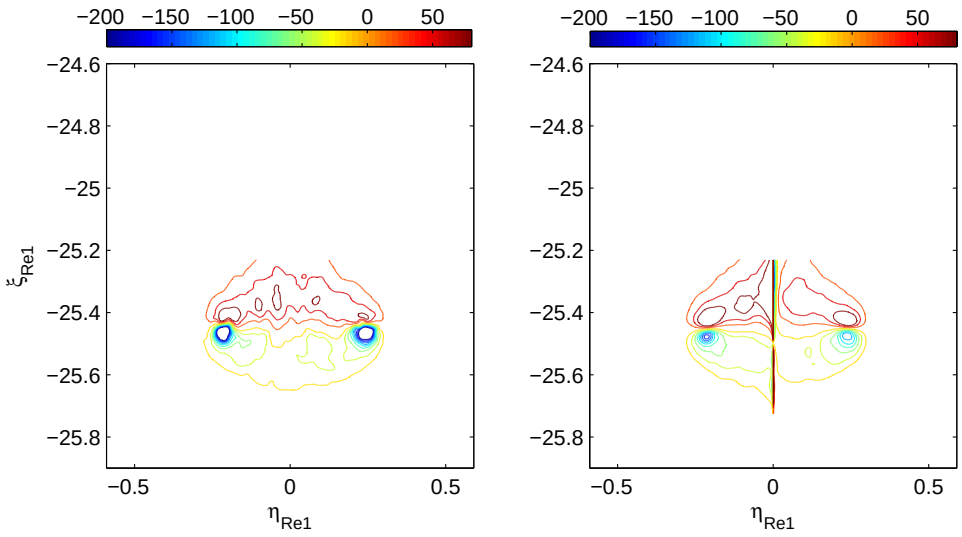

Figure 5.33: The comparison of the turbulence production in Cartesian (left) and cylindrical (right) coordinates. Equation 5.47 and 5.50 are computed and plotted, respectively.

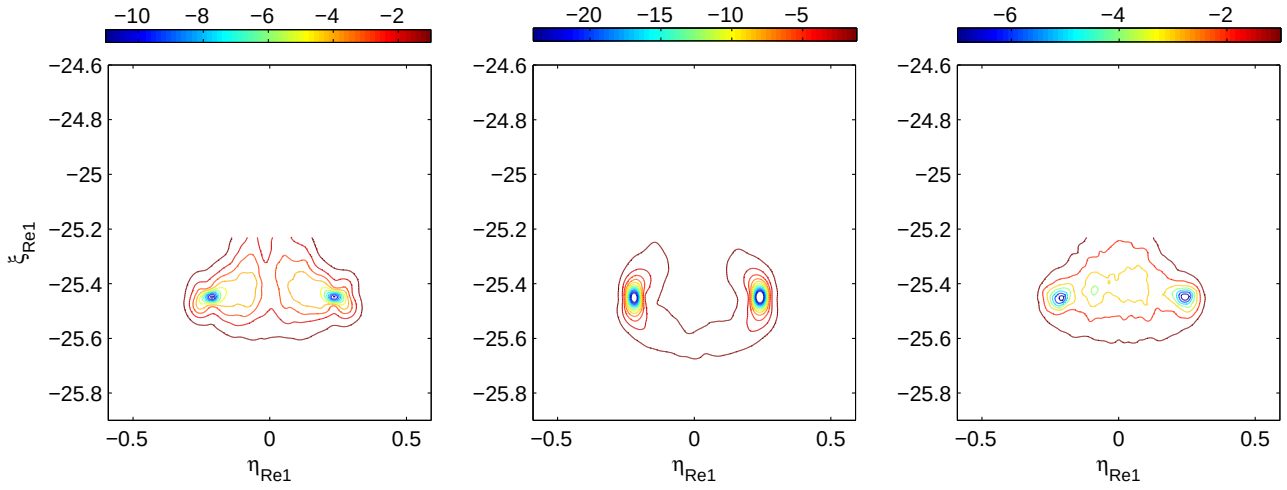

Figure 5.34: Reynolds normal stresses: $-\overline{U'U'}$, $-\overline{V'V'}$, $-\overline{W'W'}$ in similarity coordinates. Higher levels in the core centre area are not shown.

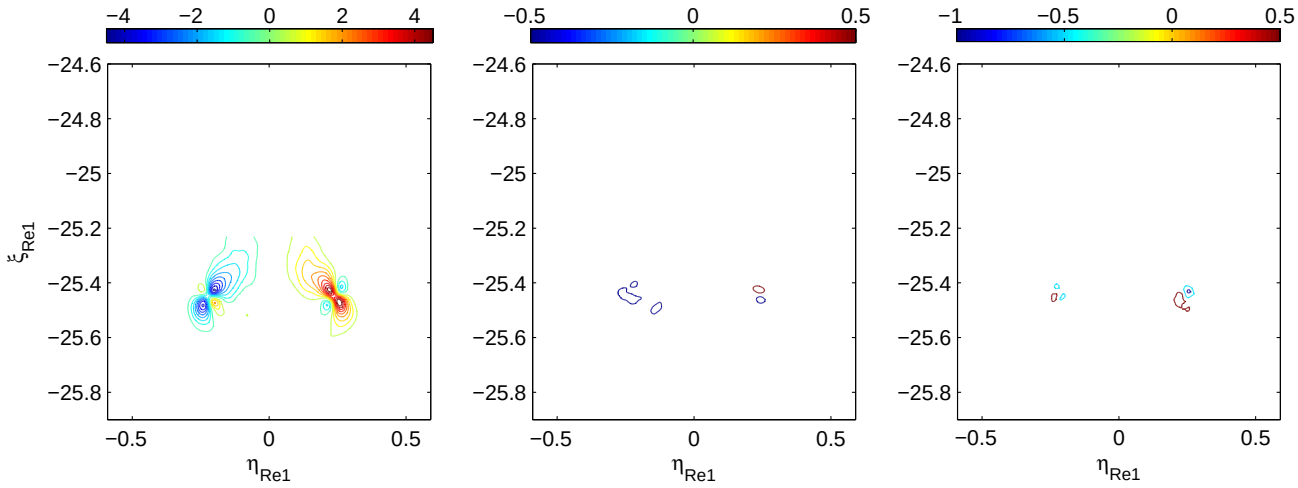

Figure 5.35: Reynolds shear stresses: $-\overline{U'V'}$, $-\overline{U'W'}$, $-\overline{V'W'}$ in similarity coordinates. Higher levels in the core centre area are not shown.

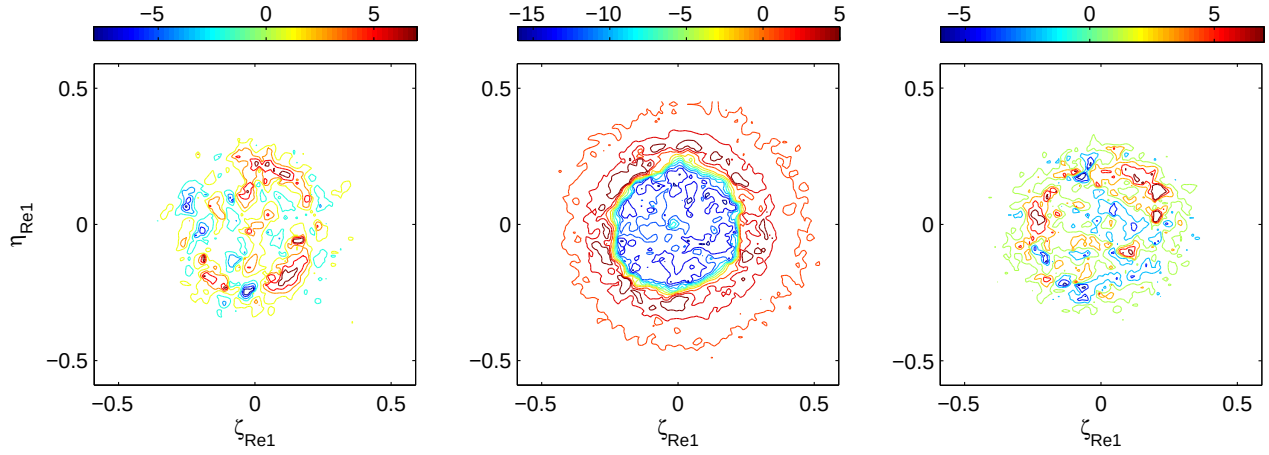

Figure 5.36: Instantaneous velocity contours in azimuthal plane presented in similarity coordinates when the PIV measurement plane approximately cuts through the ring core. From left to right: U, V, W; the symbol assignment is consistent with the two-dimensional results. Zero contour level is bypassed. The PIV plane of the two-dimensional or the first stereoscopic set-up is along η direction. Note that U, V, W are in Cartesian coordinates.

stresses is reflected by the components in the two-dimensional PIV measurement plane.

To further explore the existence and importance of the $-\overline{W'W'}$ component, the second stereoscopic set-up is adopted. The second set-up and experimental conditions are discussed in detail in section 7.1. The three instantaneous velocity components are presented in figure 5.36, in similarity coordinates. Although these are not Reynolds stresses, the strong three-dimensional structure is clearly observed and the importance of the $-\overline{W'W'}$ is expected. The importance of this quantity can also be seen in figure 7.1. The Reynolds stresses and other statistical quantities obtained from this experimental set-up will be discussed in section 7.2.

5.2.4 The pressure gradients

When the PIV measurements are operated in single-frame single-exposure mode (see section 3.3), in which time-series cross-correlation is necessary, time-dependent information can be resolved, and it becomes possible to compute the ensemble-averaged pressure gradients from the velocity information. The ensemble-averaged incompressible Navier-Stokes equation is written as

$$\overline{\frac{D\boldsymbol{u}}{Dt}} = -\frac{1}{\rho}\overline{\nabla p} + \boldsymbol{g} + \nu\overline{\nabla^2\boldsymbol{u}}, \tag{5.51}$$

or

$$\overline{\frac{\partial\boldsymbol{u}}{\partial t}} + \overline{\boldsymbol{u}\cdot\nabla\boldsymbol{u}} = -\frac{1}{\rho}\overline{\nabla p} + \boldsymbol{g} + \nu\overline{\nabla^2\boldsymbol{u}}, \tag{5.52}$$

where p in this section denotes the pressure. The continuity equation is written as

$$\nabla\cdot\boldsymbol{u} = 0. \tag{5.53}$$

The incompressible Navier-Stokes equation can be reduced to the incompressible Euler equation for turbulent vortex ring applications because at high Reynolds numbers, the inertial term dominates the viscous term. In other words, over the length scale which can be resolved in this experiment, viscous effects are not important. This point will be further commented at the end of this section. Thus equation 5.51 can be reduced to

$$\overline{\frac{D\boldsymbol{u}}{Dt}} = -\frac{1}{\rho}\overline{\nabla p} + \boldsymbol{g}. \tag{5.54}$$

Expanding the vector form into three components, equation 5.54 can be written as

$$\overline{\frac{\partial u}{\partial t}} + \overline{u\frac{\partial u}{\partial x}} + \overline{v\frac{\partial u}{\partial y}} + \overline{w\frac{\partial u}{\partial z}} = -\frac{1}{\rho}\overline{\frac{\partial p}{\partial x}} \tag{5.55}$$

$$\overline{\frac{\partial v}{\partial t}} + \overline{u\frac{\partial v}{\partial x}} + \overline{v\frac{\partial v}{\partial y}} + \overline{w\frac{\partial v}{\partial z}} = -\frac{1}{\rho}\overline{\frac{\partial p}{\partial y}} + g_y \tag{5.56}$$

$$\overline{\frac{\partial w}{\partial t}} + \overline{u\frac{\partial w}{\partial x}} + \overline{v\frac{\partial w}{\partial y}} + \overline{w\frac{\partial w}{\partial z}} = -\frac{1}{\rho}\overline{\frac{\partial p}{\partial z}}, \tag{5.57}$$

where $g_y = -9.8ms^{-2}$, and similarly, equation 5.53 is written as

$$\frac{\partial u}{\partial x} + \frac{\partial v}{\partial y} + \frac{\partial w}{\partial z} = 0. \tag{5.58}$$

Results from the first stereoscopic PIV measurements which is described in section 3.3, are used in order to compute as many terms in equation 5.54 as possible. Equation 5.57 is completely known, with equation 5.58 giving $(\partial w/\partial z)$ (cf. equation 5.44). The only two terms that cannot be computed are $w\,(\partial u/\partial z)$ and $w\,(\partial v/\partial z)$. The three acceleration terms $\partial u/\partial t$, $\partial v/\partial t$ and $\partial w/\partial t$ can be computed by equation 3.4, while all the spatial derivatives can be computed by the Pade approximation scheme (see section 5.1.1). The first stereoscopic PIV measurement is only applied to $Re = 41280$ rings; the three components of the pressure gradient of these rings are presented in figure 5.37 in similarity coordinates. The relationship between the dimensional and the corresponding similarity pressure gradient per unit mass of fluid can be derived from equation 4.9, because the velocity vector $\boldsymbol{u}$ decay is well predicted by the similarity theory, and so is $D\boldsymbol{u}/Dt$. In particular,

$$\left\langle \frac{1}{\rho}\overline{\nabla p} \right\rangle = \left(\frac{1}{\rho}\overline{\nabla p} \right) \left(\frac{\rho}{I} \right)^{\frac{1}{4}} (t - t_o)^{\frac{7}{4}}, \tag{5.59}$$

where $\langle\rangle$ here, and in this section, denotes a similarity quantity.

Because the flow of this study is of constant density, the gravity term g_y simply contributes to a hydrostatic pressure, which also takes the same effect in a still fluid, it is not included when plotting figure 5.37. It is the pressure due to the dynamics of the ring that is of interest. Moreover, because g_y is constant, mathematically, it cannot be included in the time-dependent similarity scaling of equation 5.59.

Two primary conclusions can be drawn from the pressure gradient plots in figure 5.37: first, the pressure gradient in the azimuthal direction, $\left\langle (1/\rho)\left(\overline{\partial p/\partial z}\right)\right\rangle$

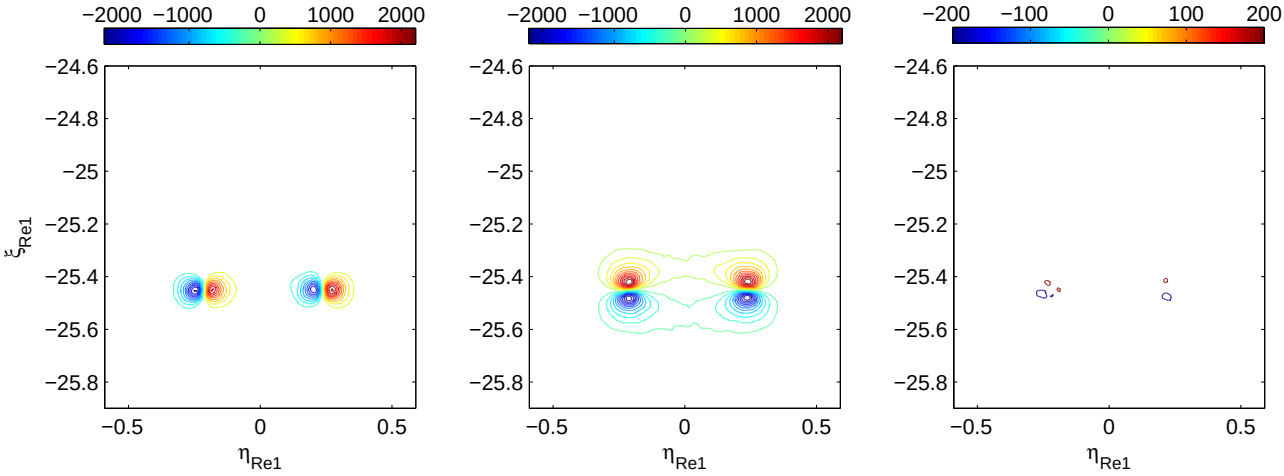

Figure 5.37: Pressure gradients in the three principle directions computed from equation 5.54 with the gravity term g_y excluded; from left to right: $\left\langle (1/\rho)\left(\overline{\partial p/\partial x}\right)\right\rangle$, $\left\langle (1/\rho)\left(\overline{\partial p/\partial y}\right)\right\rangle$, $\left\langle (1/\rho)\left(\overline{\partial p/\partial z}\right)\right\rangle$ in similarity coordinates. Higher levels in the core centre area are not shown.

(note that the plot is for the centre plane in Cartesian coordinates), is negligible compared to the in-plane components $\left\langle (1/\rho)\left(\overline{\partial p/\partial x}\right)\right\rangle$ and $\left\langle (1/\rho)\left(\overline{\partial p/\partial y}\right)\right\rangle$, meaning that there is an extremely weak, if any, azimuthal pressure gradient existing, which might be responsible for the weak azimuthal velocity (see section 7.2); second, the distribution of the in-plane pressure gradients in the η and ξ directions, which are of about the same magnitude, are associated with the centrifugal acceleration for the vortex core to rotate in the centre plane. In the moving reference frame seen from the bubble[1], if the particle paths close to the core centroid are approximately circular, the relationship of the pressure gradient and the centrifugal acceleration is expressed as

$$-\frac{1}{\rho}\frac{\partial p}{\partial r} = \frac{v^2}{r}\widehat{\mathbf{r}}, \tag{5.60}$$

where $\widehat{\mathbf{r}}$ is the unit (inward) normal vector; v is the particle speed, and r is the radius of the path considered. The minus sign is to make the direction of the pressure gradient and the centrifugal acceleration consistent. To make the second

[1]It will be shown later in this section that, change of reference frame will not alter the pressure distribution, if it is presented in similarity space.

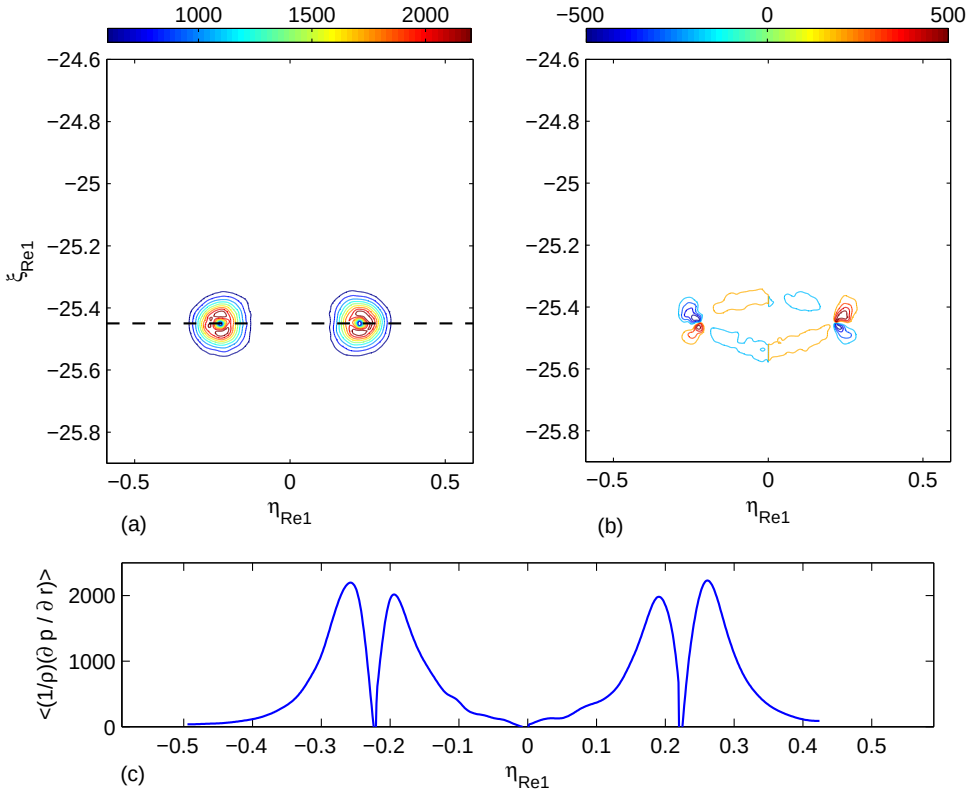

Figure 5.38: The centrifugal acceleration associated with the (radial) pressure gradient (equation 5.60), plotted in similarity coordinates. (a): the local radial component $\left\langle (1/\rho)\left(\overline{\partial p/\partial r}\right)\right\rangle$, (b): the local tangential component $\left\langle (1/\rho)\left(\overline{\partial p/\partial \beta}\right)\right\rangle$, (c): the intensity distribution along the trace −− in (a).

point clearer, the pressure-gradient distribution in the vicinity of the two cores are plotted in figure 5.38, in local polar coordinates.

The pressure gradients in the Cartesian coordinates (the similarity coordinates) can be converted to local radial and tangential pressure gradients for each core in figure 5.37: $p(\xi,\eta) \mapsto p(r,\beta)$, where r and β are the local radial and angular coordinates of a point with respect to each of the cores, β being positive anti-clockwise. In particular:

$$\begin{aligned}
\left\langle \frac{1}{\rho}\overline{\frac{\partial p}{\partial r}} \right\rangle &= \left\langle \frac{1}{\rho}\overline{\frac{\partial p}{\partial y}} \right\rangle \sin\beta + \left\langle \frac{1}{\rho}\overline{\frac{\partial p}{\partial x}} \right\rangle \cos\beta \\
\left\langle \frac{1}{\rho}\overline{\frac{\partial p}{\partial \beta}} \right\rangle &= \left\langle \frac{1}{\rho}\overline{\frac{\partial p}{\partial y}} \right\rangle \cos\beta - \left\langle \frac{1}{\rho}\overline{\frac{\partial p}{\partial x}} \right\rangle \sin\beta.
\end{aligned} \tag{5.61}$$

When applying equation 5.61, the left half and the right half of the flow field have to be treated separately, and for each half, the origin is set at the corresponding core centroid, which can be read from (ξ, η) or table 8.1.

Figure 5.38 (a) or (c) can also serve as a criterion to estimate the vortex ring core radius, i.e. by locating the radius at which $\left\langle (1/\rho)\left(\overline{\partial p/\partial r}\right)\right\rangle$ is maximum.

Returning to figure 5.37, note that the azimuthal pressure gradient is completely determined (or computed), see equation 5.57. The two terms which cannot be computed, $\left\langle \overline{w\partial u/\partial z}\right\rangle$ and $\left\langle \overline{w\partial v/\partial z}\right\rangle$ are not necessarily zero, because in an individual ring, they should not be zero due to the turbulent nature. To have a reasonable guess of the magnitude of these two terms from the data available, it is estimated that in an instantaneous ring, $|w\partial u/\partial z| \approx |w\partial u/\partial x|$ and $|w\partial v/\partial z| \approx |w\partial v/\partial x|$. The contour plots of these two estimated terms show that their magnitudes are less than 10% of the terms plotted in figure 5.37. The plots are not shown here. The estimated terms do not have any physical meaning; they are only expected to be mathematically similar to the non-computable terms.

It is also interesting to compare the relative magnitudes of the in-plane time-dependent acceleration term $\left\langle \overline{\partial \boldsymbol{u}/\partial t}\right\rangle$ and the convection term $\langle \overline{\boldsymbol{u}\cdot\nabla\boldsymbol{u}}\rangle$ in equation 5.54. The plots are presented in figure 5.39 and 5.40. Because the azimuthal components of these terms are very small and insignificant, they are not plotted.

The time dependent acceleration of the radial velocity component $\left\langle \overline{\partial u/\partial t}\right\rangle$ is about three times larger than that for the streamwise velocity $\left\langle \overline{\partial v/\partial t}\right\rangle$. This is not surprising, because the ring travels in the streamwise direction at a considerable speed, see section 5.1.3; in particular, if one examines the velocity field of an instantaneous ring, which is similar to figure 5.20 and 5.21, in zones of the highest velocity gradients (near the core, shown by the contour density), contour shapes are parallel with the ring travel direction for the V component but perpendicular for the U component. Therefore the change of U over a small time is expected to be larger. The contours of time-dependent acceleration terms are noisier compared to the contours of the convection terms. The convective accelerations in the radial and streamwise directions are of similar intensities.

After the pressure gradients are known, it is possible to estimate the pressure distribution in the PIV measurement plane. This is done by first computing the

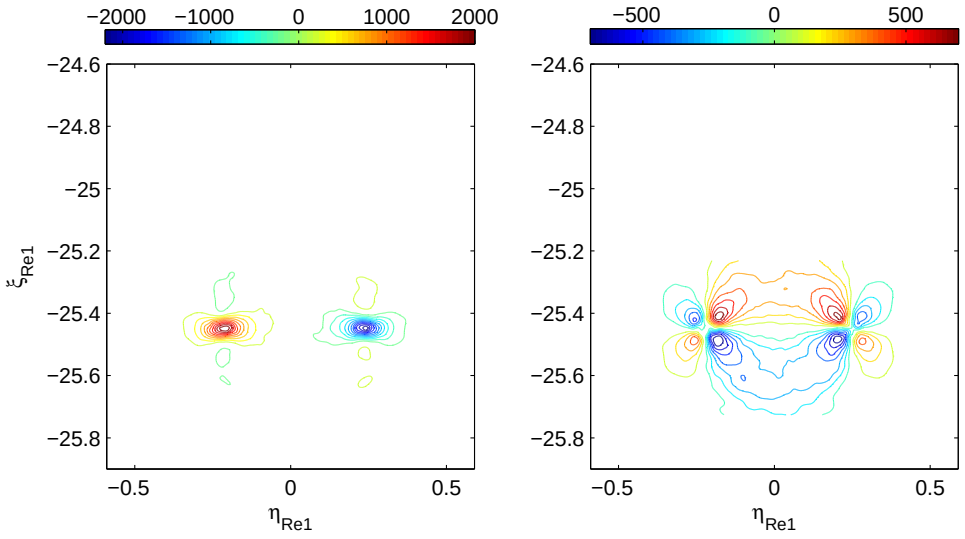

Figure 5.39: The in-plane acceleration terms: $\left\langle \overline{\partial u/\partial t} \right\rangle$ and $\left\langle \overline{\partial v/\partial t} \right\rangle$ in similarity coordinates. Higher levels in the core centre area are not shown.

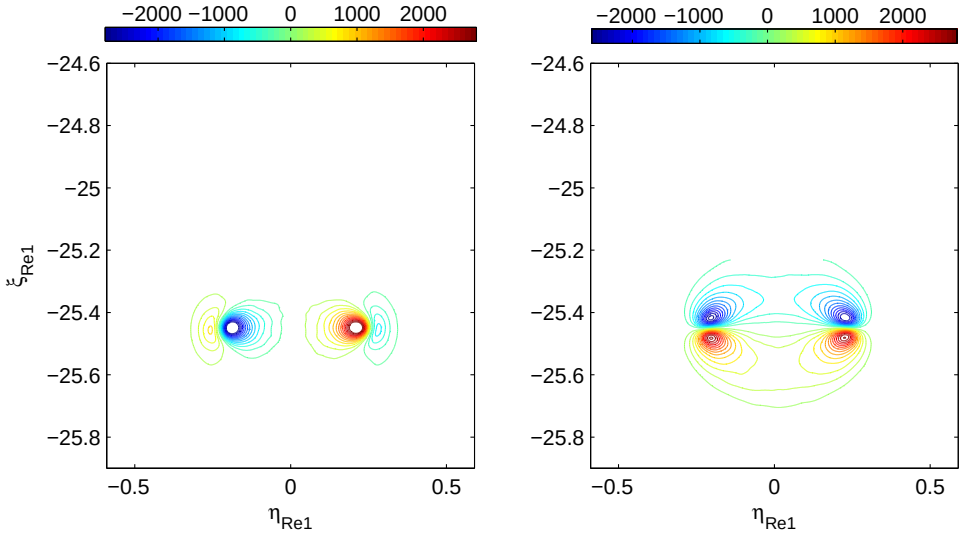

Figure 5.40: The in-plane convection terms of the material derivative: $\left\langle \overline{u\,(\partial u/\partial x)} + \overline{v\,(\partial u/\partial y)} \right\rangle$ and $\left\langle \overline{u\,(\partial v/\partial x)} + \overline{v\,(\partial v/\partial y)} \right\rangle$ in similarity coordinates. Higher levels in the core centre area are not shown.

pressure on the ring centre trajectory, and then integrating along the radial (x) direction. This can be written as

$$\left.\frac{1}{\rho}p(y)\right|_x = \int_0^x \frac{1}{\rho}\frac{\partial p(y)}{\partial x}\,\mathrm{d}x + \left.\frac{1}{\rho}p(y)\right|_{x=0}. \tag{5.62}$$

In this section $p(y)$ denotes the pressure distribution in the y direction. It does not mean that pressure p is only a function of y, Since p is a function of all three spatial variables x, y, z.

The first term on the right side of equation 5.62 can be computed by numerical integration of the data from figure 5.37. The hydrostatic term g_y is again excluded, because this term simply gives a pressure distribution of $p(y) = -\rho g y$. There are two experimentally independent ways to calculate $p(y)$ on the ring centre trajectory. One is the direct integration along the y direction using $(1/\rho)\,(\partial p/\partial y)$ obtained earlier. The other one does not require the pressure gradients, i.e. it does not need highly temporally resolved velocity information. The second method, which involves solving the steady Bernoulli equation, can serve as a validation of the pressure-gradient computation, and it is illustrated first below.

In an axisymmetric vortex ring, there must be a streamline on the axis of symmetry, i.e. it is a single-valued streamfunction on the axis of symmetry (see section 5.1.5)[1]. Moreover, on this streamline, only streamwise velocity exists. Therefore, the pressure distribution $p(y)$ on $x = 0$ can be calculated by Bernoulli equation. It must be stressed that, in a fixed reference frame (e.g. one attached to the tank or the camera), because the ring structure is moving downstream, the flow field is unsteady: $\partial \boldsymbol{u}/\partial t \neq 0$, and the steady Bernoulli equation is invalid. In order to overcome this problem, a uniform upwash flow against the ring at a velocity equals to the ring's instantaneous translation velocity is superimposed, after which the flow pattern would be just like that plotted in figure 5.11. Because the ring celerity is not constant, neither is the superimposed velocity, the resultant velocity is also a function of time; the unsteady problem is still not solved. Equation 5.56 in this situation is written as

$$\left.\frac{\partial\,(v-u_t)}{\partial t}\right|_{x=0} + (v-u_t)\left.\frac{\partial\,(v-u_t)}{\partial y}\right|_{x=0} = -\left.\frac{1}{\rho}\frac{\partial p}{\partial y}\right|_{x=0}; \tag{5.63}$$

[1]Here it is assumed that the wake of the ensemble-averaged turbulent vortex ring is also axisymmetric.

note that the ring translation velocity u_t is negative. Nevertheless, in similarity space, equation 5.63 appears steady. It is because all the terms in the equation obey the same similarity scaling, and all the time functions can be cancelled. Therefore, in similarity variables, equation 5.63 is written as

$$\left\langle \frac{\partial \left(V - U_t\right)}{\partial t} \right\rangle \Bigg|_{\eta=0} + \left(V - U_t\right) \frac{\partial \left(V - U_t\right)}{\partial \xi} \Bigg|_{\eta=0} = - \left\langle \frac{1}{\rho} \frac{\partial p}{\partial y} \right\rangle \Bigg|_{\eta=0}, \tag{5.64}$$

and $\langle \partial \left(V - U_t\right) / \partial t \rangle = 0$. It is necessary to clarify that this term means the time-dependent acceleration at a fixed point in the similarity space. So $\langle \partial V / \partial t \rangle \neq 0$ because the ring structure moves downstream in the similarity space at a constant speed U_t, which is a negative quantity, due to its self-induced velocity.

The steady Bernoulli equation can then be applied:

$$\left\langle \frac{1}{\rho} \overline{p(y)} \right\rangle \Bigg|_{\eta=0} + \frac{1}{2} \left[V(\xi) - U_t\right]^2 \Bigg|_{\eta=0} = \left\langle \frac{1}{\rho} \overline{p_1} \right\rangle \Bigg|_{\eta=0} + \frac{1}{2} \left[V_1 - U_t\right]^2 \Bigg|_{\eta=0}, \tag{5.65}$$

hence

$$\left\langle \frac{1}{\rho} \overline{\left(p(y) - p_1\right)} \right\rangle \Bigg|_{\eta=0} = -\frac{1}{2} \left[V(\xi) - U_t\right]^2 \Bigg|_{\eta=0} + \frac{1}{2} \left[V_1 - U_t\right]^2 \Bigg|_{\eta=0}, \tag{5.66}$$

where $V(\xi)$ and U_t can be obtained using the same method as discussed in section 5.1.2 and 5.1.3, and

$$\left\langle \frac{1}{\rho} \overline{p(y)} \right\rangle = \left(\frac{1}{\rho} \overline{p(y)} \right) \left(\frac{\rho}{I} \right)^{\frac{1}{2}} \left(t - t_o\right)^{\frac{3}{2}}. \tag{5.67}$$

In similarity space, the measured pressure distribution at any point on $\eta = 0$, in the reference frame which moves at a constant velocity of U_t, should read the same as if measured in the fixed reference frame. In other words, the physics is not affected by a new reference frame, as long as it is inertial and not moving at a too high speed, because *the principle of special relativity* states that:

"If a system of coordinates K is chosen so that, in relation to it, physical laws hold good in their simplest form, the same laws hold good in relation to any other system of coordinates K' moving in uniform translation relatively to K." (Einstein *et al.*, 1952).

The term $\left[V(\xi) - U_t\right]$ on $\eta = 0$ is plotted in figure 5.41 (a) and the pressure distribution $\left\langle (1/\rho) \overline{\left(p(y) - p_1\right)} \right\rangle$ on $\eta = 0$ computed from equation 5.66, is plotted

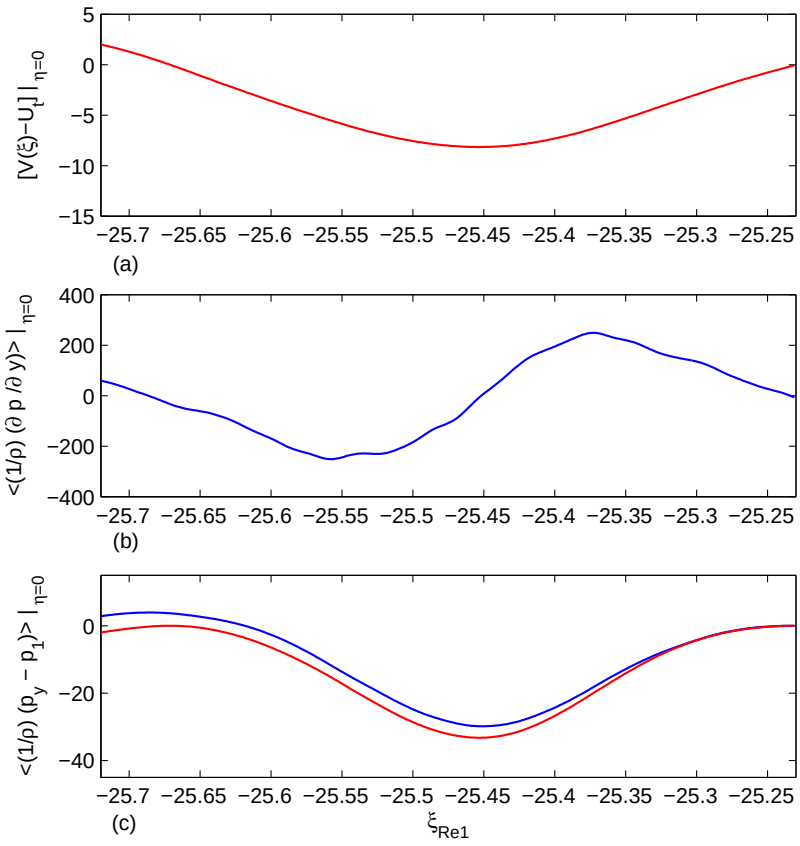

Figure 5.41: The estimated pressure on the ring centre trajectory, plotted against the streamwise distance by two approaches. (a) The ring streamwise velocity distribution on its centre trajectory as seen by the ring; (b) the streamwise pressure gradient distribution on the centre trajectory of the ring as seen by the cameras, computed from equation 5.54; (c) the pressure distribution on the ring centre trajectory as a function of the streamwise distance, – computed by equation 5.68, – computed by equation 5.66. All the quantities are plotted in similarity coordinates. The data is from the stereoscopic PIV measurements for $Re_1 = 41280$.

as the red trace in figure 5.41 (c). The reference point '1' is chosen to be the first point available in the streamwise direction.

As mentioned earlier, alternatively, the pressure distribution $\left\langle (1/\rho)\,\overline{p(y)}\right\rangle$ on the centreline $\eta = 0$ can also be inferred by a more straight-forward way, in the fixed or stationary reference frame. Because the pressure gradient contours in the three principle directions in the fixed reference frame have been obtained (figure 5.37), $p(y)$ on $x = 0$ can be calculated by integrating the streamwise pressure gradient:

$$\frac{1}{\rho}p(y)\bigg|_{x=0} = \int_1^y \frac{1}{\rho}\frac{\partial p(y)}{\partial y}\bigg|_{x=0} \mathrm{d}y + \frac{1}{\rho}p_1\bigg|_{x=0}. \tag{5.68}$$

The quantity $\left\langle (1/\rho)\,\overline{(\partial p/\partial y)}\right\rangle$ on $\eta = 0$ is plotted in figure 5.41 (b) and the pressure distribution $\left\langle (1/\rho)\,\overline{(p(y) - p_1)}\right\rangle$ on $\eta = 0$ computed by equation 5.68 is plotted as the blue trace in figure 5.41 (c). The scaling laws in equation 5.59 and 5.67 are used to convert the two terms into the corresponding similarity quantities.

Figure 5.41 (c) shows that the results from the two approaches agree well, with the blue trace, calculated from the pressure gradient integration, slightly exceeding the red trace, calculated from the steady Bernoulli equation. This could be attributed to the term $\left\langle \overline{w\partial v/\partial z}\right\rangle$, which cannot be measured. Another factor is that the pressure gradient terms are affected by the ring dispersion more than the celerity, because the individual ring celerity can be obtained from PIV measurements directly and are not affected by small dispersions much; while pressure gradients are, because they are inferred by spatial derivatives, which are strong functions of dispersion.

Figure 5.41 shows a limited region along the streamwise distance, approximately the bubble size, although it is the most important part of the flow field. In order to see the pressure distribution further outside the bubble, figure 5.41 is re-plotted in figure 5.42 using the results from the two-dimensional PIV measurements of $Re = 20039$ rings (the FOV for the two-dimensional PIV measurements is about twice as big as the FOV of stereoscopic PIV measurements). Note that the computable terms in equation 5.55 and 5.56 are the same for two-dimensional and stereoscopic PIV measurements.

The Reynolds number independence is again verified by comparing figure 5.41 and 5.42. They both indicate a maximum dimensionless pressure difference of

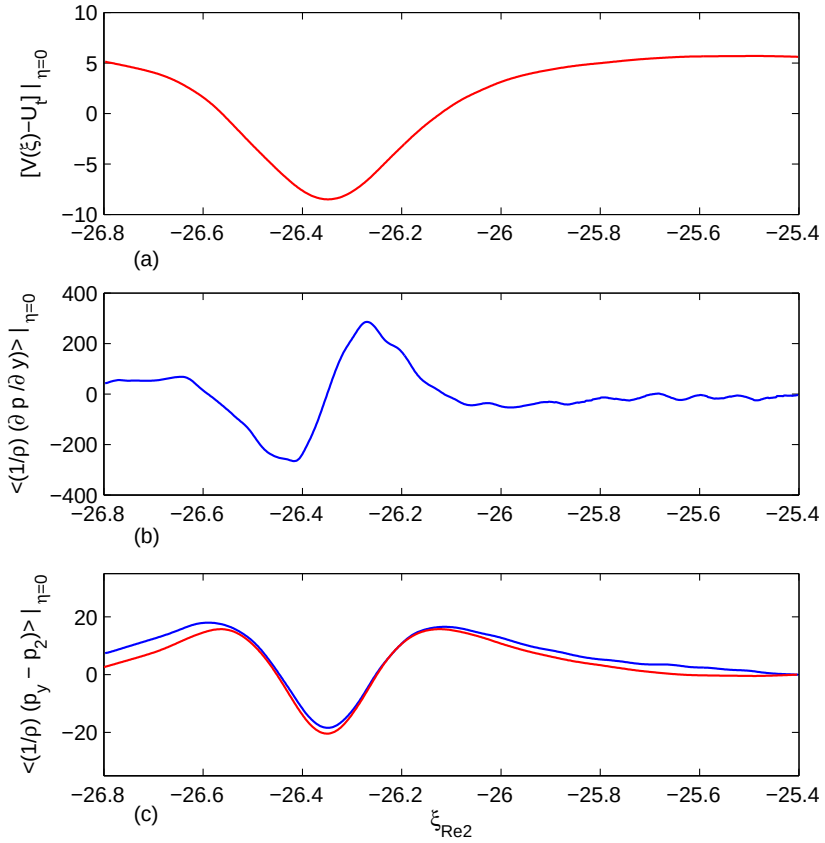

Figure 5.42: Re-plot of figure 5.41 for $Re_2 = 20039$ rings using the data from two-dimensional PIV measurements. The subscript 2 refers to a point different from point 1 in figure 5.41 and equation 5.66.

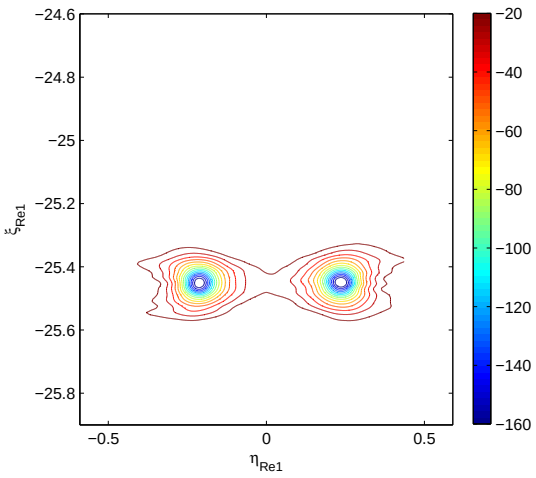

Figure 5.43: The pressure field in the PIV measurement plane computed from equation 5.62. Contours are plotted from stereoscopic PIV data. The very weak positive valued contours are not plotted. $Re_1 = 41280$.

about 40. The plots of $\left\langle (1/\rho)\,\overline{(\partial p/\partial y)} \right\rangle$ show a higher maximum intensity difference in $Re = 20039$ rings. This is because on the centreline, the low-magnitude $\left\langle (1/\rho)\,\overline{(\partial p/\partial y)} \right\rangle$ is 'contaminated' by the higher levels from the core area due to stronger dispersion of the lower Reynolds number rings; see figure 5.27. Moreover, the influence of the wake on the streamwise pressure gradient is also clear in figure 5.42 (b); see the wavy portion upstream. Note also that the temporal error levels when computing the time-dependent acceleration term $\mathcal{O}(\Delta t)$ (see equation 3.4) are different due to different FOVs and Reynolds numbers for the different experiments. The error levels are of order $0.002sec$ and $0.005sec$ respectively, with the one for the stereoscopic PIV measurement lower. Because of the computational error of the other terms of the incompressible Euler equation, and the terms which cannot be computed, this error is not critical, and is presumably negligible.

When the pressure distribution on the ring centre trajectory (axis of symmetry) is obtained, the pressure distribution in the entire PIV plane is readily computed by equation 5.62. This is shown in figure 5.43.

The pressure magnitude plotted in figure 5.43 is based on the reference pressure p_1 in equation 5.65, so it is the *relative* magnitude. The contour shape agrees with figure 5.38 (a) which shows that the pressure is balanced by the centrifugal

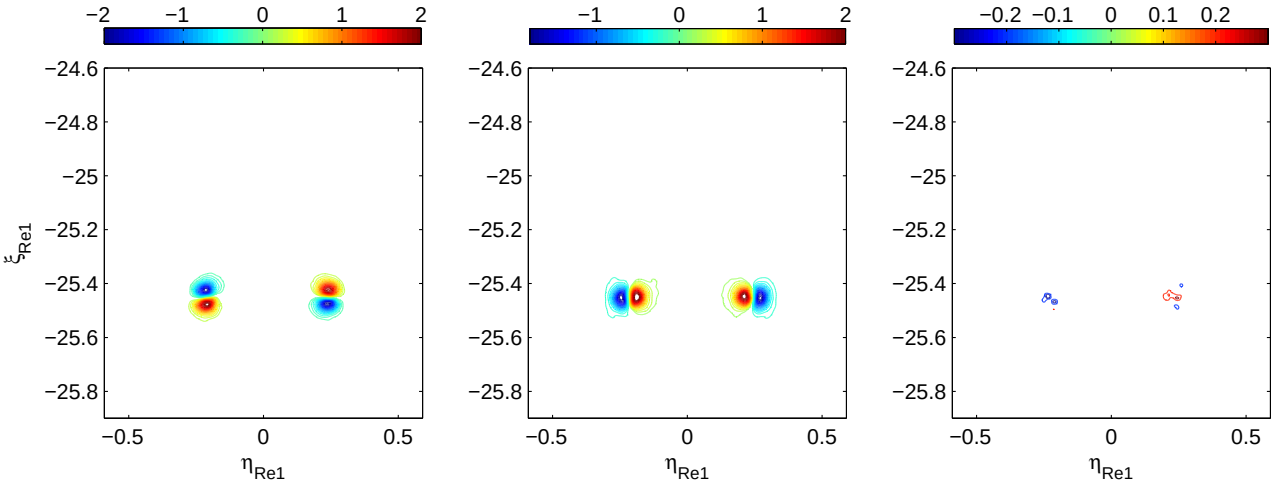

Figure 5.44: The viscous terms reflected in the PIV measurement plane. From left to right: $\left\langle \nu \left(\overline{\partial^2 u/\partial x^2 + \partial^2 u/\partial y^2} \right) \right\rangle$, $\left\langle \nu \left(\overline{\partial^2 v/\partial x^2 + \partial^2 v/\partial y^2} \right) \right\rangle$, $\left\langle \nu \left(\overline{\partial^2 w/\partial x^2 + \partial^2 w/\partial y^2} \right) \right\rangle$.

acceleration. The minimum relative pressure in the flow field occurs at the two core centroids.

The pressure contours shown in figure 5.43 should be roughly correct, although the derivation does not start from the complete incompressible Navier-Stokes equation. One may raise the question as follows: as velocity decreases away from the ring centre, the local Reynolds number decreases, the viscous terms become of a similar order to the inertial terms, even if they are small; this means that physically, is it not suitable to simplify the incompressible Navier-Stokes equation to the incompressible Euler equation. Instead, solutions of the full incompressible Navier-Stokes equation become necessary; however, the spatial resolution of this experiment may not be enough to correctly estimate the viscous effect, which is normally only important at very small scales. The fact is that away from the ring centre, the shear, or the strain rate is not expected to be large, so the viscous term can still be insignificant. At larger spatial resolution, viscous terms always remain at an insignificant level; see figure 5.44. Note that the contour levels in figure 5.44 are only 0.1% of those in figure 5.37.

The scaling law of the viscous term is the same as for the pressure gradient term,

with

$$\left\langle \nu\overline{\nabla^2 \boldsymbol{u}} \right\rangle = \left(\nu\overline{\nabla^2 \boldsymbol{u}} \right) \left(\frac{\rho}{I} \right)^{\frac{1}{2}} (t - t_o)^{\frac{3}{2}} . \tag{5.69}$$

Note that $\left\langle \overline{\partial^2 u/\partial z^2} \right\rangle$, $\left\langle \overline{\partial^2 v/\partial z^2} \right\rangle$ and $\left\langle \overline{\partial^2 w/\partial z^2} \right\rangle$ are inaccessible, but they are expected to be very small, of the same order as the terms shown in figure 5.44.

Chapter 6

Turbulence Quantity Corrections

This chapter proposes a method to decompose the raw turbulence quantity into various factors. Because the flow field of turbulent vortex rings is not stationary, turbulence quantities are only computable by ensemble-averaging procedure. Thus, to correctly quantify the degree of turbulence due to velocity intensity fluctuation of a single ring, requires to ensemble-averaging points which are at the same relative location in the global structure of every ring. Various factors like core dispersion, bubble shape variation, can all be considered as turbulence sources, because single realisations are added regardless whether the core and the bubble position or shape are the same or not, as long as the bubble centres are at the same streamwise location (see section 5.1.1). An effort to estimate the quantitative contribution of these factors to the raw turbulence intensities as discussed in section 5.2 is presented in this chapter. Section 6.1 proves the importance of dispersion, section 6.2 and 6.3 describe the decomposition operations.

6.1 Source of turbulence

Since it is believed that core dispersion makes a significant contribution to the total turbulent stresses, it is logical to attempt to decompose the total Reynolds stresses τ into several possible contributions. In order to see the effect of dispersion on the results of turbulence stresses more intuitively, stresses generated from artificial dispersion are plotted in figure 6.1. An instantaneous velocity field is taken to act as an ensemble-averaged velocity field, then this field is slightly shifted to create

an artificial fluctuation, which is only due to dispersion but not shape variation. Mathematically the artificial fluctuation is written as

$$\begin{aligned} u'(x,y) &= u(x+\Delta x, y+\Delta y) - u(x,y) \\ v'(x,y) &= v(x+\Delta x, y+\Delta y) - v(x,y), \end{aligned} \tag{6.1}$$

where u' and v' denote the artificial fluctuation; u, v are the two velocity components. If there is no dispersion, $\Delta x = \Delta y = 0$, there will be no velocity fluctuation and these stresses vanish. The effect of the amount of dispersion on the stress magnitude is plotted in figure 6.1. For comparison purpose, the magnitudes of the real stresses $\int_S |-\rho\overline{u'u'}|\,\mathrm{d}x\mathrm{d}y$, $\int_S |-\rho\overline{v'v'}|\,\mathrm{d}x\mathrm{d}y$ $\int_S |-\rho\overline{u'v'}|\,\mathrm{d}x\mathrm{d}y$ (where S is the velocity field area) of $Re = 20039$ rings at about $8D$ downstream distance are about 0.01, 0.02 and 0.004 respectively, which can be deduced from figure 5.28. This corresponds to about $3 \sim 5mm$ ($6\% \sim 10\%$ D) dispersion. Note that this is just a very rough estimation; figure 5.28 and figure 6.1 are not really comparable because the real stresses are ensemble-averaged ones. The real dispersion level can be deduced from figure 5.27.

The decomposition of Reynolds stresses can be written as

$$\tau_{total} = \tau^{(1)}_{position} + \tau^{(2)}_{radius+tilt} + \tau^{(3)}_{intensity} + \tau^{(4)}_{shape}, \tag{6.2}$$

where τ_{total} represents the raw stresses which are shown from figure 5.23 to figure 5.25. Position, radius, tilt and shape are all apparent properties reflected by the core positions which might be due to azimuthal waves. These effects all come from the ensemble-averaging process. The same equation can also be applied to the turbulence production,

$$p_{total} = p^{(1)}_{position} + p^{(2)}_{radius+tilt} + p^{(3)}_{intensity} + p^{(4)}_{shape}. \tag{6.3}$$

The τ_{total} contours are directly obtained from the experiments, including all the factors on the right-hand-side of equation 6.2 and without any artificial correction. It now becomes possible to estimate the percentage of contributions to the raw stresses due to these factors. In this chapter, algorithms are designed in an attempt to separate and quantify the contributions from these factors. It should be stressed that the quantified results are not claimed to be accurate, since the accurate results would require ensemble realisations of fully three-dimensional data over a volume.

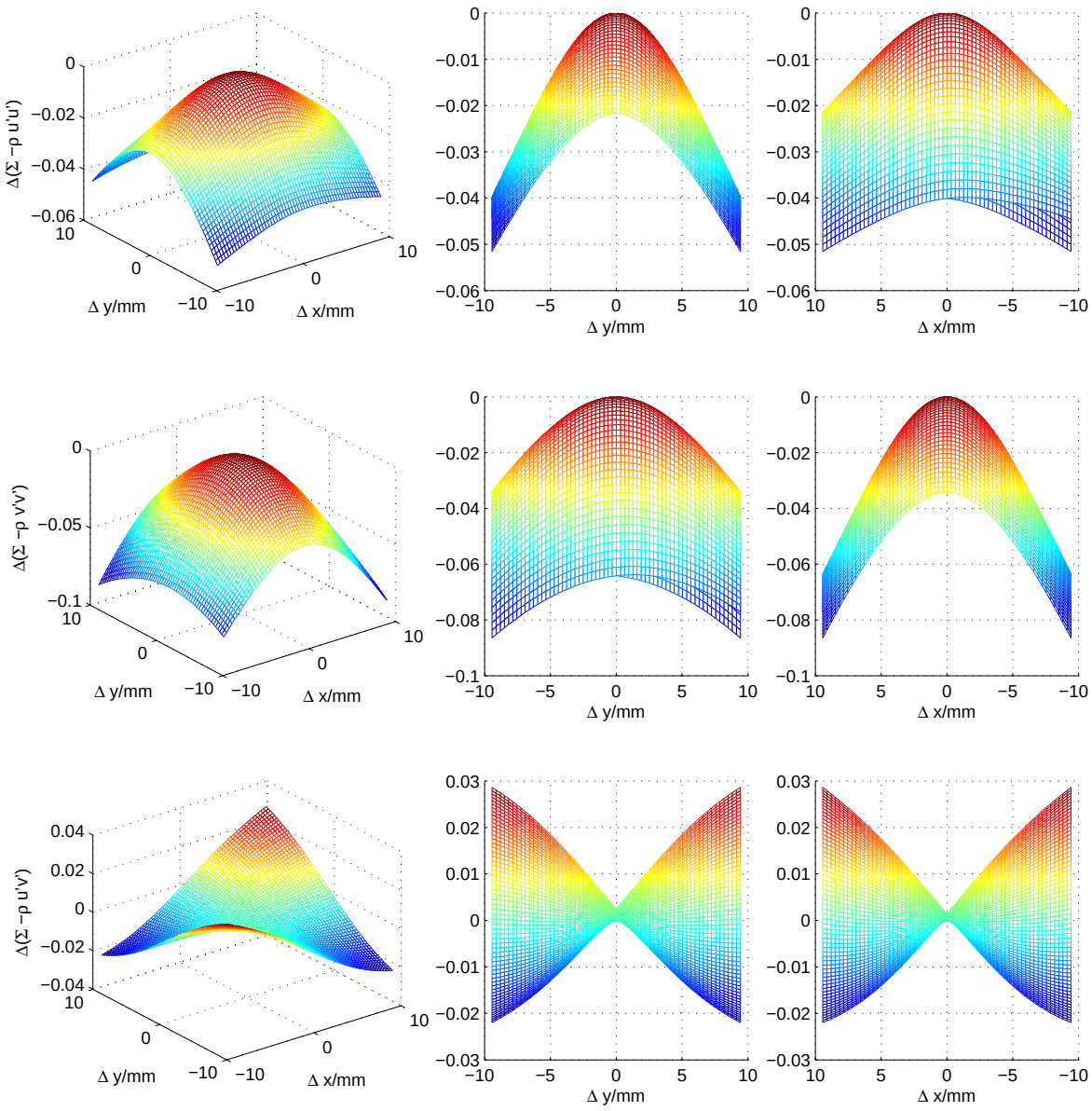

Figure 6.1: An example of the effect of dispersion on the three components of Reynolds stresses, $\int_S -\rho u'u'\,\mathrm{d}x\mathrm{d}y$, $\int_S -\rho v'v'\,\mathrm{d}x\mathrm{d}y$ and $\int_S -\rho u'v'\,\mathrm{d}x\mathrm{d}y$. An instantaneous ring of $Re = 20039$ at about $8D$ downstream from the orifice exit is tested, so the stresses are not ensemble averaged ones.

6.2 Centroid position shift

The easiest factor to filter out in equation 6.2 is (1), due to dispersion of position. In other words, the first algorithm is designed to shrink the core centroid footprint cluster at each station (see figure 5.26) to one point, or to bring down the curves in figure 5.27 towards zero. At each station described in section 5.1.1, the left and right halves of a single ring are considered to be uncorrelated, and each half is shifted until the core centroid of the corresponding half collapses with a destination point. The destination points are chosen to be the intersection points of each station line in a streamwise position and the fitting lines in figure 5.1. A typical destination point is shown in figure 5.26, which is the intersection of the left fitting line and station 102 ($5.55D$ downstream from the orifice exit). The shifting process can be divided into two steps:

1. *Shift in y direction.* Note that for one realisation (one ring), PIV cameras record hundreds of images based on the recording frequency set. The criterion of the image number selection from each realisation of the ensemble-averaging process has been described in section 5.1.1. The image number of each realisation is now reselected such that the centroid y-coordinate of each half of the ring should be closest to the corresponding station line. For instance near station 102 (see figure 5.26), the 50 image numbers are reselected such that the 50 footprints are close sufficiently to station 102, within $\pm 0.8mm$. The consequence of the y-shift is shown in figure 6.2. There are only 20 footprints shown, the reason for which will be given below. In fact there is no artificial shifting in this step, only the reselecting process is operated.

2. *Shift in x direction.* The images from the two cameras are connected giving the full FOV, after which the connected vorticity field is refined ten times by cubic spline interpolation such that the resolution is artificially increased by ten times. The benefit from this refinement is that the error in the x-direction shifting can be reduced to a very small amount. Note that the data points are discretized. For instance, the scatter of the footprints in figure 6.2 in the x-direction after this step will be within $\pm(1/10) \times 2.48mm = \pm 0.248mm$, where $2.48mm$ is the raw grid spacing. The ring radius at each station number

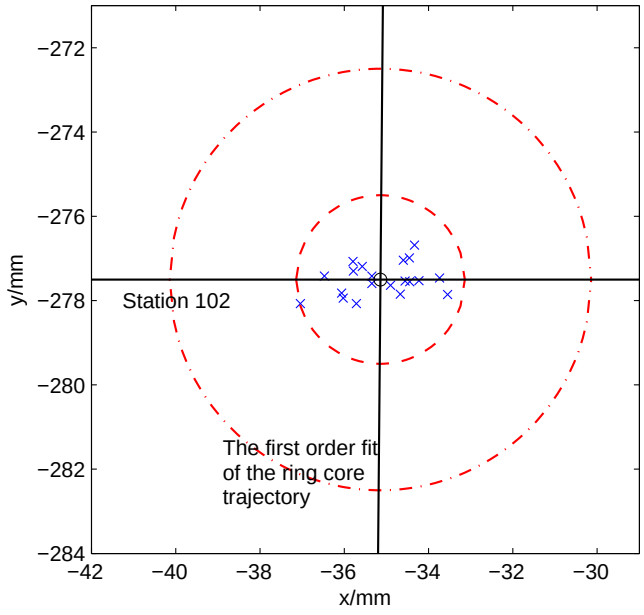

Figure 6.2: The left-hand-side core centroid footprints cluster reselected at station 102 (see figure 5.26) for 20 realisations of $Re = 41280$ cases. $\times$ denotes each of the core centroids; $--$ denotes a $2mm$ radius circle centred at $\circ$; $-\cdot-$ denotes a $5mm$ radius circle centred at $\circ$. The station 102 line and the averaged core centroid trajectory are also shown.

calculated from the fitting lines of figure 5.1 is used as the standard ring radius, regardless of the true radius of each ring produced. For example, at station 102, the standard radius is about $35mm$, or $0.7D$ (see the x-coordinate of '$\circ$' in figure 5.26 and 6.2). The standard radius is also marked in figure 6.3. For further averaging, each of the shifted velocity matrix needs to have the same size, therefore it is not possible to keep the width of the original FOV matrix. The new width is set to $2.0D$ (for half of the ring), giving the total width $4.0D$ (see figure 6.3), which is a suitable width for the x-direction shift.

The consequence of the x-axis and y-axis centroid shift is sketched in figure 6.3, where the left core centroid of two typical rings collapse at the destination point of station i.

A primary effect after the core centroid position shift is shown in figure 6.4. The first observation is that the maximum dimensionless vorticity levels of the rings at the two Reynolds numbers are comparable now (compared to figure 5.22). The second one is that the vorticity contours are slightly elongated, perhaps most obviously at the lowest contour level. This is because the deviations of the centroid cluster are not the same in the y-direction and the x-direction, within $\pm 0.8mm$ and $\pm 0.248mm$, respectively. Figure 6.5, 6.6, 6.7 and 6.8 show the three Reynolds stress contours and the production contour. It is clear that the maximum intensities of these contours are significantly reduced, compared with the raw quantity contours in section 5.2.1. A quantitative calculation of the reduction will be given later. The contour shapes are basically retained, with the core easily located, except for the axial and shear component of the $Re = 20039$ rings. Reasons for this are given below.

The shifting process described above does not filter out factor (2) in equation 6.2 and 6.3. This is because shifting in rectangular grids does not change the ring's apparent tilting angle (judged from the positions of the two cores) in the PIV plane, and it does not correct the curvature differences around the core due to the ring size difference. It is clearly shown in figure 6.3. The result of applying this process is an overestimation of the stresses towards the centre of the ring (towards the axis of symmetry). In an effort to reduce this overestimation, 20 realisations whose core centroids are closest to the destination points are used in the averaging process. Because of this, in figure 6.2, only 20 footprints are shown. This overestimation is

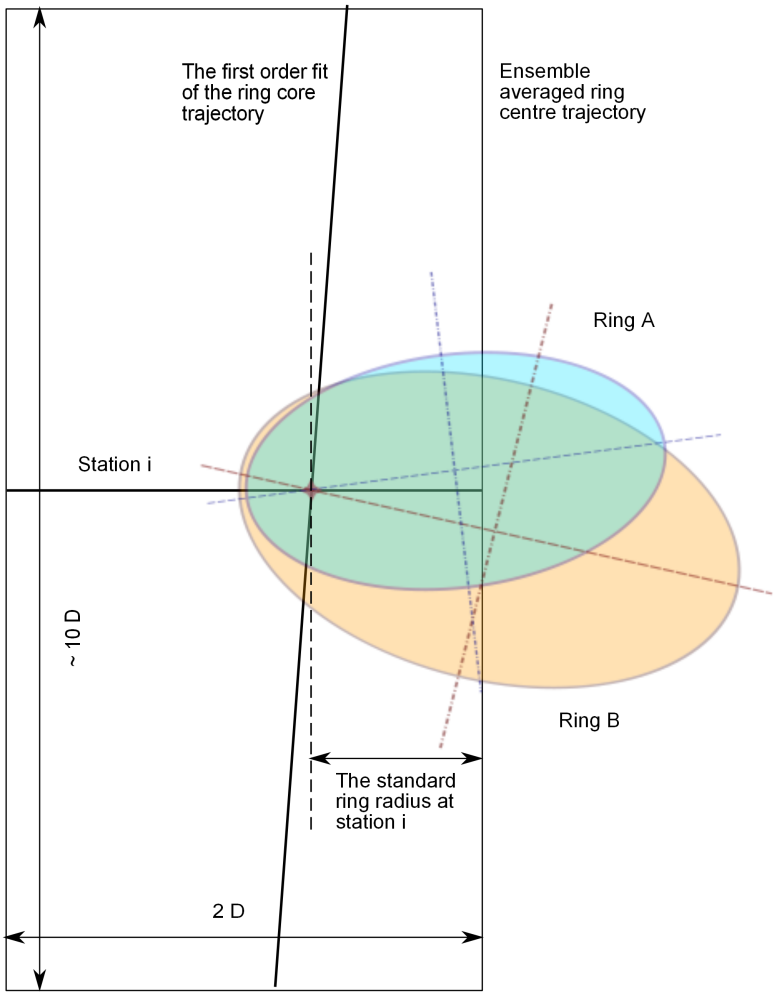

Figure 6.3: A schematic diagram showing the left halves of two typical vortex rings shifting towards station i. The diagram shows that the shifting process is not capable of filtering out the size and tilting angle effect. The sketch is not to scale and the size difference and the tilting angles are exaggerated for the sake of illustration.

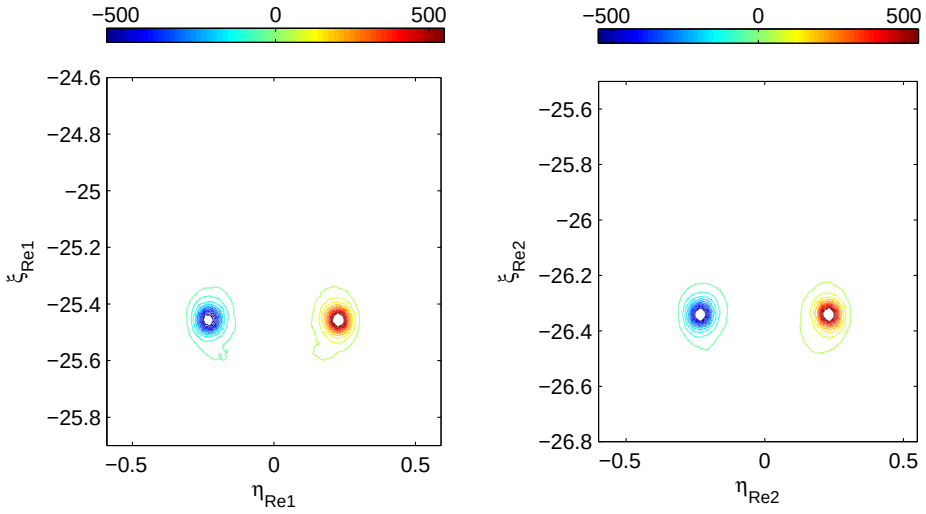

Figure 6.4: Vorticity $\partial V/\partial \eta - \partial U/\partial \xi$ contours in similarity coordinates, obtained from velocity contours, after applying centroid position shift.

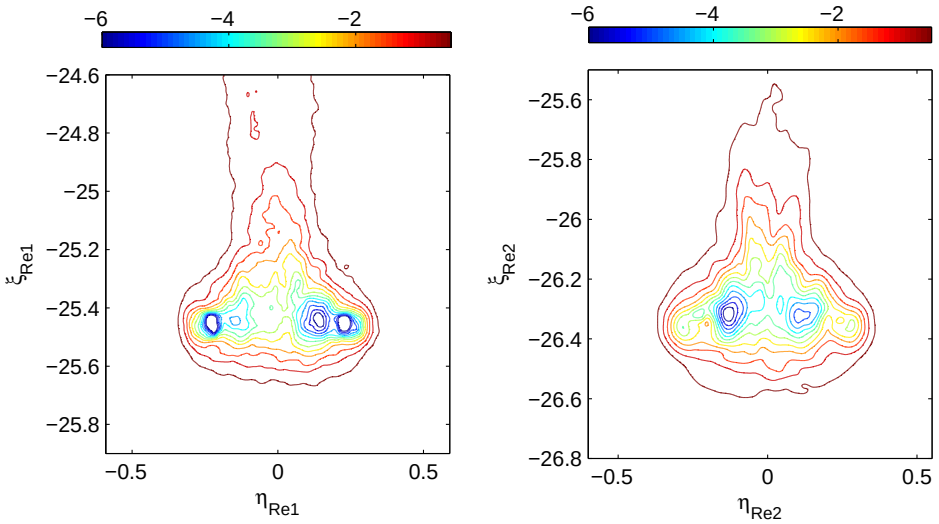

Figure 6.5: Radial normal Reynolds stresses $-\overline{U'U'}$ contours in similarity coordinates, after applying centroid position shift. Higher levels in the core centre area are not shown.

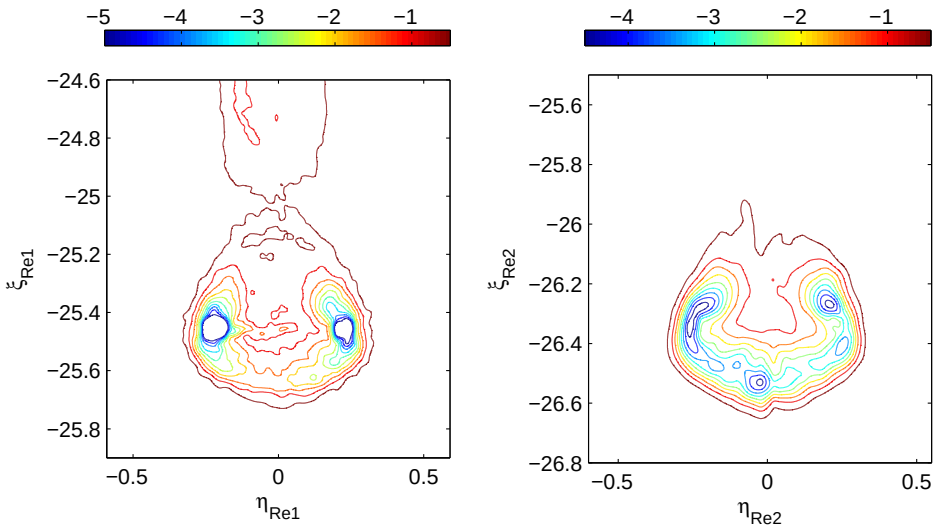

Figure 6.6: Axial normal Reynolds stresses $-\overline{V'V'}$ contours in similarity coordinates, after applying centroid position shift. Higher levels in the core centre area are not shown.

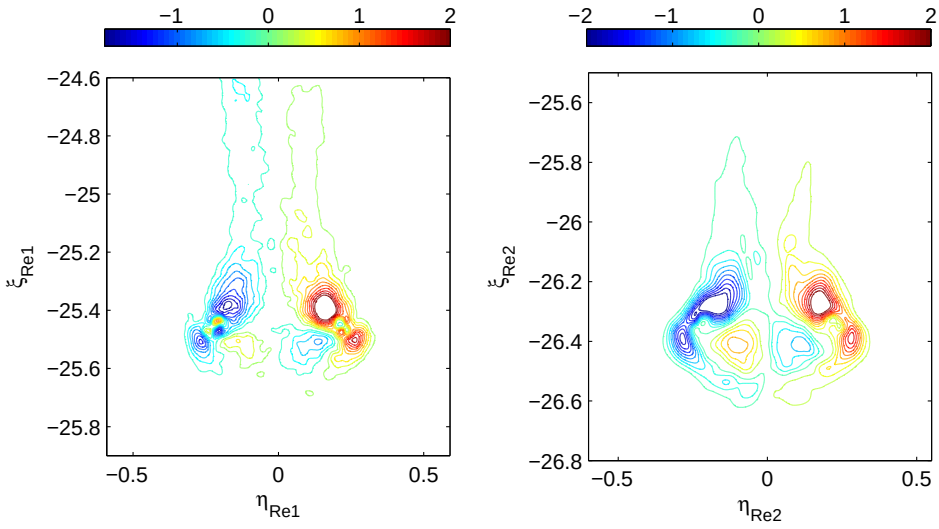

Figure 6.7: Reynolds shear stresses $-\overline{U'V'}$ contours in similarity coordinates, after applying centroid position shift. Higher levels in the core centre area are not shown.

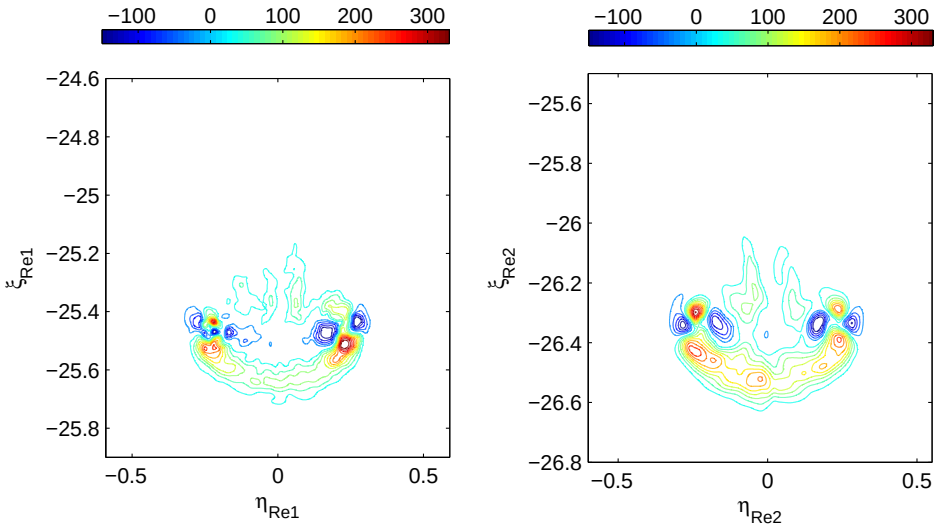

Figure 6.8: Turbulence production contours in similarity coordinates, after applying centroid position shift. Only the first four terms in equation 5.45 are included. Higher levels in the core centre area are not shown.

still clear though, for instance in figure 6.5, where an obvious secondary core appears on the inner side of the main core; and in figure 6.7, where the diagonal structures near the cores are amplified; and the wake in figure 6.8. Therefore the collapse of the apparent ring cores does not guarantee a good collapse of the ring bubbles.

The magnitudes of the total stress in the bubble region, equation 5.38, are plotted in figure 6.9. It shows that this method filters up to 30% of the total stresses, especially for Re_2, when the apparent dispersion is strong. Figure 6.9 illustrates the effectiveness of the filtering and clearly shows the size of the possible contribution of the apparent core-position dispersion to the total stresses. It should be noted that it includes the stress overestimation in the ring centre area. The magnitude of the production in the bubble volume will be given at the end of section 6.3.

6.3 Column decomposition

For the purpose of subtracting factor (2) from equation 6.2, a technique is borrowed from the analysis of Glezer & Coles (1990) that was applied to their LDV data. Each column in the resultant data mesh (the vector field mesh) is assumed to be

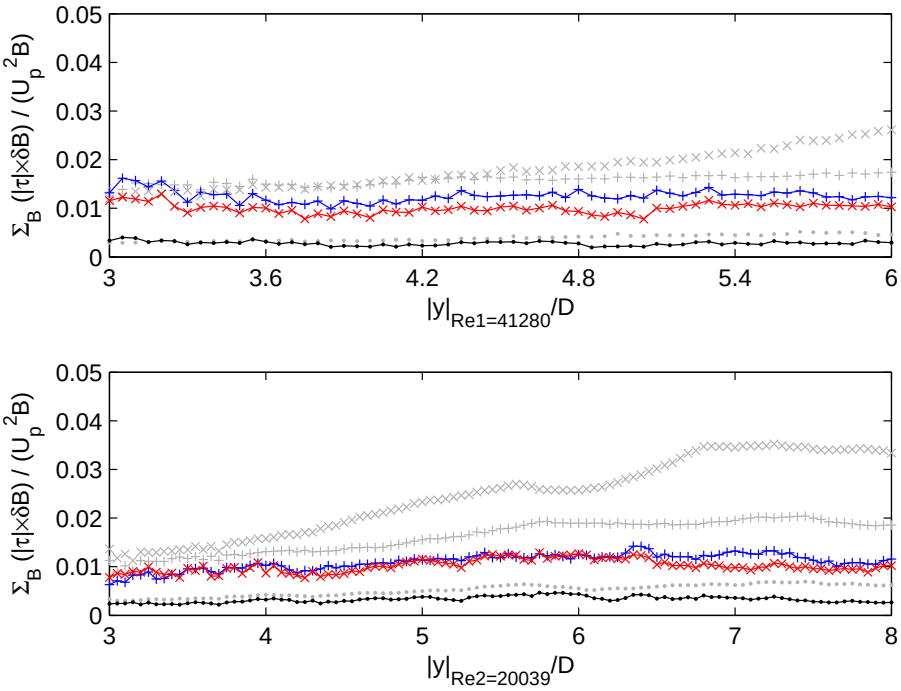

Figure 6.9: The summation of the magnitude of the Reynolds stress over the ring bubble area $\int_B |\tau| \, \mathrm{d}\boldsymbol{B}/U_p^2 B$ as a function of ring streamwise location after shifting each core centroid to the desired collapse point. τ: $-\overline{u'u'}$, $-\overline{v'v'}$ or $-\overline{u'v'}$; B: the rectangular region of $1.4D$ in streamwise direction and $2.4D$ in radial direction, see figure 5.11. $+$: axial Reynolds normal stress; $\times$: radial normal Reynolds stress; $\bullet$: Reynolds shear stress. The grey markers are reproduced from figure 5.28.

uncorrelated with the neighbouring columns. The velocity mesh grid for the two-dimensional PIV recording is 85×85, thus effectively there are 85 LDV testing stations across the radial direction. A single instantaneous realisation recorded by the PIV equivalently gives 85 LDV velocity traces. (It must be noted that they are not exactly equivalent, because LDV gives a velocity trace of a time function, while PIV results in a space function for a specific time.) In this way, data at each column has no idea about what happens in the neighbouring columns. The algorithm is summarised in the following steps.

1. If one column is considered, for each of the 50 rings produced, the PIV image number (at a particular time) corresponding to the minimum r.m.s. of velocity components with respect to the ensemble-averaged velocity components at that column is picked out. To reduce the computational expense, only ± 20 images of the original image number are involved in the searching process. (This corresponds to $\pm 52.6ms$ in $Re = 41280$ rings and $\pm 100ms$ in $Re = 20039$ rings.) The first ensemble-averaged velocity components are calculated from the raw averaging process which is described in section 5.1.1. These ensemble averaged values will be updated after the second step. This process is equivalent to the time-shifting process in Glezer & Coles (1990). However, instead of shifting the axial velocity component only to find the minimum r.m.s., in this method, both axial and radial components are taken into consideration. In order to take into account the small dispersion in the spanwise direction in the PIV plane, the neighbouring three columns (hence seven columns in total) are included for searching for the minimum r.m.s. PIV image number (time point). Therefore, for one realisation, there are in total $7 \times (2 \times 20 + 1) = 287$ u, v trace pairs involved in searching for a best-fit trace pair.

2. After the first step, there are 50 velocity trace pairs (including both u and v components) from 50 rings corresponding to one column station (the effective LDV station), after which these 50 r.m.s. values are further sorted to find the smallest 30 r.m.s. values. The final 30 trace pairs at one column station are used to find the new ensemble-averaged velocities of two components.

3. The processes described above are iterated to obtain the final result for one column. The same process is applied to all the 85 columns to obtain the final corrected two-dimensional velocity fields and hence the stress fields and production fields.

Figure 6.10 shows the 50 raw velocity traces at a typical column position, before the column shifting treatment. After the iteration, the best 30 fitted traces corresponding to that column are plotted in figure 6.11. The two figures clearly show the effect of the column shifting treatment: the level of fluctuation is significantly reduced. With more iterations applied, the fitting quality is expected to be improved (the r.m.s. values can be further reduced). Ideally, iterations would be repeated until some stress quantities, like the ones plotted in figure 6.13, converge to certain values, but more iterations will seriously increase the computational expense. Due to this consideration, only a single iteration is applied, but that already reduces the stress level remarkably, which will be shown later.

Notice that, at each column, the two velocity components in one pair are correlated, in other words, the r.m.s. mentioned above takes the minimum value of the following term

$$\sqrt{\frac{1}{N}\sum_{y=1}^{y=N}\left[u(y)-\overline{u}(y)\right]^2+\frac{1}{N}\sum_{y=1}^{y=N}\left[v(y)-\overline{v}(y)\right]^2}, \tag{6.4}$$

where N is the number of data points available in the streamwise direction. It should be stressed that velocity traces are not corrected by the circulation factor as for the LDV results. Multiplying circulation factors defined as

$$\digamma=\frac{\int_0^\infty \overline{u(y)}\mathrm{d}y}{\int_0^\infty u(y)\mathrm{d}y} \qquad \varkappa=\frac{\int_0^\infty \overline{v(y)}\mathrm{d}y}{\int_0^\infty v(y)\mathrm{d}y} \tag{6.5}$$

by each of the velocity trace will further reduce the fluctuation, i.e. bring each of the traces even closer to the averaged one (see figure 6.11). This is not attempted though: the reason will be given later.

A primary check for the effectiveness of this method is again by plotting the vorticity contours, which are presented in figure 6.12. The basic contour shapes and

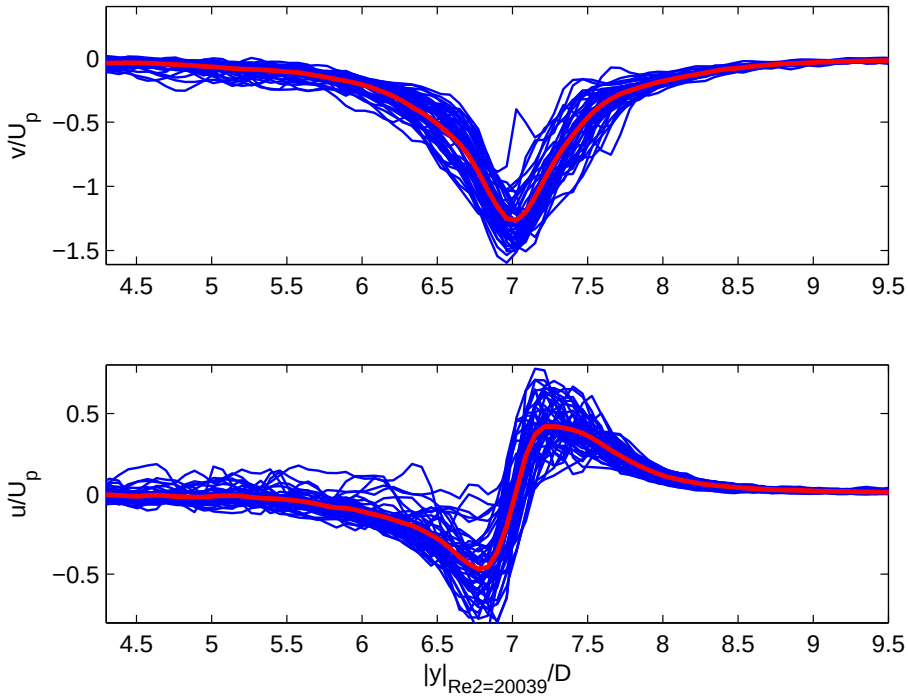

Figure 6.10: Typical velocity traces at one PIV data column scaled by effective piston velocity U_p at seven orifice diameters downstream from the orifice exit, before the column shifting process is applied. In this plot, all 50 realisations are shown by −, with the raw averaged traces shown by −. $U_p = 0.25m/s$; $Re = 20039$.

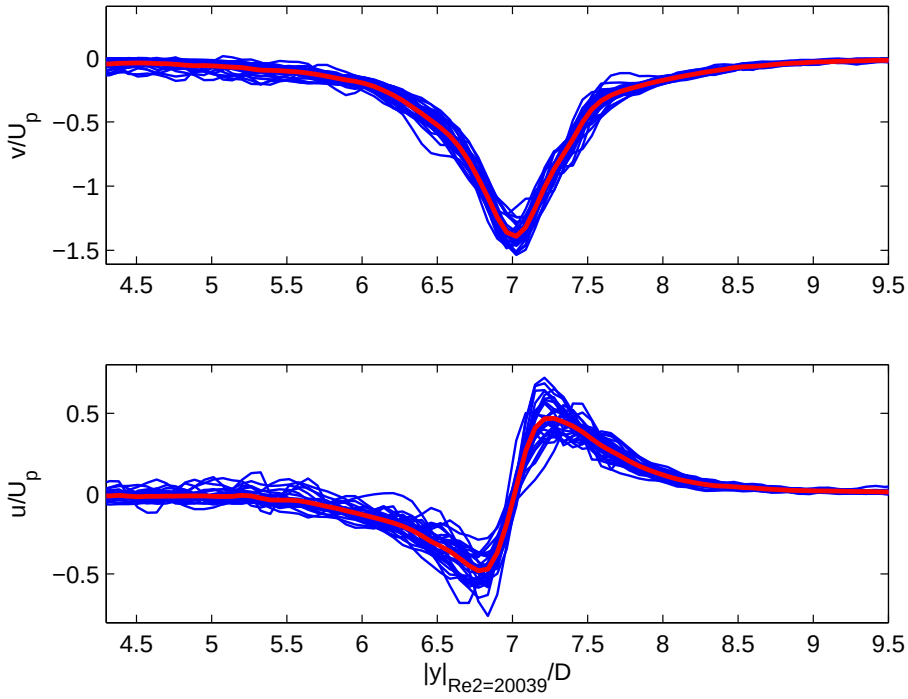

Figure 6.11: Typical velocity traces at one PIV data column scaled by effective piston velocity U_p at seven orifice diameters downstream from the orifice exit, after the column shifting process and the iteration is applied. In this plot, 30 traces with the minimum r.m.s. values are shown by −, with the iterated averaged traces shown by −. $U_p = 0.25m/s$; $Re = 20039$.

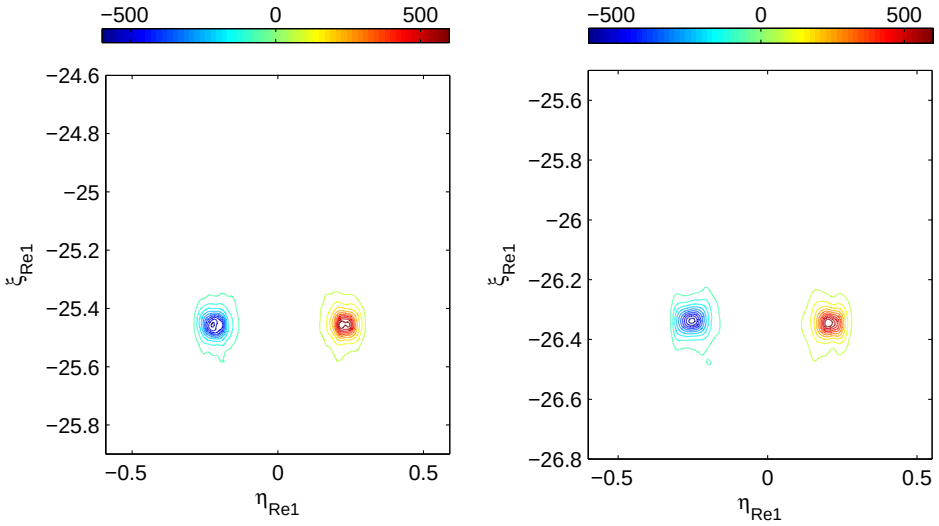

Figure 6.12: Vorticity $\partial V/\partial \eta - \partial U/\partial \xi$ contour in similarity coordinates, obtained from velocity contours, after applying column shift.

levels are comparable with figure 6.4. It is the lowest level, where the contour lines deviate from a quasi-closed circular loop, which reflects the effect of neighbouring column un-correlation.

The magnitudes of the three Reynolds-stress components in the ring bubble region are plotted in figure 6.13 . Note that the maximum scale in figure 6.13 is only 20% of that in figure 5.28 and figure 6.9. The stresses are also plotted in similarity scaling and shown in figure 6.14. This shows that stresses do not decay perfectly as similarity theory predicts (plots are still flat in figure 6.13), which means that either the testing range is not long enough, or factor (4) in equation 6.2 still plays a significant role which is subtracted. To subtract factor (4) requires that, on top of the algorithm described above, at each column the velocity traces need to be scaled to have the same standard deviation for both velocity components individually, e.g. by multiplying the circulation factors in equation 6.5 by each of the selected trace, but this process would decouple the two velocity components (i.e. destroy the Reynolds shear stress), which is undesirable. It is for this reason that this factor (4) is not processed. Note that the procedure used in the LDV results treated the u and v signatures differently and separately - something the researchers regretted at a later stage (as stated in Glezer & Coles, 1990). The decomposition procedure

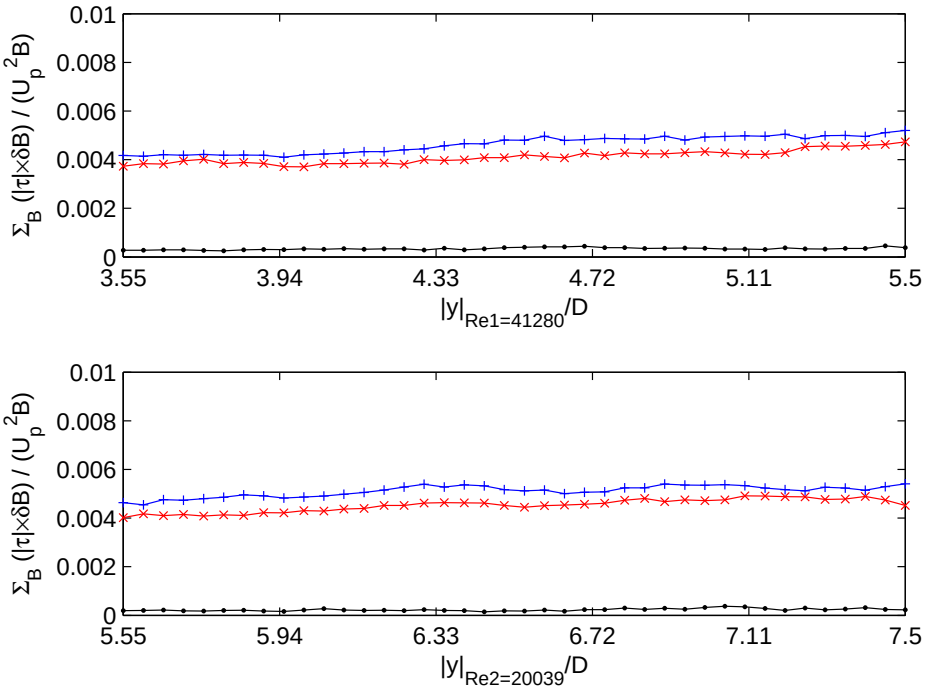

Figure 6.13: The summation of the magnitude of the non-dimensionalised Reynolds stress over the ring bubble area $\int_B |\tau| \, \mathrm{d}\boldsymbol{B}/U_p^2 B$ as a function of ring streamwise location after adopting the column decomposition method. τ: $-\overline{u'u'}$, $-\overline{v'v'}$ or $-\overline{u'v'}$; B: the rectangular region of $1.4D$ in streamwise direction and $2.4D$ in radial direction; see figure 5.11. $+$: axial Reynolds normal stress; $\times$: radial normal Reynolds stress; $\bullet$: Reynolds shear stress.

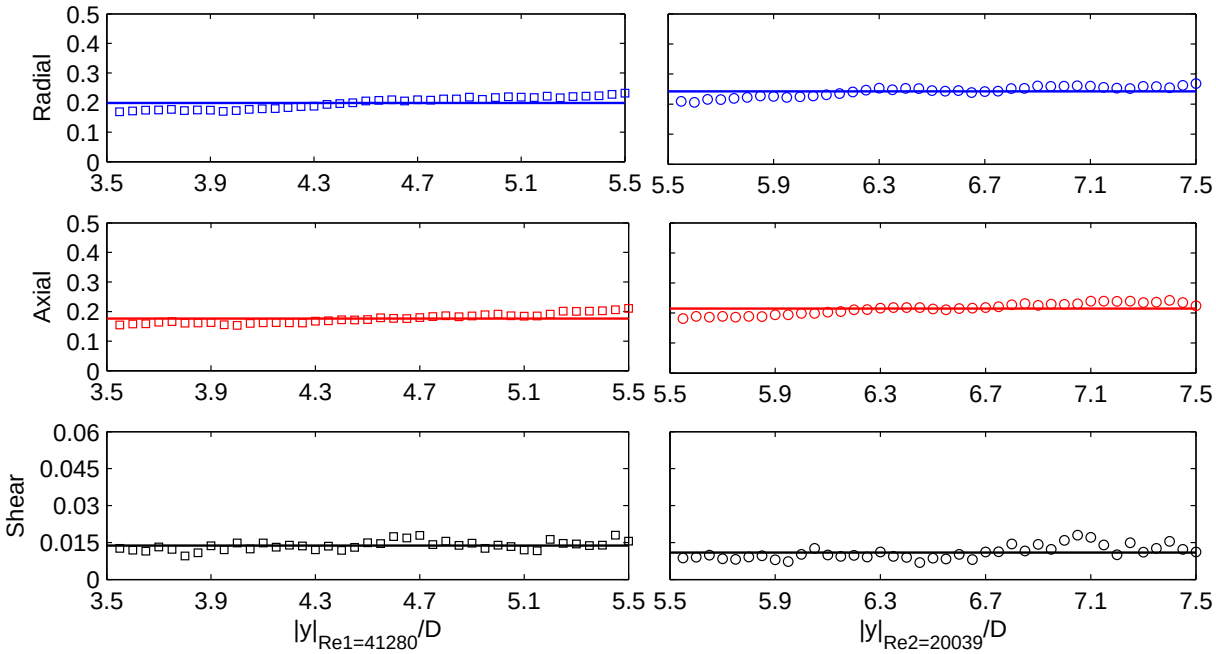

Figure 6.14: The magnitude of the non-dimensionalised Reynolds stresses in the bubble area scaled by the similarity scaling law as a function of ring streamwise location after the column decomposition method is applied. Radial component: $\int_B |-\overline{u'u'}|\mathrm{d}\boldsymbol{B}\,(\rho/I)^2\,(y-y_o)^4\,/\xi^4$; axial component: $\int_B |-\overline{v'v'}|\mathrm{d}\boldsymbol{B}\,(\rho/I)^2\,(y-y_o)^4\,/\xi^4$; shear component $\int_B |-\overline{u'v'}|\mathrm{d}\boldsymbol{B}\,(\rho/I)^2\,(y-y_o)^4\,/\xi^4$, according to equation 5.37. $\square$: Re_1 case; $\circ$: Re_2 case. $-$: the zero-order least-squares fits of $\square$ and $\circ$ with the fixed virtual origins y_o obtained from figure 5.1.

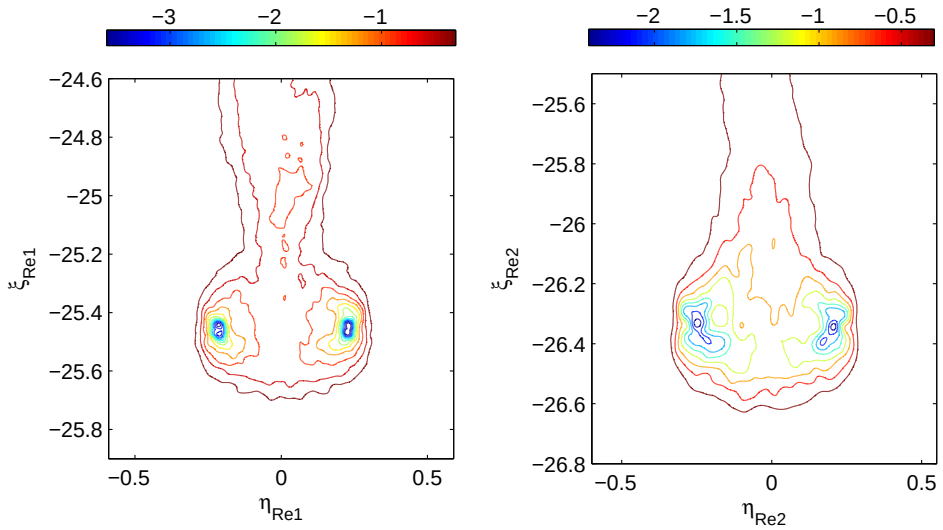

Figure 6.15: Contours of radial normal Reynolds stresses $-\overline{U'U'}$ in similarity coordinates after the column decomposition method has been applied.

here is then a significant improvement for this reason (and in other details).

The contours of the Reynolds stresses and the production are reproduced in figures 6.15 to 6.18, after the column decomposition method has been applied, or after factor (1) and (2) have been filtered from equation 6.2. Although they do not precisely obey the similarity theory, they are still scaled and presented in similarity coordinates, in order to check the quality of the fitting and to find the similarity constants, which will be listed in table 8.1. The stress intensities in the radial and axial components are comparable now, and the degree of symmetry is increased. Due to the low magnitudes, a very weak wake appears in the left figure of figure 6.16, but not in the right figure, nor in the left figure of figure 5.24. The wake here is not the one shed from the ring structure, but the one that belongs to the formation process. This formation wake is also visible in the left figure of figure 6.17, but it is merged with the wake shed from the ring bubble. It should be noted that, with correction, the values for the quantities are very similar to those found in the LDV results, whereas before correction they were significantly higher; see the plots in appendix D. Of course the LDV results were also corrected for dispersion but via a more complex procedure (which was necessary due to the fact that the researchers only had single-point measurements).

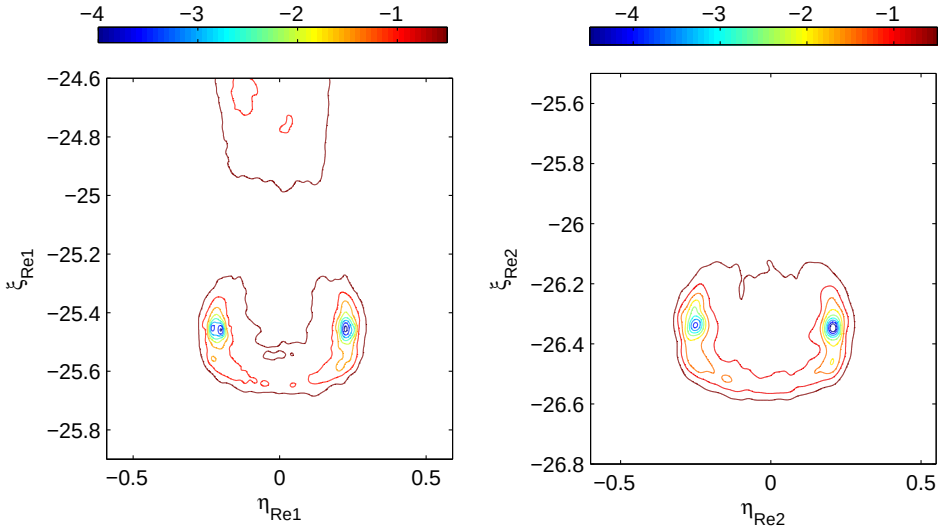

Figure 6.16: Contours of axial normal Reynolds stresses $-\overline{V'V'}$ in similarity coordinates after the column decomposition method has been applied.

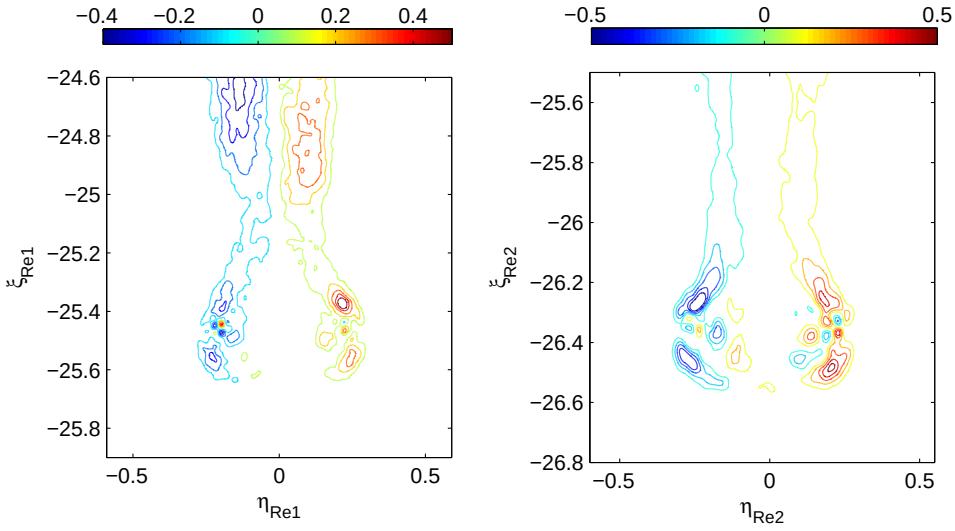

Figure 6.17: Contours of Reynolds shear stresses $-\overline{U'V'}$ in similarity coordinates after the column decomposition method has been applied.

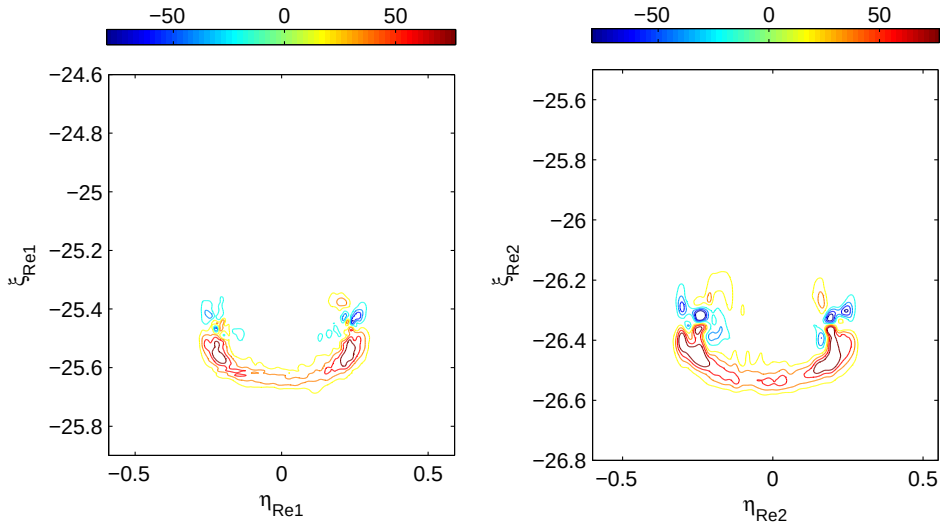

Figure 6.18: Turbulence production contour in similarity coordinates after the second correction method has been applied.

Finally, the turbulence production level in the bubble region is plotted in figure 6.19, for the raw quantities together with the filtered quantities after applying the two filtering algorithms discussed in this chapter. Similar to equation 5.38, the magnitudes of the production level in the bubble region can be written as

$$\int_B |p| \, \mathrm{d}\boldsymbol{B} = \int_B |p| \, \mathrm{d}r\mathrm{d}y. \tag{6.6}$$

There are a few points worth noting once more, even though they are similar to those mentioned for the stress plots. First, the raw levels are quite different even in dimensionless form (scaled by piston velocity and slug circulation). Like the similarity theory, the non-dimensionalising process only accounts for the magnitude but not for the dispersion, therefore a higher level in the Re_2 plot is reasonable (see figure 5.27). Second, after the first correction method (centroid position shift) is applied, the production levels for the two cases both decrease to the level of 0.025, meaning that after the centroid dispersion is excluded, the evidence for Reynolds number independence is already revealed. Third, as with the stress plots in figure 6.13, application of the second correction method (column decomposition) reduces the level by about another 50% and the plots are much smoother. However,

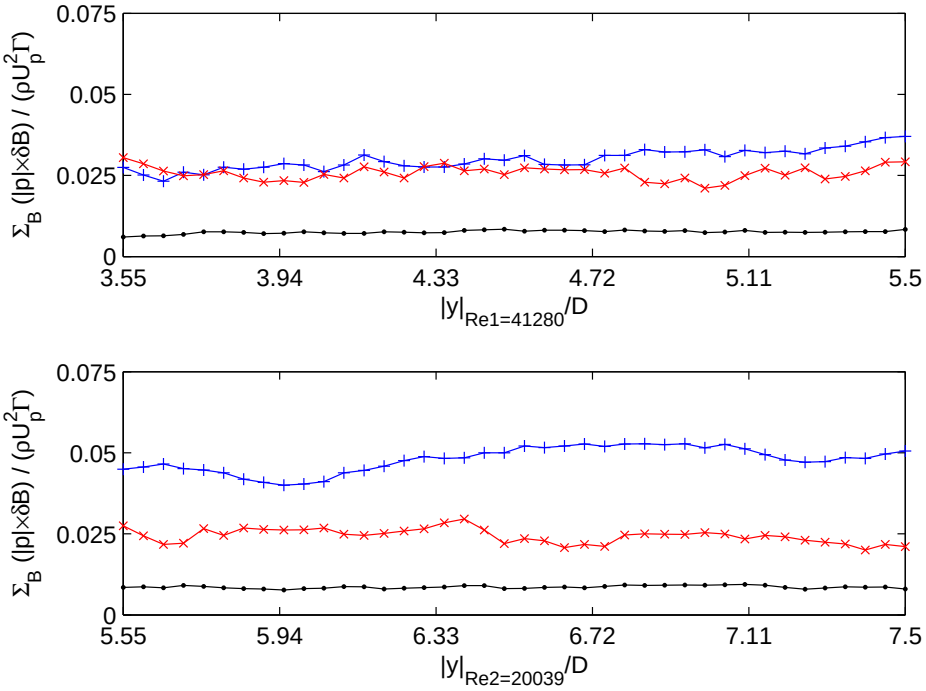

Figure 6.19: The summation of the magnitude of the non-dimensionalised turbulence production over the bubble area $\int_B |p|\,\mathrm{d}\boldsymbol{B}/\rho U_p^2 \Gamma_{slug}$ as a function of ring streamwise location. The production p is calculated from equation 5.39 for i, j up to 2, $+$: the raw quantity p_{totol}; $\times$: after $p_{position}$ is filtered; $\bullet$: after $p_{position}$ and $p_{radius+tilt}$ are filtered.

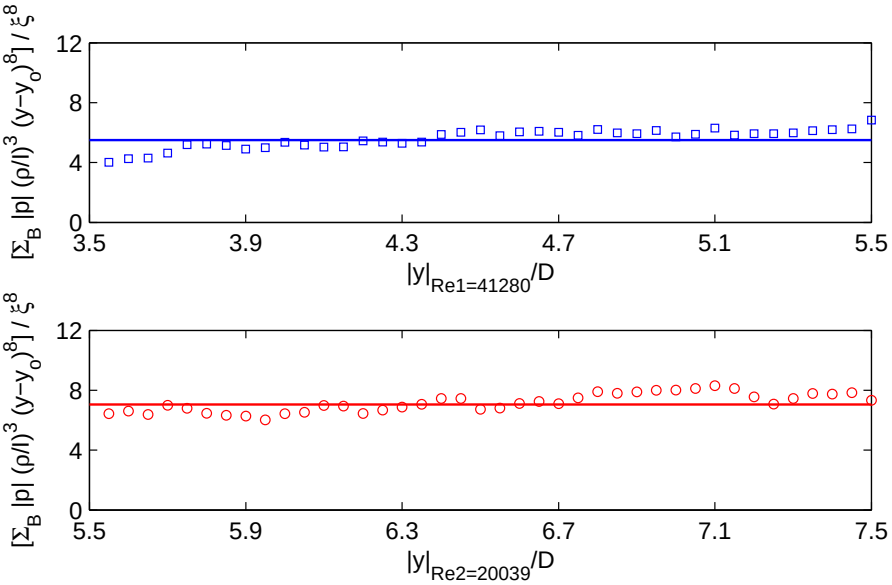

Figure 6.20: The magnitude of the non-dimensionalised turbulence production in the bubble area $\int_B |p|\,\mathrm{d}\boldsymbol{B}$ scaled by the similarity scaling law $\int_B |p|\,\mathrm{d}\boldsymbol{B}\,(\rho/I)^3\,(y-y_o)^8\,/\xi^8$, according to equation 5.43, as a function of ring streamwise location after the column decomposition is applied. The production p is calculated from equation 5.39 for i, j up to 2. □: Re_1 case; ○: Re_2 case. −: the zero-order least-squares fits of □ and ○ with the fixed virtual origins y_o obtained from figure 5.1.

if data in figure 6.19 are presented in similarity coordinates (see figure 6.20), it is noticeable that the similarity theory does not work perfectly as well, probably for the same reasons discussed for the stresses.

Chapter 7

A Three-Dimensional Representation

This chapter presents an effort in an attempt to reconstruct a three-dimensional quantitative visualisation of a single vortex ring by adopting the idea of Taylor's hypothesis, or Taylor's 'frozen turbulence' hypothesis. Section 7.1 gives a brief background of Taylor's hypothesis and an introduction of the procedure of the reconstruction process. The result of the recontruction is shown, and some key features of the vortex ring are successfully captured. Section 7.2 proposes an azimuthal averaging method in cylindrical coordinates, based on the instantaneous three-dimensional velocity information, showing mean velocity and vorticity contours and contours of turbulence quantities.

7.1 The reconstructed velocity field

Taylor's hypothesis (Taylor, 1938; Townsend, 1976) states that "if the velocity of the airstream which carries the eddies is very much greater than the turbulent velocity, one may assume that the sequence of changes in U at the fixed point are simply due to the passage of an unchanging pattern of turbulent motion over the point". In other words, if the relative turbulence intensity u' is assumed to be small enough compared to the mean advection speed U

$$\frac{u'}{U} \ll 1, \tag{7.1}$$

the time-history of the flow signal from a stationary probe can be regarded as that due to advection of a frozen spatial pattern of turbulence past the probe with the mean advection speed U, i.e.

$$u\left(y,t\right)=u\left(y-U\Delta t,t+\Delta t\right) \tag{7.2}$$

where Δt is the time delay and should not be a too large value. Taylor's hypothesis is effectively a method to transfer the time dependent measurement results to a spatial domain.

The accuracy of Taylor's hypothesis is determined by equation 7.1. Theoretically, if $u'\rightarrow 0$, the flow field structure would be like a solid ('frozen') body passing through the testing station. A finite u' means that the different points or layers of data of the subsequently reconstructed flow field along the advection direction belong to different times, so the reconstructed flow field is not strictly a snapshot. If, however, the convection velocity goes to infinity, the time scale for the flow structure to pass the station is effectively zero, and so is the time difference for points on advection path. Because in a real flow problem, U cannot go to infinity, Taylor's hypothesis is only valid if the level of turbulence u' is sufficiently low.

A vortex ring advects downstream due to its self-induced velocity, and the speed of the advection has been given in figure 5.5 and equation 5.7. The dimensionless advection speed U_t for rings of two Reynolds numbers is typically about 6.0 (see figure 5.5 and equation 5.7). When a single vortex ring is to be reconstructed, turbulence intensities will only be due to factor (3) in equation 6.2, i.e. there will be no ensemble-averaging effects. Therefore, the relative dimensionless turbulence intensities $-\overline{U'U'}$ and $-\overline{V'V'}$ are most likely to be the ones in figure 6.15 and 6.16, which are typically below 4. Thus result of equation 7.1 can be estimated as:

$$\frac{u'}{U}=\frac{U'}{U_t}<\frac{2}{6.0}\approx 0.33. \tag{7.3}$$

Although equation 7.1 does not strictly hold, a mean structure can still be successfully reconstructed. For this purpose, the PIV plane needs to be oriented perpendicularly to the ring advection direction, parallel to the x-direction in figure 3.3 and stereoscopic recording is required. In this arrangement, the PIV plane is located at 6D downstream from the orifice exit. Due to physical space restrictions, smaller

streamwise locations are difficult to measure. A backward backward-scattering (BB) camera arrangement is used, i.e. the two cameras are on different sides of the laser sheet (see Lavision, 2007b). In order to orient the laser sheet horizontally, a second optical mirror is placed between the two cameras, at 45^o to the horizontal direction. The laser sheet is reflected twice. Figure C.1 B shows the sketch of this stereoscopic recording setup. After the water-perspex-air refraction is taken into consideration, the effective angle between the two cameras is approximately 120^o, which is quite near to the minimum requirement of the BB setup (Raffel *et al.*, 2007) but the maximum value that can be reached in the physical space. The spatial resolution in this setup is $1.69mm$ and only $Re_1 = 41280$ rings are studied. In this experiment, the Cartesian coordinate system is also adopted with the $+y$ axis points to the $+x$ direction in figure 3.3 but $+x$ axis outward such that the $+z$ axis points upward.[1] These are the default assignment of the stereoscopic PIV arrangement. The x, y, z components are labelled by $\hat{\mathbf{i}}$, $\hat{\mathbf{j}}$, $\hat{\mathbf{k}}$ respectively.

A typical instantaneous PIV velocity - vorticity field looks like that in figure 7.1, in which only the in-plane velocity vectors are plotted and the vorticity is the one calculated from the in-plane velocities which is $\omega\hat{\mathbf{k}}$. The turbulence is indicated by the directions and relative lengths of the vectors and the fluctuations of the vorticity contours. Velocity contours for a typical snapshot of this type can be found in figure 5.36.

In order to visualise the vortex ring structure, after Taylor's reconstruction of velocity field, the vorticity magnitude is shown. In the three-dimensional case, the vorticity vector has three components. In Cartesian coordinates, the vorticity vector is written as

$$\begin{aligned}\vec{\omega} &= \nabla \times \vec{u}\left(\hat{\mathbf{i}}, \hat{\mathbf{j}}, \hat{\mathbf{k}}\right) \\ &= \left(\frac{\partial u_k}{\partial x_j} - \frac{\partial u_j}{\partial x_k}\right)\hat{\mathbf{i}} - \left(\frac{\partial u_k}{\partial x_i} - \frac{\partial u_i}{\partial x_k}\right)\hat{\mathbf{j}} + \left(\frac{\partial u_j}{\partial x_i} - \frac{\partial u_i}{\partial x_j}\right)\hat{\mathbf{k}}. \qquad (7.4)\end{aligned}$$

Therefore,

$$\omega\hat{\mathbf{i}} = \frac{\partial w}{\partial y} - \frac{\partial v}{\partial z}$$

[1] Such coordinate assignment in three-dimensional representations is for convention's sake: the upward direction is indicated by $+z$, instead of by $+y$ as in the previous chapters.

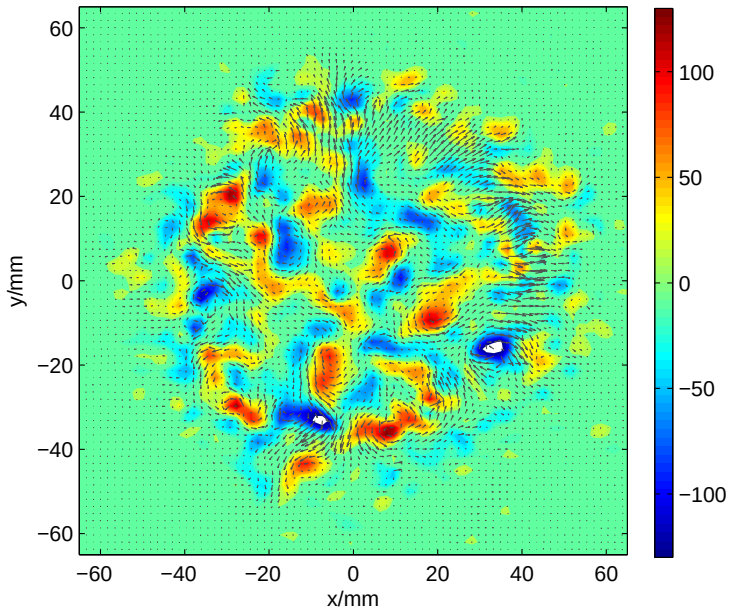

Figure 7.1: An instantaneous presentation of velocity vectors (shown by the arrows) and vorticity (shown by the contours) in the azimuthal plane in physical/dimensional coordinates when the ring centre is about to reach the PIV measurement plane. Only the velocity vectors in the azimuthal $(x - y)$ plane are shown. The vorticity is in the streamwise direction. $Re = 41280$.

$$\begin{aligned} \omega\hat{\mathbf{j}} &= -\left(\frac{\partial w}{\partial x} - \frac{\partial u}{\partial z}\right) \\ \omega\hat{\mathbf{k}} &= \frac{\partial v}{\partial x} - \frac{\partial u}{\partial y}. \end{aligned} \tag{7.5}$$

where $u_i = u$, $u_j = v$ and $u_k = w$; $x_i = x$, $x_j = y$ and $x_k = z$. The magnitude of the vorticity is

$$\omega_m = \sqrt{\omega\hat{\mathbf{i}}^2 + \omega\hat{\mathbf{j}}^2 + \omega\hat{\mathbf{k}}^2} \tag{7.6}$$

where ω_m denotes the magnitude of the vorticity and $\omega\hat{\mathbf{i}}$, $\omega\hat{\mathbf{j}}$, $\omega\hat{\mathbf{k}}$ are defined in equation 7.5.

After the reconstruction process, the structures of the vortex ring-bubble and wake can be clearly observed in figure 7.2, in which the strong level of the turbulence can be indicated by the degree of the surface smoothness of each isosurface level and the streamline patterns. It must be pointed out that in order to visualise the ring bubble by streamlines, the ring needs to be put in a reference frame which moves at the ring's translation speed downstream. This is realised by simply adding the translation velocity of the ring at the PIV testing location[1] on to the instantaneous streamwise velocity at every data point. The computation of vorticities is not affected by adding a constant to the velocity field.

The extent of irregularity of the streamline patterns can be clearly distinguished between upstream and downstream of the ring bubble, and the existence of a strong wake is clearly shown. A wavy core is also obvious, which verifies the existence of the azimuthal waves. In order to see the effect of this waviness on the apparent core dispersion encountered in the two-dimensional PIV results, the compact vortex ring core is reproduced in figure 7.3, with three viewing angles presented. It is easy to see this effect in the second figure. (The PIV plane of the two-dimensional recording is in the y-z plane.)

7.2 The azimuthal-averaged turbulence quantities

If the vortex ring bubble is considered to be axisymmetric, it is possible to compute the turbulence quantities by azimuthal averaging a single realisation, instead of by

[1] It is assumed here that the ring navigation velocity in the vicinity of the PIV testing location is constant, while the decuction of figure 5.5 or a small extrapolation of figure 5.10 shows that it is a function of streamwise distances and hence time.

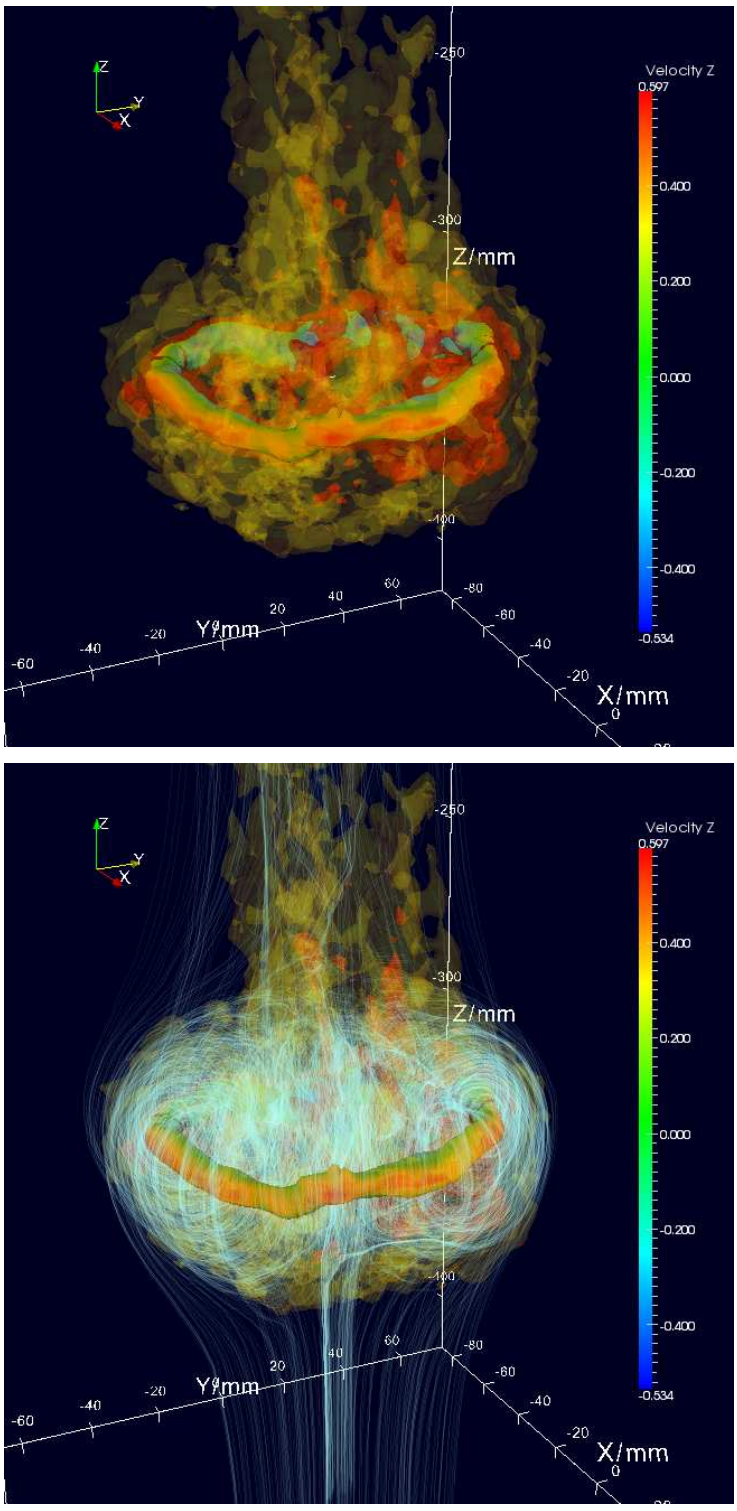

Figure 7.2: A three-dimensional vorticity magnitude Isosurface. Isosurface levels are $150s^{-1}$, $100s^{-1}$, $50s^{-1}$. Streamlines are shown in the second figure. The colour bar shows the streamwise velocity level. $Re = 41280$.

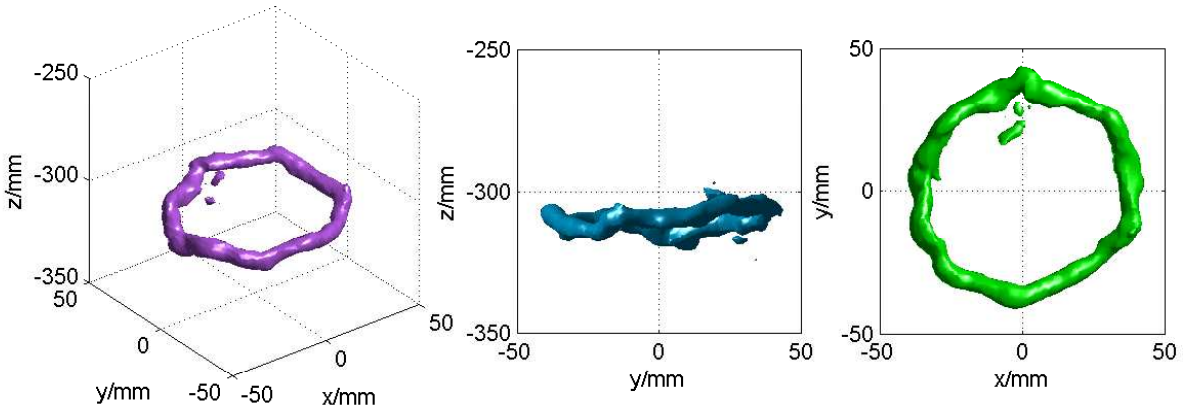

Figure 7.3: A vortex-ring core represented in physical coordinates. The level of the vorticity magnitude is $\omega_m = 150s^{-1}$.

ensemble averaging. The vortex-ring wake is not necessarily axisymmetric, but since the turbulence intensity in the wake is normally low compared to that in the bubble volume (see the contour plots in section 5.2.2 and 5.2.3), the asymmetry of the wake is not believed to be very important.

The azimuthal averaging process is illustrated in figure 7.4, in which a cylindrical coordinate system is used and the averaging process begins at $\theta = 0$ and ends at $\theta = 2\pi$. An initial step is to locate the 'best' centre point, or a proper axis of symmetry. It is because the results from the azimuthal-averaging process depend heavily on the location of this axis. The axis is found by the least-squares fit of the core area to a circle. In figure 7.4, two co-centric circles with radius $35mm$ and $40mm$ are plotted to prove the quality of the fitting.

Because the raw data is stored in Cartesian grids, at smaller radii, there are fewer points to average. In order to improve this shortage, the grid is refined by a factor of ten by two-dimensional cubic spline interpolation to increase the number of data points at small radius. However, there are still different numbers of data points at different radii. In other words, quantities at different radii converge to different extents. Unless one intentionally uses fewer points at larger radii, fully overcoming the problem requires storing the raw data directly into a polar-coordinated mesh, which is not easily achievable.

The method is attempted first with velocity fields, albeit imperfectly. Because

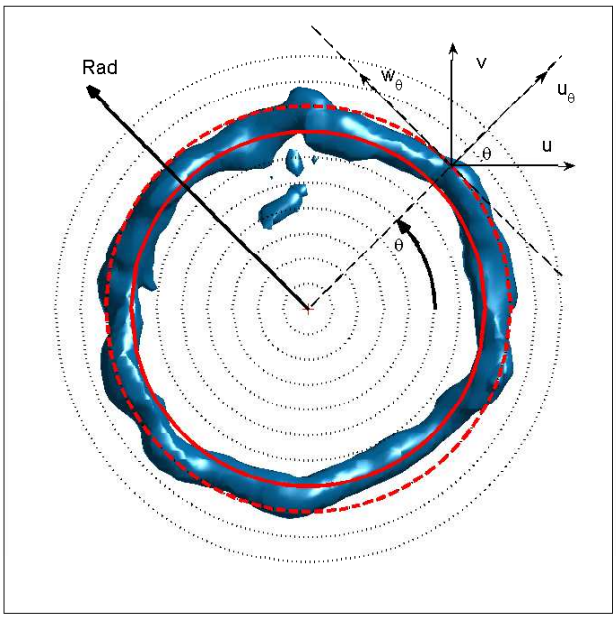

Figure 7.4: A schematic diagram showing the azimuthal averaging process in cylindrical coordinates. Only one azimuthal plane is shown. *Rad* denotes the radial direction and θ denotes the azimuthal direction, positive anti-clockwise; – and –– denote circles of $35mm$ and $40mm$ in radius and centred at the origin.

of the discretized Cartesian grids, the points searching for each radius follows the rule below after the best-fitted centre is located:

$$r \leqslant \sqrt{(x - x_c)^2 + (y - y_c)^2} < r + \frac{\sqrt{2}}{10}\Delta h, \tag{7.7}$$

where r denotes the radial distance from the best-fitted centre (x_c, y_c); $\Delta h = 1.69mm$, which is the spatial resolution, 10 denotes the refinement factor and $\sqrt{2}$ denotes the diagonal of a square grids. Thus it gives an uncertainty of $\sqrt{2}\Delta h/10 = 0.24mm$.

In order to make better comparison with the two-dimensional results, the assignment of the coordinates are changed to the same as for the two-dimensional results and the quantities are non-dimensionalised by equation 4.9 and presented in similarity coordinates calculated from equation 4.7. Figure 7.5 shows the dimensionless velocities U_θ (radial), V_θ (axial), W_θ (azimuthal) and the dimensionless vorticity $\widehat{\omega}_\theta$, where:

$$\widehat{\omega}_\theta = \frac{\partial V_\theta}{\partial \eta} - \frac{\partial U_\theta}{\partial \xi}, \tag{7.8}$$

and the subscript θ, here-and-after denotes an azimuthal-averaged result, ξ, η denote the axial and radial direction in cylindrical coordinates. The velocity components in cylindrical coordinates can be converted from those in Cartesian coordinates. At an arbitrary point in the first quadrant (see figure 7.4), the instantaneous velocities in cylindrical coordinates can be derived by:

$$\begin{aligned} u_\theta &= u\cos\theta + v\sin\theta \\ w_\theta &= -u\sin\theta + v\cos\theta \\ v_\theta &= w, \end{aligned} \tag{7.9}$$

where u, v and w are the velocity components in the three principle directions, in the Cartesian coordinates; u_θ, v_θ and w_θ are the radial, axial and azimuthal velocity components, respectively in cylindrical coordinates. Similar relationships can be derived for points in the other three quadrants.

The first observation of figure 7.5 is that the location of the core is conserved in the similarity coordinates. The second is that there is more noise towards the axis of symmetry in all the contour plots (a)-(d), which is presumably due to the smaller number of data points for averaging in the centre area. There is a weak mean

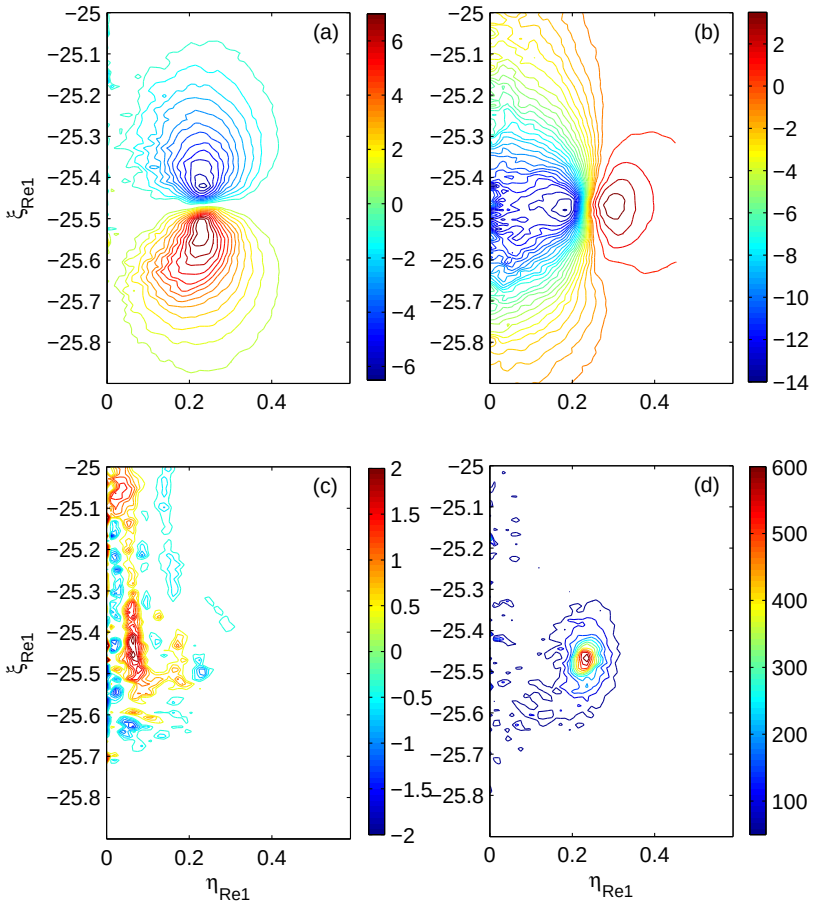

Figure 7.5: The mean structures of velocity and vorticity calculated by azimuthal-averaging: averaging along the θ direction in similarity coordinates. Contours shown are U_θ (radial), V_θ (axial), W_θ (azimuthal) and $\widehat{\omega}_\theta$ (azimuthal) in (a), (b), (c) and (d), respectively.

azimuthal velocity in the azimuthal component W_θ plot (figure 7.5 c): an elongated region of positive mean velocity can be observed in the wake, while a weak negative mean velocity can be observed in the core centre region. The existence of a mean azimuthal velocity in the core region is not surprising, as a number of researchers have also observed such behaviour, which has been reviewed in section 2.3. This could also be attributed to the inaccuracy of the azimuthal-averaging method, which will be discussed later. The opposite-sensed mean velocity in the inner region may be partly due to the noise and partly due to a possible mechanism of conservation of angular momentum of the vortex-ring bubble. The streamline pattern in figure 7.2 is evidence for the mean azimuthal velocity. If it is difficult to see the weak mean motion in the core, some spiral streamlines can be clearly seen in the wake. It must be noted that the mean azimuthal velocities in these two regions are still much weaker than the radial and axial components: U_θ, V_θ.

If the mean velocity structure is correct, the turbulence stresses and production can also be computed by means of azimuthal-average, based on the mean velocities. The three components of Reynolds normal stresses are written as

$$-\overline{U'_\theta U'_\theta}, \quad -\overline{V'_\theta V'_\theta}, \quad -\overline{W'_\theta W'_\theta}, \tag{7.10}$$

where the subscript θ refers to the azimuthal averaging process, in order to differentiate to the quantities from ensemble-averaging process. Similarly the three components of Reynolds shear stresses are written as:

$$-\overline{U'_\theta V'_\theta}, \quad -\overline{U'_\theta W'_\theta}, \quad -\overline{V'_\theta W'_\theta}. \tag{7.11}$$

Similar to equation 5.49, the turbulence production from azimuthal averaging is written as

$$\begin{aligned} P_\theta \;=\; & \left(-\overline{U'_\theta U'_\theta}\frac{\partial U_\theta}{\partial \eta}\right) + \left(-\overline{U'_\theta V'_\theta}\right)\left(\frac{\partial U_\theta}{\partial \xi} + \frac{\partial V_\theta}{\partial \eta}\right) + \left(-\overline{V'_\theta V'_\theta}\frac{\partial V_\theta}{\partial \xi}\right) \\ & + \left(-\overline{W'_\theta W'_\theta}\frac{U_\theta}{\eta}\right). \end{aligned} \tag{7.12}$$

The shape of the contour plots of the normal stresses and the production (figure 7.6 and 7.8) basically agree well with the ensemble-averaged results, except for some disparities in the contour levels. In particular, the wake is only visible in the

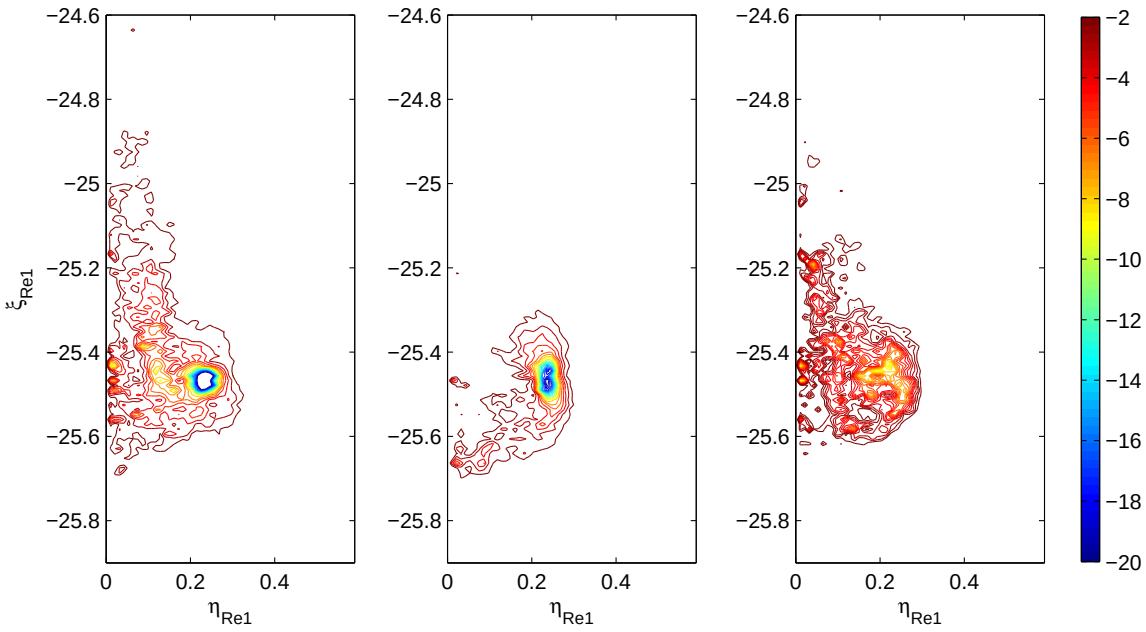

Figure 7.6: Azimuthal-averaged Reynolds normal stresses - averaging along the θ direction in similarity coordinates. Contours shown are $-\overline{U'_\theta U'_\theta}$, $-\overline{V'_\theta V'_\theta}$ and $-\overline{W'_\theta W'_\theta}$, respectively.

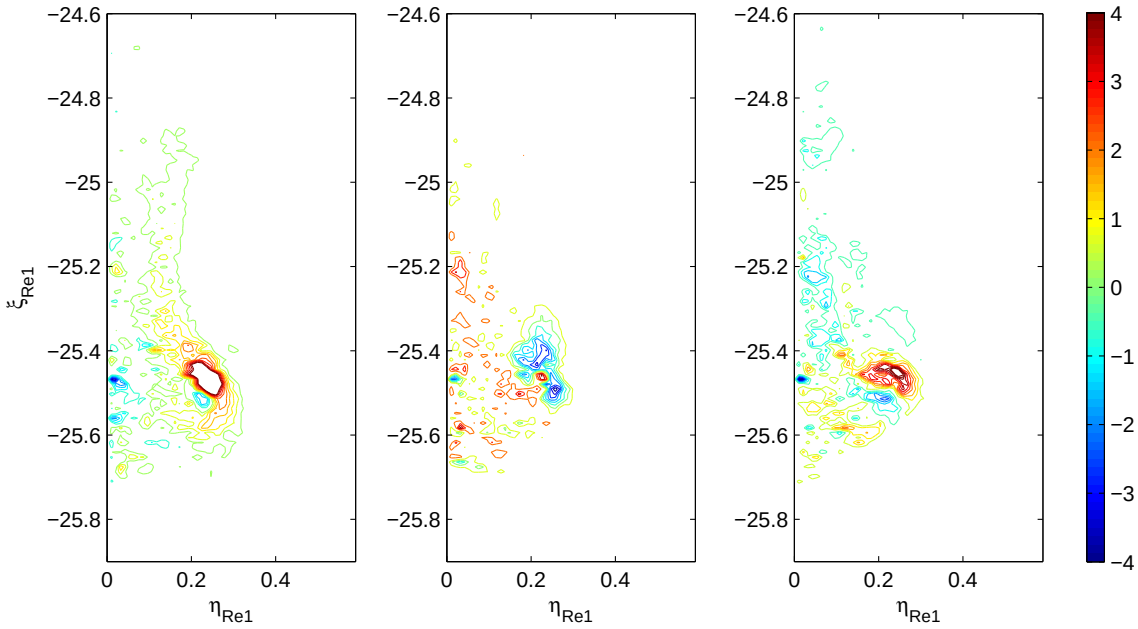

Figure 7.7: Azimuthal-averaged Reynolds shear stresses - averaging along the θ direction in similarity coordinates. Contours shown are $-\overline{U'_\theta V'_\theta}$, $-\overline{U'_\theta W'_\theta}$ and $-\overline{V'_\theta W'_\theta}$, respectively.

radial and azimuthal normal stress components and compared with the in-plane (radial and axial, ξ and η) components, the out-of-plane (azimuthal, θ) components are smaller, for both of the figures. The Reynolds shear stress plot (figure 7.7) has a significant discrepancy compared with figure 5.35; the possible reasons will be considered now.

In general all the contour plots produced by azimuthal average are noisier than those produced by the ensemble average. One of the reasons has been given, which is the extent of convergence. There are at least three more possible reasons for the noisiness and the inaccuracy of this azimuthal averaging method:

1. The first two reasons are associated with the degree of axisymmetry of the vortex ring structure. The terminology of axisymmetry relates to two direct effects in the computation of turbulence quantities by azimuthal averaging. The first effect is the degree of the circularity of the ring projected in the azimuthal plane, or the radius variation. One may argue that the radial vari-

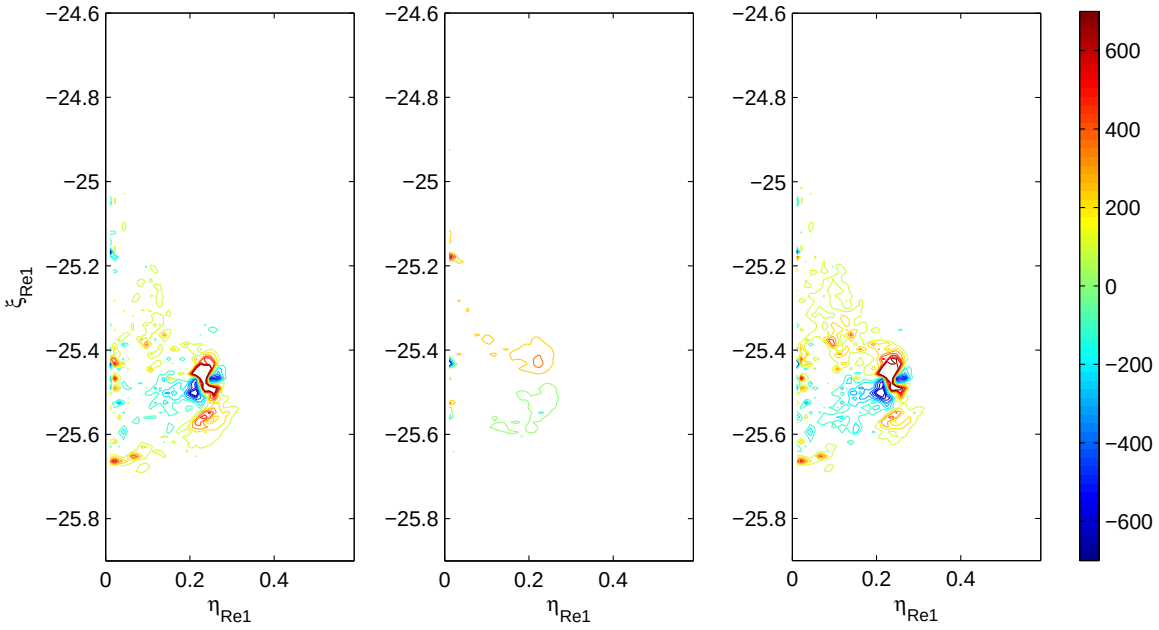

Figure 7.8: Azimuthal-averaged turbulence production - averaging along the θ direction in similarity coordinates. From left to right: sum of the first four terms in equation 7.12, the fifth term in equation 7.12, sum of all the five terms in equation 7.12.

ation is also a factor for the level of turbulence of a vortex ring, nevetheless, it is always ideal to average quantities at the same relative positions in a ring, i.e. to set the averaging path to follow the core shape, so that it reflects the fluctuation more precisely. For argument's sake, if the ring produced is (temporarily) elliptical when projected in the azimuthal plane, the averaging path would ideally also be elliptical, following the core. Figure 7.4 shows the ring core projected in an azimuthal plane and the eccentricity from a perfect circle is clearly seen in the 'southeast' portion.

2. The second effect is the degree of core waviness and the mean tilting angle, or the axial variation. Ideally the azimuthal average in this aspect requires that the core is flat and level in the azimuthal plane. If the tilting angle is large, it is no longer suitable to average along paths in a plane normal to the axial direction in cylindrical coordinates.

3. The core azimuthal waves may be changing (both their amplitudes and phase angles) on a time scale similar to the advection time for the ring structure to pass through the testing station, although this time scale is relatively very small.

4. Although the vortex-ring bubble advects downstream at a finite speed, the wake, which has no mean momentum, does not advect. Therefore Taylor's hypothesis does not 'freeze' the wake, and the contour plots of the wake part are less accurate.

In addition to the noisiness, the averaged core shape is slightly elongated in the axial direction (see figure 7.5 (d)), which may suggest that the effect of reason 2 exceeds the effect of reason 1. The magnitudes of turbulence quantities are especially sensitive to the lack of axisymmetry (point 1 and 2 above) due to the small streamline curvature in the core region which helps answer the questions why the turbulence intensities are higher and the contour shapes are different for the Reynolds shear stresses when they are compared with the ensemble-averaged results.

7.3 Future perspective and implications

Because the waviness along the core is an intrinsic property of a turbulent vortex ring during its development, it is inevitable and should not be corrected artificially when one attempts to compute the turbulence quantities. The azimuthal averaging is a sensible method to account for the effect of the amplitude of the core waviness on the turbulence quantities. The main point for future improvement of the three-dimensional reconstruction discussed in this chapter is to increase its accuracy. There are at least two aspects worth future investigation.

First, in order to freeze the ring structure better, the results of equation 7.3 needs to be closer to zero. Nevertheless, it is expected that for fully turbulent vortex ring, the level of turbulence intensity u' scales with Reynolds number (because $u' \sim U_p$), hence scales with vortex ring circulation Γ and the advection speed u_t. Simply increasing Reynolds number will not improve the situation. Certain treatments independent of the ring will be necessary. A possible way is to move the recording PIV plane (cameras and the laser sheet together) against the ring advection direction - an 'active scanning' process. Equation 7.3 shows that by simply moving the PIV testing plane at the same speed as the ring, it can bring down the ratio u'/u_t significantly to less than 0.167 (doubling the denominator). Moreover, to resolve the wake correctly, an 'active scanning' seems to be compulsory.

Second, the conventional statistical study of non-stationary turbulent flow by an ensemble-averaging process is often useful. As has been pointed out in the beginning of Chapter 6, to accurately correct the effect of dispersion or shape variation, requires fully three-dimensional data. If the active scanning method guarantees a nearly accurate raw three-dimensional velocity field, the correction based on ensemble averaging can be realized and can possibly give a better result. Furthermore, it is also possible to incorporate the ensemble averaging and azimuthal averaging in order to compute the turbulence quantities.

If the ring is in a transient regime, it is not quite turbulent and the bubble volume, and hence the ring core, is still quite compact and isolated, the active scanning or even the 'passive scanning' (stationary PIV testing plane) method will be accurate enough. Therefore, some important properties of the azimuthal instabilities (waves), e.g. the wave number, amplitude, shape, angle and mode, in various conditions

(as discussed in section 2.3) can be revisited with fully three-dimensional velocity information (hence vorticity and other inferred quantities) supported.

It has to be pointed put that, there exists an upper limit of the active scanning speed, it is not allowed, even if it is capable to go to infinity. In other words, it is never possible to capture a true 'frozen' flow field. It is because if the flow is really frozen, there will be no particle displacement, thus the PIV will fail to work. In order to allow a particle displacement, a PIV Δt has to be given at one slice, which is in the order of millisecond. In summary, there will be a trade off for the scanning speed, but an optimal scanning speed is always possible to find.

There is probably a solution for the problem of zero particle displacement at an extremely high scanning speed U_{scan}: a second stereo recording system can be introduced, aligning with the first system in the scanning path, and with a spacing l to the first one. Thus the value of l/U_{scan} effectively gives the PIV Δt. Theoretically, this dual-system arrangement allows the choice of the U_{scan} value to a much higher value: at a fixed U_{scan}, PIV Δt can be adjusted by setting the spacing l between the two systems (two laser sheets) very carefully. By choosing a very high value of U_{scan}, one approaches a truly 'frozen' and instantaneous flow structure.

The state-of-the-art tomographic PIV is also a candidate to give truly instantaneous three-dimensional velocity information of a flow field. However, tomographic PIV would encounter some difficulties when a large volume of the flow is to be examined. To reach the same FOV as the current expariment, a minimum required FOV will be $100mm^3$ (see figure 7.3). This means that first of all, this volume needs to be illuminated; the laser intensity would be very weak when it is diffused to such a large volume. Second, it would be extremely difficult for the cameras to be focused on such a deep FOV (which means the aperture needs to be very small) while accepting enough light during a very short shutter opening time. Therefore, if tomographic PIV is to be used, one can only produce small vortex rings, but small rings will reduce the spatial resolution, probably to an undesirable level.

Chapter 8

Conclusions

Overall, for the streamwise range considered, the similarity theory seems to predict the behaviour of the circulation decay, velocity decay and growth rate very well. In the case of the turbulence quantities the situation is more difficult to assess because the ring dispersion has a much stronger effect on the results. After applying basic and reasonable corrections, however, it does seem that the similarity theory is valid.

The vital differences observed in these two Reynolds number cases, perhaps, is the degree of apparent scattering of core centroids which can be seen in figure 5.1 and figure 5.27. As has been emphasised, the apparent scattering is part of the nature of turbulent rings due to azimuthal waves, and because the waves travel in the azimuthal direction, the PIV plane can cut at local peaks or valleys of the waves not necessarily in a totally random fashion. In other words, there could be a trend that at a certain streamwise location, waves rotate at azimuthal angles such that on one side, cores appear more scattered than on the other. To prove this possibility, the three-dimensional measurements of vortex-ring cores as described in chapter 7 are a potential solution, but a large number of realisations are necessary. (Of course, the imperfection of the ring generator could be another possibility, although it is believed to be a minor factor.) This could also be a reason why in figure 5.27 Re_2 case, the two curves split at about $|y|/D = 5.5$ and soon after $|y|/D = 7$ they merge again. (Notice that 50 realisations should guarantee convergence; see figure 3.4.) The amplitude of the waves directly relates to the degree of instability, which is a function of ring propagation time and distance. The detailed investigation of this scattering trend will be left for future study.

When quantities are plotted to verify the similarity theory, they are scaled with the virtual origins fixed and the zero-order least-squares fits are applied. If the similarity theory works, the experimental data should follow the fitting lines precisely. The fitting of the data are very sensitive to the locations of the origins, which are obtained from figure 5.1. The Re_2 case in figure 5.1 is more scattered, it makes sense to imagine that if the outer part of the individual traces are used to fit,[1] a nearer origin may be obtained which changes the plots slightly and leads to better fits in some figures, like in figure 5.3.

The results presented have shown that all the ensemble-averaged quantities measured in this experiment are not strong functions of Reynolds number when the rings are produced as turbulent and at least up to $Re = 41280$, although the turbulence quantities, after correction, still indicate slightly different similarity quantities. Therefore the elimination of ν in equation 4.1 is a reasonable assumption. The physical explanation of the validity of this elimination, which was mentioned in section 4.2, is the inertial term exceeding the viscous term. This argument is also supported by the instantaneous results of vortex shedding (see section 5.1.8), where the dominant vortex-shedding process is inviscid and a function of the ring core size (see section 5.1.4, where the viscous diffusion effect is not clearly seen to cause the core radius to increase).

Although the hydrodynamic impulse of the entire flow field, after some computational error is excluded (as described in section 5.1), drops, the drop is not significant, at least for the first few orifice diameters (see figure 5.17); furthermore, since the similarity theory works for the ring bubble area, it makes sense to consider the ring bubble impulse instead of the full field impulse, and this quantity is fairly constant. The vortical structure shedding as observed by Maxworthy (1974), by flow visualisation, does not indicate significant impulse loss from the ring bubble. When all the assumptions are valid, similarity theory predicts the development of single-point properties only e.g. Reynolds stresses and turbulence production. When the ensemble-averaging process is applied to obtain these quantities, to properly verify the theory requires that all the realisations are ideal in the sense that they are of the same location, size, tilting angle and shape. This is not possible because of the

[1] By using the outer part, it is suggested that the inner parts do not reveal the true ring radius, they are rather influenced either by the azimuthal waves or by the dispersion.

effect of core dispersion, which is inherent in the nature of turbulent vortex rings and it is the core dispersion that has a significant effect on the results. The contribution from the intensity fluctuation to the turbulence quantities is shown to be below 10% of the raw, or the total level, and because the shapes of the turbulent vortex rings differ, perfect similarity decay is not seen. Despite the imperfection in the similarity decay, they are least-squares fitted to give the similarity constants presented in table 8.1. Some parts of this research activity have been contributed to Gan & Nickels (2010).

A three-dimensional reconstruction method following the idea of Taylor's hypothesis is also attempted in order to give an approximate three-dimensional velocity field. The method has some success in capturing the ring-core waviness, albeit suffering from the intrinsic limitations of Taylor's hypothesis. It shows that the azimuthal waviness does not only exist in a ring's transitional regime from laminar to turbulent, it can appear in a fully turbulent ring. With the aid of the fully three-dimensional information, the vortex stretching effect is also presented, which is verified to be closely related to the source of the turbulence production. An azimuthal-averaging process is also proposed in an attempt to give a two-dimensional averaged contour based on a single realisation. This averaging process shows some agreement with the traditional ensemble-averaged results, but it is not believed to be a perfect method, because of the limitations mentioned. A possible cure is the active scanning method applied on ensemble realisations, as discussed in section 7.3.

Figure number	Quantities on the ordinate	The similarity constants	Re_1	Re_2	LDV
5.5	$\left[4u_t\left(\rho/I\right)\left(y-y_o\right)^3\right]^{1/4}$	$\lvert\xi\rvert$	25.463	26.380	25.0
5.5		$\lvert U_t\rvert$	6.36	6.60	6.25
5.1		η	0.225	0.232	
5.3*	$\lvert v_{peak}\rvert\left(\rho/I\right)\left(y-y_o\right)^3/\xi^3$	$\lvert V_{peak}\rvert$	15.464	15.177	
5.15*	$\left[\int_{B'}\omega\,\mathrm{d}x\mathrm{d}y\right]\left(\rho/I\right)\left(y-y_o\right)^2/\xi^2$	$\int_{S'}\widehat{\omega}\,\mathrm{d}\xi\mathrm{d}\eta$	6.869	7.096	7.71
5.12	$\left[\int_{y_a}^{y_b}\pi x^2\,\mathrm{d}y\right]\xi^3/\left(y-y_o\right)^3$	$\int_{\xi_a}^{\xi_b}\pi\eta^2\,\mathrm{d}\xi$	0.076	0.078	0.048
6.14*	$\int_B\lvert-\overline{u'u'}\rvert\mathrm{d}\boldsymbol{B}\left(\rho/I\right)^2\left(y-y_o\right)^4/\xi^4$	$\int_S\lvert\overline{U'U'}\rvert\mathrm{d}\xi\mathrm{d}\eta$	0.199	0.242	
6.14*	$\int_B\lvert-\overline{v'v'}\rvert\mathrm{d}\boldsymbol{B}\left(\rho/I\right)^2\left(y-y_o\right)^4/\xi^4$	$\int_S\lvert\overline{V'V'}\rvert\mathrm{d}\xi\mathrm{d}\eta$	0.176	0.215	
6.14*	$\int_B\lvert-\overline{u'v'}\rvert\mathrm{d}\boldsymbol{B}\left(\rho/I\right)^2\left(y-y_o\right)^4/\xi^4$	$\int_S\lvert\overline{U'V'}\rvert\mathrm{d}\xi\mathrm{d}\eta$	0.014	0.011	
6.20*	$\int_B\lvert p\rvert\,\mathrm{d}\boldsymbol{B}\left(\rho/I\right)^3\left(y-y_o\right)^8/\xi^8$	$\int_S\lvert P\rvert\mathrm{d}\xi\mathrm{d}\eta$	5.50	7.05	

Table 8.1: Similarity constants obtained from the data. LDV represents the results from Glezer & Coles (1990). $Re_1 = 41280$, $Re_2 = 20039$. U_t is the similarity quantity corresponding to the ring translation velocity (equation 5.7). $*$: quantities that do not obey the similarity theory perfectly, but least-squares fitting is still applied to find the approximate similarity quantities. $\widehat{\omega}$: The dimensionless vorticity (equation 5.31); B: the bubble region in dimensional/physical coordinates; B': half of the bubble region for circulation calculation in dimensional/physical coordinates; S: the bubble region in similarity coordinates; S': half of the bubble region for circulation calculation in similarity coordinates. P: the dimensionless turbulence production, calculated from the first four terms in equation 5.45. Note that the LDV circulation is computed for the full flow field, however figure 5.15 shows that the full-field circulation deviates from the similarity theory significantly. The circulation shown here is the bubble circulation.

Appendix A

Maxworthy's model for turbulent vortex rings

There are two assumptions made for deriving the mathematical description of the long-term behaviour of turbulent vortex ring: the turbulent core and its co-travelling bubble are assumed to be geometrically similar at all times and the Reynolds number is large enough for viscosity to be unimportant in determining the gross properties of the flow. The growth rate of the ring bubble volume is proportional to the ring instantaneous surface area and propagation velocity:

$$\frac{\mathrm{d}}{\mathrm{d}\,t}\left(\frac{4}{3}\pi R^3 k_1\right) = 4\pi R^2 U \alpha' k_2,$$

therefore,

$$\frac{\mathrm{d}\,R^3}{\mathrm{d}\,t} = 3\alpha R^2 U, \tag{A.1}$$

where $\alpha = \alpha' k_2/k_1$, which is an entrainment coefficient and k_1, k_2 are coefficients which relate the actual volume and surface area of the ring to those of an equivalent sphere of radius R. Similarly, the equation of impulse loss rate can be modelled by an equivalent drag force:

$$\frac{\mathrm{d}\,I}{\mathrm{d}\,t} = \frac{\mathrm{d}}{\mathrm{d}\,t}\left(2\pi\rho R^3 U k_3\right) = -\frac{1}{2}C_D''\rho U^2 \pi R^2 k_4,$$

which reduces to

$$\frac{\mathrm{d}}{\mathrm{d}\,t}\left(R^3 U\right) = -\frac{1}{4}C_D' U^2 R^2, \tag{A.2}$$

where $C_D' = C_D'' k_4/k_3$, which is a drag coefficient, and k_3, k_4 are again geometrical coefficients to account for the shape factor. The ring propagating velocity can be written as

$$U = \frac{\mathrm{d}\,x}{\mathrm{d}\,t}, \tag{A.3}$$

where x is the streamwise distance.

The above three equations serve as the governing equations to seek the scaling law of U and R (with respect to t).

Equation A.1 can be reduced to

$$\frac{\mathrm{d}\,R}{\mathrm{d}\,t} = \alpha U. \tag{A.4}$$

By refering to equation A.3,

$$\frac{\mathrm{d}\,R}{\mathrm{d}\,x} = \alpha. \tag{A.5}$$

Therefore,

$$\frac{\mathrm{d}\,R^3}{\mathrm{d}\,x} = 3\alpha R^2.$$

Equation A.2 and A.3 give

$$\frac{\mathrm{d}}{\mathrm{d}\,x}\left(R^3 U\right) = -\frac{1}{4} C_D' U R^2, \tag{A.6}$$

which can be expanded and rearranged to give

$$\int_{U_o}^{U} \frac{\mathrm{d}\,U}{U} = -\int_{R_o}^{R} \left(\frac{C_D'}{4\alpha} + 3\right) \frac{\mathrm{d}\,R}{R}. \tag{A.7}$$

Integration and simplification gives

$$\overline{U} = \overline{R}^{\left[-\left(C_D'/4\alpha\right)-3\right]} = \overline{R}^{[-C_D-3]}, \tag{A.8}$$

where $\overline{U} = U/U_o$, $\overline{R} = R/R_o$ and $C_D = C_D'/4\alpha$. If two more dimensionless numbers are defined as $\overline{t} = t/t_c$ and $t_c = R_o/\alpha U_o$, combining equation A.4 and A.8, it can be shown that

$$\overline{R} = \left[(C_D+4)\,\overline{t}+1\right]^{\frac{1}{C_D+4}} \tag{A.9}$$

$$\overline{U} = \left[(C_D+4)\,\overline{t}+1\right]^{-\frac{C_D+3}{C_D+4}}, \tag{A.10}$$

because $\overline{R} = 1$ when $\overline{t} = 0$.

Thus the scaling law becomes

$$\begin{aligned} R &\sim t^{1/(C_D+4)} \\ U &\sim t^{-(C_D+3)/(C_D+4)} \\ U &\sim R^{-(C_D+3)} \sim x^{-(C_D+3)}. \end{aligned} \tag{A.11}$$

Note that when $C_D \to 0$, scaling law in equation A.11 reduces to the results of the similarity theory. The value of C_D in Maxworthy (1974) is found to be between 1.8 and 2.7 by curve fitting of his experimental data.

Appendix B

Johnson's model for turbulent vortex rings

Johnson (1970) found that for distances of 70 diameters from the nozzle, the behaviour of turbulent vortex rings can be accurately described by the following empirical equations

$$\frac{(t-t_o)}{T_o} = C\left(\frac{x-x_o}{D}\right)^{\frac{2}{3}}, \tag{B.1}$$

and

$$2\frac{R}{D} = K\left(\frac{x-x_o}{D}\right)^{\frac{1}{6}}, \tag{B.2}$$

where K and C are constants and t_o and x_o are virtual origins in time and space respectively. T_o is the time scale for vortex ring generation, R is the radius of the ring and D is the diameter of the vortex generator.

Equation B.1 can be arranged to:

$$\left(\frac{x-x_o}{D}\right) = C'\left(\frac{t-t_o}{T_o}\right)^{\frac{3}{2}},$$

where C' is another constant. Differentiating the above equation with respect to time, the dimensionless ring propagation velocity U/U_o can be calculated as

$$\frac{U}{U_o} = C''\left(\frac{t-t_o}{D}\right)^{\frac{1}{2}}, \tag{B.3}$$

where U_o is a velocity scale from the apparatus. Thus,

$$U \sim (t-t_o)^{\frac{1}{2}}$$

$$\sim \quad (x - x_o)^{\frac{1}{3}} . \tag{B.4}$$

From equation B.1,

$$\begin{aligned} R &\sim (t - t_o)^{\frac{1}{4}} \\ &\sim (x - x_o)^{\frac{1}{6}} . \end{aligned} \tag{B.5}$$

This model shows that the ring propagation velocity U increases with downstream distance, which is not very reasonable, because the energy of the ring always decays.

The large discrepancies between Johnson's scaling law and the other two scaling laws could be partly because of the difficulty of quantifying the effect of initial conditions in different experiments, and partly because of the different ranges of the data used to empirical fitting. Seventy diameters downstream could be too much for the ring to maintain a high level of turbulence, thus the viscous effect may be important.

Appendix C

Schematic views of stereoscopic recordings

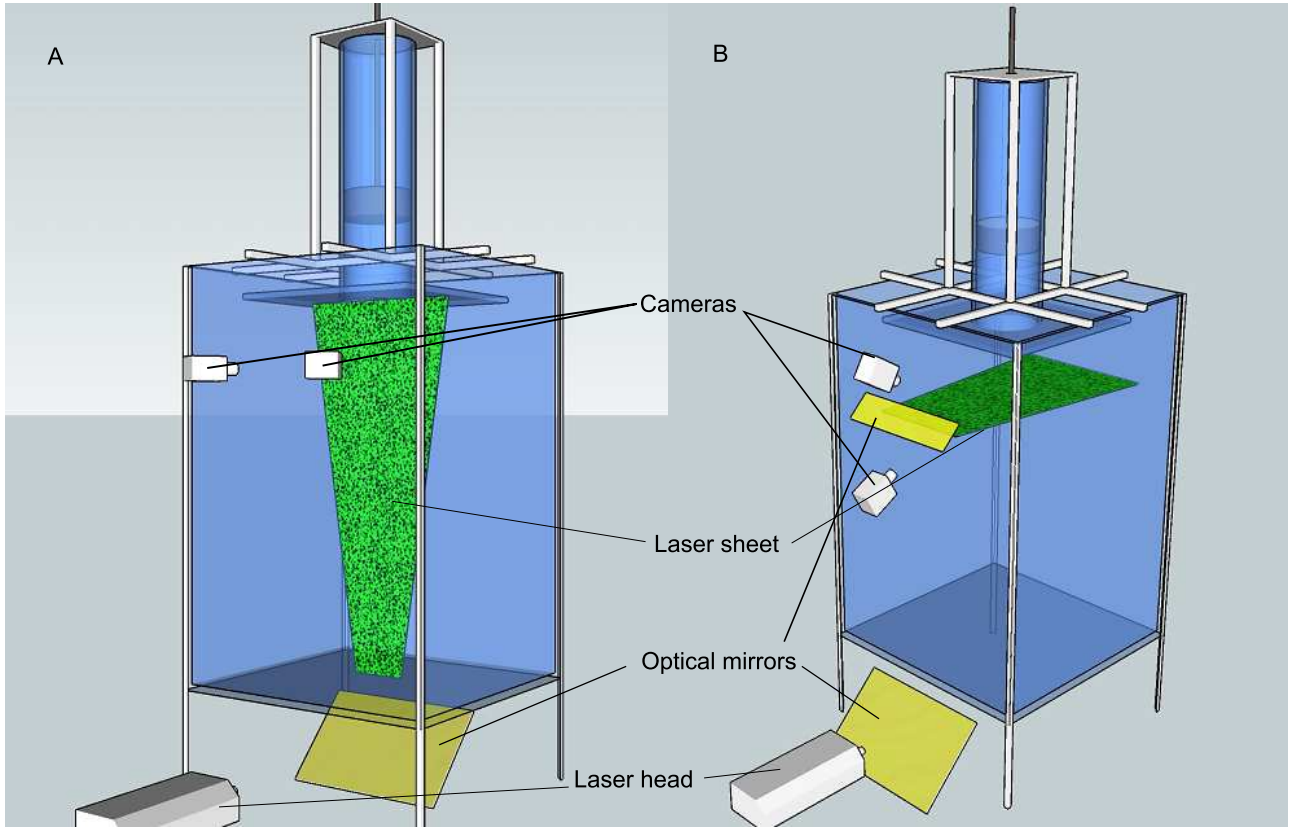

Figure C.1: Schematic diagrams of the stereoscopic recording set-ups. A: the first type, for centre-cross section; B: the second type, for three-dimensional reconstruction method. Note that the laser sheet is invisible without the seeding reflection. The sketch is not to scale.

Appendix D

Results from Laser Doppler Velocimeter measurements

The contour plots of various turbulence quantities from LDV measurements are shown here. These results are taken from Glezer & Coles (1990). Note that in all these plots, LDV results use different definitions of the quantities, in which the minus signs are all not included. For instance, the streamwise Reynolds stress is written as $\overline{V'V'}$ instead of $-\overline{V'V'}$. Similarly the production term (equation 5.49) is also calculated without the minus signs included in the stress terms, i.e. $P_{LDV} = -P_{PIV}$, where P_{PIV} refers to the production in equation 5.49.

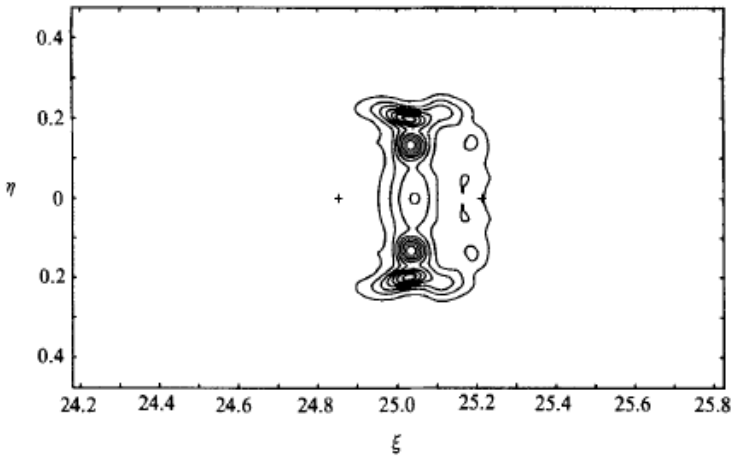

Figure D.1: LDV streamwise Reynolds stress $\overline{V'V'}$ in similarity coordinates. Contour levels: 0.25(0.25)2.00.

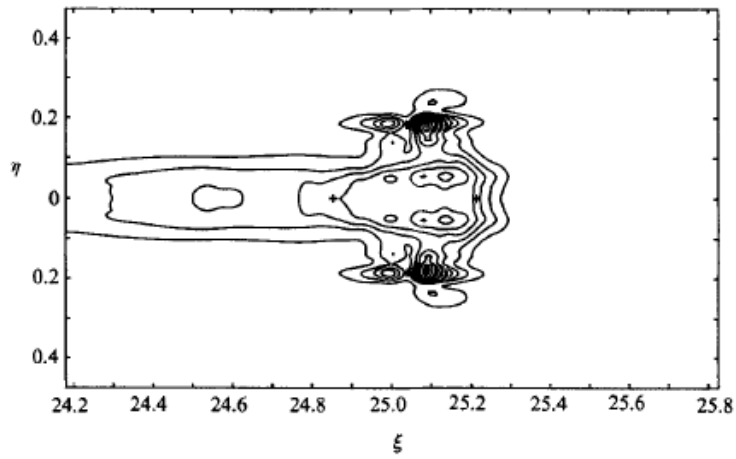

Figure D.2: LDV radial Reynolds stress $\overline{U'U'}$ in similarity coordinates. Contour levels: 0.5(0.5)4.5.

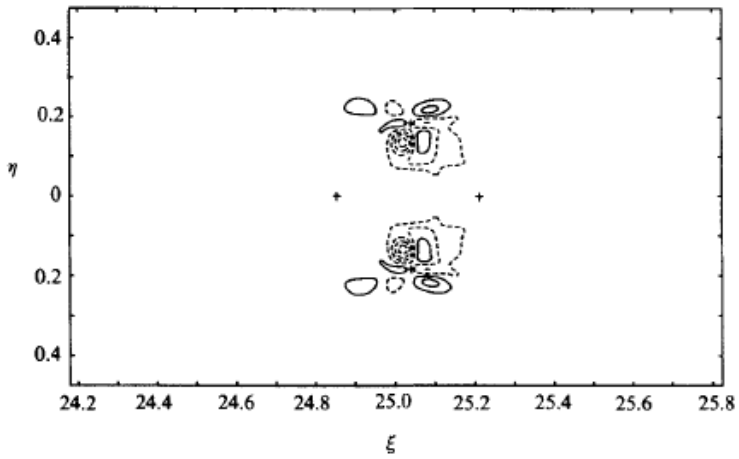

Figure D.3: LDV Reynolds shear stress $\overline{U'V'}$ in similarity coordinates. Contour levels: -0.7(0.2)0.3.

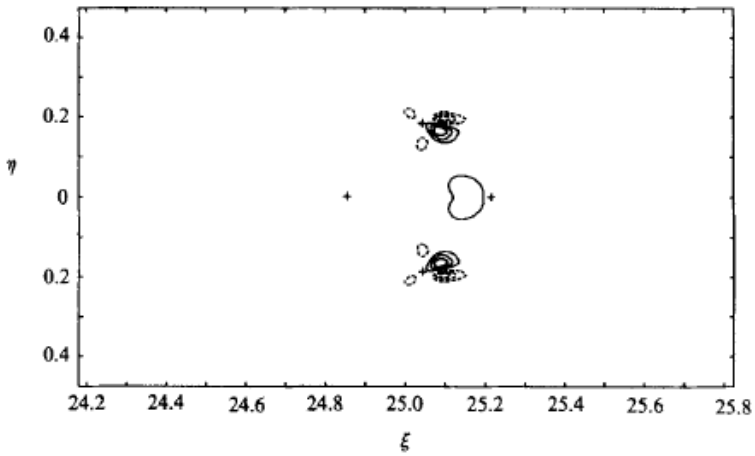

Figure D.4: LDV turbulence production, the sum of the first four terms in equation 5.49 in similarity coordinates. Contour levels: -300(100)300. Zero level bypassed.

References

Adrian, R.J. (1991). Particle-imaging techniques for experimental fluid mechanics. *Annu. Rev. Fluid Mech.*, **23**, 261–304. 24

Allen, J.J. & Chong, M.S. (2000). Votex formation in front of a piston moving through a cylinder. *J. Fluid Mech.*, **416**, 1–28. 8

Archer, P.J., Thomas, T.G. & Coleman, G.N. (2008). Direct numerical simulation of vortex ring evolution from the laminar to the early turbulent regime. *J. Fluid Mech.*, **598**, 201–226. 15, 16

Bergdorf, M., Koumoutsakos, P. & Leonard, A. (2007). Direct numerical simulations of vortex rings at Re_Γ =7500. *J. Fluid Mech.*, **581**, 495–505. 14, 15, 64

Cater, J.E., Soria, J. & Lim, T.T. (2004). The interaction of the piston vortex with a piston-generated vortex ring. *J. Fluid Mech.*, **499**, 327–343. 8, 20

Dabiri, J.O. (2005). On the estimation of swimming and flying forces from wake measurements. *J. Exp. Biol.*, **208**, 3519–3532. 18

Dabiri, J.O. (2009). Optimal vortex formation as a unifying principle in biological propulsion. *Annu. Rev. Fluid Mech.*, **41**, 17–33. 18

Dabiri, J.O. & Gharib, M. (2004a). Delay of vortex ring pinch-off by an imposed bulk counter-flow. *Phys. Fluids*, **16(4)**, L28–L30. 18

Dabiri, J.O. & Gharib, M. (2004b). Fluid entrainment by isolated vortex rings. *J. Fluid Mech.*, **511**, 311–331. 57, 58

Dabiri, J.O. & Gharib, M. (2005). Starting flow through nozzles with temporally variable exit diameter. *J. Fluid Mech.*, **538**, 111–136. 16

Dabiri, J.O., Colin, S.P. & Costello, J.H. (2007). Morphological diversity of medusan lineages constrained by animalfluid interactions. *J. Exp. Biol.*, **210**, 1868–1873. 3

Davidson, P.A. (2004). *Turbulence, An introduction for scientists and Engineers.*. Oxford University Press, Oxford. 71

Dazin, A., Dupont, P. & Stanislas, M. (2006a). Experimental characterization of the instability of the vortex ring. Part i: Linear phase. *Exp. Fluids*, **40**, 383–399. 14, 15

Dazin, A., Dupont, P. & Stanislas, M. (2006b). Experimental characterization of the instability of the vortex ring. Part ii: Non-linear phase. *Exp. Fluids*, **41**, 401–413. 14, 15

Didden, N. (1979). On the formation of vortex rings: rolling-up and production of circulation. *Z. Angew. Math. Phys.*, **30**, 101–116. 7, 8, 9, 66

Einstein, A., Lorentz, H., Minkowski, H. & Weyl, H. (1952). *The Principle of Relativity: a collection of original memoirs on the special and general theory of relativity.*. Courier Dover, N. Chelmsford. 93

Friedlander, S.K. & Topper, L. (1962). *Turbulence: Classical papers on statistical theory.*. Interscience, New York. 28

Gan, L. & Nickels, T.B. (2007). Use of 'Baker's method' to visualize vortex rings. *Proceeding in the* 9^{th} *Asian Symposium on Visualization, HK*. 16

Gan, L. & Nickels, T.B. (2008). An experimental study of turbulent vortex rings. *Proceedings of the iTi Conference in Turbulence*, **131**, 263–266. 30

Gan, L. & Nickels, T.B. (2010). An experimental study of turbulent vortex rings during their early development. *J. Fluid Mech.*, **649**, 467–496. 142

Gharib, M., Rambod, E. & Sharrif, K. (1998). A universal time scale for vortex ring formation. *J. Fluid Mech.*, **360**, 121–140. 16, 17, 39

Gharib, M., Rambod, E., Kheradvar, A., Sahn, D.J. & Dabiri, J.O. (2006). Optimal vortex formation as an index of cardiac health. *Proc. Natl. Acad. Sci. USA*, **103**, 6305–6308. 4

Glezer, A. (1988). On the formation of vortex rings. *Phys. Fluids*, **31**, 3532–3542. 10, 11

Glezer, A. & Coles, D. (1990). An experimental study of a turbulent vortex ring. *J. Fluid Mech.*, **211**, 243–283. 11, 12, 13, 25, 28, 32, 33, 40, 42, 72, 109, 111, 115, 143, 151

Hughes, M.D. & Gerrard, J.H. (1971). The stability of unsteady axisymmetric incompressible pipe flow close to a piston. Part 2. Experimental investigation and comparison with computation. *J. Fluid Mech.*, **50**, 645–655. 8

Jeon, D. & Gharib, M. (2004). On the relationship between the vortex formation process and cylinder wake vortex patterns. *J. Fluid Mech.*, **519**, 161–181. 18

Johnson, G.M. (1970). Researches on the propagation and decay of vortex rings. *ARL Report 70-0093 Aerospace Res. Labs., Wright-Patterson Air Force Base*. 11, 13, 40, 147

Johnson, G.M. (1971). An empirical model of turbulent vortex rings. *AIAA J.*, **9**, 763–764. 11

Krueger, P.S. & Gharib, M. (2003). The significance of vortex formation to the impulse and thrust of a starting jet. *Phys. Fluids*, **15**, 1271–1281. 66

Krueger, P.S., Dabiri, J.O. & Gharib, M. (2003). The formation number of vortex rings formed in the presence of uniform background co-flow. *Phys. Fluids*, **15(7)**, L49–L52. 18

Krutzsch, C.H. (1939). Über eien experimentell beobachtete erscheinung an wirbelringen bei ihrer translatiorischen bewegung in wirkichen flüssigkeiten. *Annalen der Physik*, **35**, 497–523. 14

Lavision (2007a). *Product Manual-DaVis 7.2 Software.*. Lavision GmbH, Gottingen. 24

Lavision (2007b). *Product Manual-FlowMaster for DaVis7.2.*. Lavision GmbH, Gottingen. 22, 24, 27, 29, 125

Lavision (2007c). *Product Manual-Hardware.*. Lavision GmbH, Gottingen. 24

Lavision (2007d). *Product Manual-HighSpeedStar5.*. Lavision GmbH, Gottingen. 24

Lavision (2007e). *Product Manual-Pegasus Laser.*. Lavision GmbH, Gottingen. 24

Lim, T.T. & Nickels, T.B. (1995). *Vortex rings. In* Fluid vortices*(ed. S. I. Green).*. Springer-Verlag, Kluwer. 5, 13, 47, 66

Maxworthy, T. (1972). The structure and stability of vortex rings. *J. Fluid Mech.*, **51**, 15–32. 10, 14

Maxworthy, T. (1974). Turbulent vortex rings. *J. Fluid Mech.*, **64**, 227–239. 11, 13, 33, 46, 65, 141, 146

Maxworthy, T. (1977). Some experimental studies of vortex rings. *J. Fluid Mech.*, **81**, 465–495. 8, 9, 14, 15

Milano, M. & Gharib, M. (2005). Uncovering the physics of flat plates with artificial evolution. *J. Fluid Mech.*, **534**, 403–409. 18

Mohseni, K. (2001). Statistical equilibrium theory for axisymmetric flows: Kelvins variational principle and an explanation for the vortex ring pinch-off process. *Phys. Fluids*, **13**, 1924–1931. 16

Mohseni, K. & Gharib, M. (1998). A model for universal time scale of vortex ring formation. *Phys. Fluids*, **10**, 24362438. 16

Mohseni, K., Ran, H.Y. & Colonius, T. (2001). Numerical experiments on vortex ring formation. *J. Fluid Mech.*, **430**, 267–282. 16

Moin, P. (2001). *Fundamentals of Engineering Numerical Analysis.*. Cambridge University Press, Cambridge. 39, 56

Moore, D.W. & Saffman, P.G. (1975a). The instability of a straight vortex filament in a strain field. *Proc. R. Soc. London, Ser. A*, **356**, 413. 15

Moore, D.W. & Saffman, P.G. (1975b). The motion of a vortex filament with axial flow. *Philos. Trans. R. Soc. London, Ser. A*, **356**, 413. 15

Naitoh, T., Fukuda, N., Gotoh, T., Yamada, H. & Nakajima, K. (2002). Experimental study of axial flow in a vortex ring. *Phys. Fluids*, **14**, 143–149. 15

Nitsche, M. & Krasny, R. (1994). A numerical study of vortex ring formation at the edge of a circular tube. *J. Fluid Mech.*, **276**, 139–161. 8

Peck, B. & Sigurdson, L.W. (1994). The three-dimensional vortex structure of an impacting water drop. *Phys. Fluids*, **6(2)**, 564–576. 2

Prasad, A.K. (2000). Stereoscopic particle image velocimetry. *Exp. Fluids*, **29**, 103–116. 24

Pullin, D.I. (1979). Vortex ring formation at tube and orifice openings. *Phys. Fluids*, **22(3)**, 401–403. 10

Raffel, M., Willert, C., Wereley, S. & Kompenhans, J. (2007). *Particle Image Velocimetry-A Practical Guide, Second Edition.*. Springer-Verlag, Berlin. 22, 24, 29, 125

Ringuette, M.J., Milano, M. & Gharib, M. (2007). Role of the tip vortex in the force generation of low-aspect-ratio normal flat plates. *J. Fluid Mech.*, **581**, 453–468. 18

Rosenfeld, M., Rambod, E. & Gharib, M. (1998). Circulation and formation number of laminar vortex rings. *J. Fluid Mech.*, **376**, 297–318. 16

Saffman, P.G. (1970). The velocity of viscous vortex rings. *Stud. Appl. Maths*, **49**, 371–380. 47

Saffman, P.G. (1976). *Vortex Dynamics.*. Cambridge University Press, Cambridge. 33, 66

Saffman, P.G. (1978). The number of waves on unstable vortex rings. *J. Fluid Mech.*, **84**, 625–639. 10, 14, 15, 47

Sallet, D.W. & Widmayer, R.S. (1974). Sekundärwirbelbildung bei ringwirbeln und in freistrahlen. *Z. Flugwiss. Weltraumforsch*, **4**, 307–318. 11, 40

Shariff, K. & Leonard, A. (1992). Vortex rings. *Annu. Rev. Fluid Mech.*, **24**, 235–279. 5, 9, 13, 47, 66

Shariff, K., Verzicco, R. & Orlandi, P. (1994). A numerical study of three-dimensional vortex ring instabilities: viscous corrections and early nonlinear stage. *J. Fluid Mech.*, **279**, 351–375. 14, 15

Taylor, G.I. (1938). The spectrum of turbulence. *Proc. R. Soc. London, Ser. A*, **164**, 476–490. 12, 71, 123

Tennekes, H. & Lumley, J.L. (1972). *A first course in turbulence.*. The MIT Press, Cambridge, Massachusetts. 28, 71

Townsend, A.A. (1976). *The structure of turbulent shear flow. Second Edition.*. Cambridge University Press, Cambridge. 123

van Dyke, M. (1982). *An album of fluid motion.*. The Parabolic Press, Stanford. 2, 14

Weigand, A. & Gharib, M. (1994). On the decay of a turbulent vortex ring. *Phys Fluids*, **6(12)**, 3806–3808. 14, 64

Widnall, S.E. & Sullivan, J.P. (1973). On the stability of vortex rings. *Proc. R. Soc. London, Ser. A*, **332**, 335–353. 14

Widnall, S.E. & Tsai, C.Y. (1977). The instability of the thin vortex ring of constant vorticity. *Philo Trans R Soc Lond A*, **287**, 273–305. 14, 15

Widnall, S.E., Bliss, D.B. & Tsai, C.Y. (1974). The stability of short waves on a vortex ring. *J. Fluid Mech.*, **66**, 35–47. 14, 15